Developing and Analysing sub-10 µm Fluidic Systems with Integrated Electrodes for Pumping and Sensing in Nanotechnology Applications

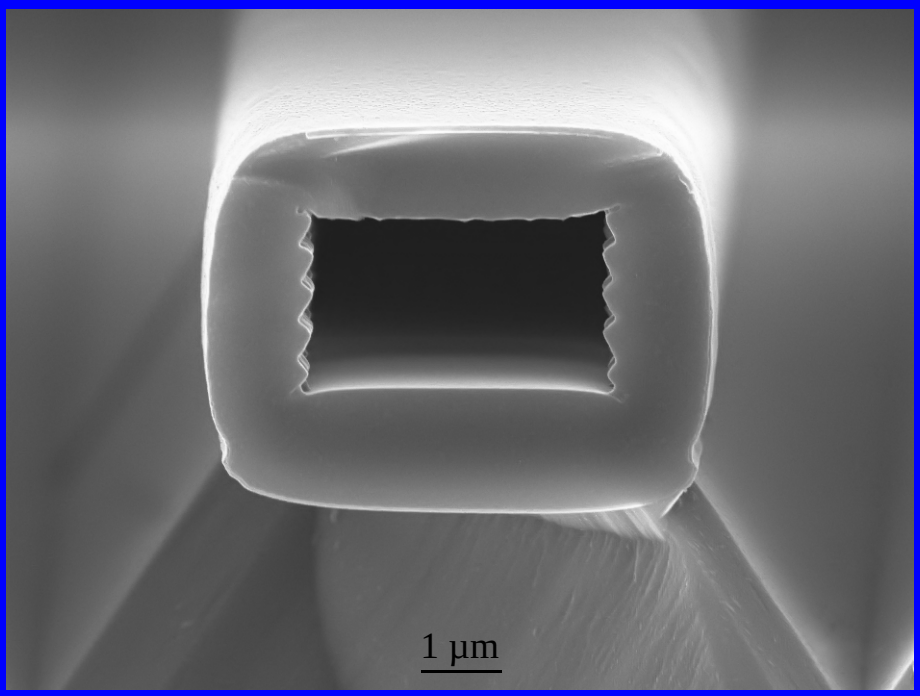

Friedjof C.A. Heuck

Developing and Analysing sub-10 µm Fluidic Systems with Integrated Electrodes for Pumping and Sensing in Nanotechnology Applications

Proefschrift

ter verkrijging van de graad van doctor
aan de Technische Universiteit Delft,
op gezag van de Rector Magnificus prof. ir. K.C.A.M. Luyben,
voorzitter van het College voor Promoties,
in het openbaar te verdedigen op donderdag 28 oktober 2010 om 14:00 uur
door

Friedjof Carl August HEUCK
Diplom Ingenieur (Universiteit Freiburg, Duitsland)

geboren te Seeheim-Jugenheim, Duitsland

Dit proefschrift is goedgekeurd door de promotor:
Prof. dr. U. Staufer

Samenstelling promotiecommissie:

Rector Magnificus	Vorzitter
Prof. dr. U. Staufer	Technische Universiteit Delft, promoter
Prof. dr. S. Verpoorte	Rijksuniversiteit Groningen
Prof. dr. N.F. de Rooij	École Polytechnique Fédéral de Lausanne, Zwitserland
Prof. dr. G. Schitter	Technische Universiteit Wenen, Oostenrijk
Prof. dr. P.M. Sarro	Technische Universiteit Delft
Prof. ir. R.H. Munnig-Schmidt	Technische Universiteit Delft
Prof. dr. P.J. French	Technische Universiteit Delft

ISBN: 978-90-9025774-7
Copyright 2010 by F.C.A. Heuck
All rights reserved. No part of the material protected by this copyright notice may be reproduced or utilized in any form or by any other means, electronic or mechanical, including photocopying, recording or by any other information storage and retrieval system, without the prior permission of the author.

To my strong & growing family network

Abstract

In this thesis, sub-10 µm fluidic systems, with integrated electrodes for pumping and sensing were developed and analysed for nanotechnology applications. This work contributes to the development of the scanning ion pipette (SIP), a tool for investigating surface changes on the nanometer scale induced by locally administering chemically or bio-active solutions. For this purpose, the already existing technology of a micropipette integrated into a scanning force microscope (SFM)-chip was enhanced by implementing electrodes for on-chip electrochemical sensing and electroosmotic (EO) pumping. The integration of an EO pump will offer the possibility of storing, selecting and dispensing multiple different liquids with the SIP chip. For a high density and convenient electronic integration, an EO pump within a small footprint (less than 100 µm × 100 µm) and low actuation voltage (less than 10 V) had to be developed.

The microfabrication of the SIP was based on standard micromachining from well established MEMS processes. These processes were adapted to build a network of sub-10 µm capillaries with a complex geometry, freestanding cantilever and tip. To gain a first experience with these small capillary dimensions, the integration of an evaporation based micropump into the SIP was investigated. Since its actuation did not require any electrodes, it was straightforward to implement it into the SIP fabrication. The result was a unidirectional pump, which could be controlled by the temperature of the evaporation area. The evaporation induced flowrate was experimentally determined to range from 7 $pl \cdot s^{-1}$ at 23° C up to 53 $pl \cdot s^{-1}$ at 65° C.

A more advanced bidirectional EO pump with platinum (Pt) electrodes was fabricated based on a simplified process with comparable SIP capillary dimensions. The Pt electrodes required a SIP specific on-chip design to ventilate the emerging electrolyzed gases by a novel liquid-gas (LG) separator. This LG-separator parted the gas bubbles from the liquid and guided them away from the EO pump. Its operation principle was solely based on the geometry of a tapered capillary sidewall, taking advantage of the high capillary pressure occurring in these small dimensions. In the experimental analysis, the LG-separator was able to reliably separate and ventilate an emerging gas flow of 2 $pl \cdot s^{-1}$. The dispensing flow of the EO pump was measured to be 50 $pl \cdot s^{-1}$ at an actuation voltage of 5 V.

The performance and integration of a second type of electrodes, based on silver/silver chloride (Ag/AgCl), into the SIP was investigated. These electrodes had the outstanding advantage, that during electrode actuation, the electrochemical reaction continued to transform Ag into AgCl and vice versa, rather than electrolyzing the liquid. Moreover, these electrodes could be integrated in a post-fabrication step of the SIP capillary, circumventing electrode instability caused by the high temperature oxidation step needed to form the silicon dioxide (SiO_2) of the capillary sidewalls. After the SIP capillary fabrication, the adhesion between the SiO_2 capillary sidewall and the Ag layer was improved by a polymeric 3-mercaptopropylmethyldimethoxy silane layer deposited out of the gas phase. Afterwards, an Ag layer was electrolessly grown on the sidewall of the closed microfluidic capillaries, based on a modified Tollen's reagence. The deposited Ag layer had an

experimentally deduced high specific conductivity of 6×10^7 $S \cdot m^{-1}$, indicating a high purity and density. The successful structuring of the Ag electrodes inside the SIP was achieved by controlling the capillary-filling with the electroless solution by using microfluidic stopvalves. For the final device, these stopvalves were filled in a void free way by changing the solution's surface tension. Finally, the Ag electrode was electrolessly transformed into an Ag/AgCl electrode. These electrodes were used to electrochemically measure different pH values, where a linear pH sensitive of 57.4 $mV \cdot pH^{-1}$ at 22.7° C was achieved. Furthermore, an EO pump was built with these electrodes integrated into a polymeric fluidic system (capillary cross section 55 µm × 65 µm). The pump rate of this device was determined to be 0.12 $nl \cdot s^{-1} \cdot V^{-1}$.

Experiments with the SIP for imaging and dispensing were performed. The imaging capabilities were illustrated by imaging in tapping mode a fixed and dried Escherichia Coli bacteria. The obtained images had a reasonable quality and resolution. Moreover, no special skills in operating the SFM were required since it did not perform differently with a mounted SIP than with a mounted standard commercially available SFM sensor chip.

Developing and Analysing sub-10 µm Fluidic Systems with Integrated Electrodes for Pumping and Sensing in Nanotechnology Applications

Abstract i

1 Introduction 1

1.1 Motivation and state of the art 1
1.1.1 Liquid dispensing with scanning force microscope enhanced micropipettes 1
1.1.2 Sensing with scanning force microscope enhanced micropipettes 4
1.2 Structure of the thesis 6
1.2.1 Fabrication of the scanning ion pipette 6
1.2.2 Evaporation induced pumping within the scanning ion pipette 6
1.2.3 Electroosmotic pumping with Pt electrodes 6
1.2.4 Integration of Ag electrodes into the scanning ion pipette 7
1.2.5 Electroosmotic pumping and electrochemical sensing with Ag/AgCl electrodes 7
1.2.6 Imaging and dispensing with the scanning ion pipette 7
1.3 Theoretical background of the thesis 8
1.3.1 Microfluidics 8
1.3.2 Scanning force microscopy 11
1.3.3 Microfabrication 12

2 Fabrication of the scanning ion pipette 13

2.1 Process flow 13
2.1.1 Fluidic-system-wafer 13
2.1.2 Base-wafer 14
2.1.3 Bonded wafers 15
2.2 Design considerations and fabrication results 16
2.2.1 Overall dimensions 16
2.2.2 Cantilever and tip 17
2.2.3 Fluidic system 18
2.2.4 Specific design for anisotropic KOH etching 19
2.2.5 Remarks on silicon direct bonding 21
2.3 Laboratories involved 21
2.4 Conclusions and outlook 22

3 Evaporation induced pumping within the scanning ion pipette 23
3.1 Theory of evaporation induced pumping in microcapillaries 24
3.2 Experimental 25
3.2.1 Design of the scanning ion pipette with an integrated evaporation based pump 25
3.2.2 Instrumentation and method 26
3.3 Results and discussion 27
3.3.1 Verification of the measurement method 27
3.3.2 Deduction of the model parameters 28
3.3.3 Temperature dependent pump rate 29
3.4 Conclusions and outlook 30

4 Electroosmotic pumping with Pt electrodes 31
4.1 Model of an electroosmotic pump with a liquid-gas-separator 32
4.1.1 Model of the liquid-gas-separator 32
4.1.2 Model of the complete fluidic system 39
4.2 Fabrication 42
4.2.1 Process flow 42
4.2.2 Fabrication results and discussion 43
4.3 Experiments, results and discussion 45
4.3.1 Liquid-gas-separator 45
4.3.2 Electroosmotic flow determination 47
4.4 Summary and conclusions 50
4.5 Outlook 51
4.5.1 Model of an electroosmotic pump integrated into the scanning ion pipette 51
4.5.2 Electrodeposition inside closed capillaries 52

5 Integration of Ag electrodes into the scanning ion pipette 53
5.1 Experimental 53
5.1.1 Intermediate polymeric-mercapto-silane layer 53
5.1.2 Electroless Ag deposition 54
5.1.3 Configuration of the Ag electrode by microfluidic structures 55
5.2 Process characterization, results and discussion 58
5.2.1 Intermediate polymeric-mercapto-silane layer 58
5.2.2 Electroless Ag deposition 59
5.2.3 Microfluidic structuring of the Ag layer 62
5.3 Summary and conclusions 64

6 Electroosmotic pumping and electrochemical sensing with Ag/AgCl electrodes 65
6.1 Design 65
6.2 Process flow 66
6.3 Fabrication results and discussion 68
6.3.1 Microfluidic NOA63/glass capillary 68
6.3.2 Electroless Ag deposition 69
6.3.3 Electroless Ag transformation into AgCl 70
6.4 Electroosmotic flow measurement 72
6.4.1 Electroosmotic induced speed of the microspheres 73
6.4.2 Electrophoretic induced speed of the microspheres 74
6.4.3 Combined velocity of the microspheres 75
6.5 Electrochemical measurement 75
6.6 Conclusions and outlook 75

7 Imaging and dispensing with the scanning ion pipette 77
7.1 Scanning force microscopy imaging with the scanning ion pipette 77
7.2 Fluid dispensing with the scanning ion pipette 78
7.2.1 Interface: scanning ion pipette and scanning force microscope holder 78
7.2.2 Sealing agents and procedure 79
7.3 Dispensing results and discussion 80
7.4 Summary and conclusions 81
7.5 Outlook: Alternative sealing approach 82

8 Conclusions and recommendations 85
8.1 Conclusions 85
8.2 Recommendations 87

9 References 89
9.1 Introduction 89
9.2 Fabrication of the scanning ion pipette 91
9.3 Evaporation induced pumping within the scanning ion pipette 92
9.4 Electroosmotic pumping with Pt electrodes 92
9.5 Integration of Ag electrodes into the scanning ion pipette 93
9.6 Electroosmotic pumping and electrochemical sensing with Ag/AgCl electrodes 96
9.7 Imaging and dispensing with the scanning ion pipette 97
9.8 Conclusions and recommendations 97

Summary **99**

Samenvatting **103**

Nomenclature **107**

Curriculum vitae & list of publications **111**

Acknowledgments **115**

Chapter 1

Introduction

At the end of the 19th century Robert Koch and Louis Pasteur proposed the germ theory of disease verifying that microorganisms were the source of many diseases. This was considered as a milestone for modern medicine. In order to verify and further develop the germ theory, individual microorganisms had to be isolated, picked up from a culture media and implanted into animals. Already at this time, micropipettes with an extremely fine aperture, were successfully pulled out of glass capillaries using a standard Bunsen burner. Further developments in mounting these micropipettes on precise and fine motion translation stages enabled Marshall Barber in 1911 to insert substances into bacterias and living cells [1].

Nowadays, one of the main driving forces to improve micropipette techniques still remains in the field of medicine; more specifically in bio-molecular recognition, including protein identification, DNA sequencing and combinatorial drug testing. This is usually performed with so called antibody arrays, containing several hundred thousands of active spots. Due to the high amount of spots required, a further miniaturization of these arrays is desired and offers several advantages: The high density of active spotsize reduces the overall chip size drastically; hence, a smaller sample volume is required and in addition the probability of interaction between the proteins and their corresponding antibodies is increased. This leads to a faster reaction, which implies less time required for the identification. In 2007, Wingren and Borrebaeck [2] formulated the requirements for a miniaturization towards high density nano arrays as an active spotsize in the range of 1 µm resulting theoretically in a maximum array density of 10^6 probes·mm^{-2} and preferably 10^4 spots of different activity.

1.1 Motivation and state of the art

1.1.1 Liquid dispensing with scanning force microscope enhanced micropipettes

The successful printing of these arrays with micropipettes encourages the development towards increased printing speed and smaller spotsize by downscaling the pipettes. In this approach, the most challenging hurdle is the high amount of diverse printing liquids to achieve different active spots. The first improvement to meet these small scale printing requirements was to enhance the micropipette with precise and high resolution motion of a scanning force microscope (SFM) [3]. Five different approaches to dispense fluids in the sub micrometer scale with a SFM have been under current development. Their corresponding sketches are shown in Fig. 1.1. (a) Dip pen nanolithography (DPN) is defined by using SFM probes coated with the desired printing material [4-12]. (b) DPN was improved by continuously supplying liquids through a fluidic connection from a large reservoir via a hollow cantilever to an outlet hole in the tip. The sharp tip was placed in the center of the outlet hole in the nano fountain probe (NFP) [13-15]. (c) Comparable to DPN, an apertured hollow tip was used for nanoscale dispensing (NADIS) [16-19]. (d) Similarly, to improve NADIS with a continuous supply of liquid, a fluidic connection from a reservoir to an outlet

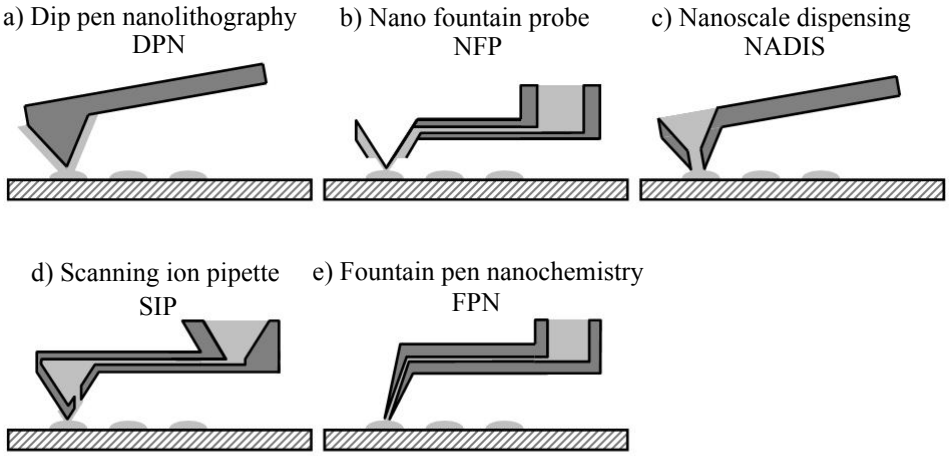

Fig. 1.1 (a) Dip pen nanolithography (DPN) is defined by using SFM probes coated with the desired printing material. (b) DPN was improved by continuously supplying liquids to an outlet hole in the tip. The sharp tip was placed in the center of the outlet hole in the nano fountain probe (NFP). (c) Comparable to DPN, an apertured hollow tip was used for nanoscale dispensing (NADIS). (d) Similarly, NADIS was improved by continuous supply of liquid to an outlet hole in the tip. In this case, the outlet hole was placed in close vicinity to the tip of the scanning ion pipette (SIP). (e) Instead of using microfabrication technology as the previously mentioned approaches, the fountain pen for nanochemistry (FPN) was based on pulled glass pipettes.

hole in the tip was designed. In this case, the outlet hole was placed in close vicinity to the tip of the scanning ion pipette (SIP) [20-23]. (e) Instead of using microfabrication technology as the previously mentioned approaches, the fountain pen for nanochemistry (FPN) was based on pulled glass pipettes [25, 26].

One of the first techniques invented was DPN in 1999. The mechanism of liquid transfer to the sample was divided into two steps in the DPN technique. Before printing, the tip was dipped into the liquid to be printed, the so called ink. It consisted of desired molecules and a corresponding solvent. The ink formed a thin layer by physisorption on the tip surface without changing its geometry. As soon as the sharp tip was in contact with the sample surface, the molecules started to diffuse from this point-contact over the surface, forming a monolayer [7]. This enabled to print very well defined and small sized spots in the range of several tens of a nanometer [5]. The formation of the ink layer on the tip, the loss in ink layer thickness due to the evaporation of the solvent, and the diffusion of ink on both surfaces, the tip and the sample, were crucial parameters for the smallest feature size and the printing speed. Therefore, DPN was performed in environmentally controlled chambers (humidity, temperature and airflow). First reported experiments with DPN technique were printed lines with a minimum width of 30 nm of 1-octadecanethiol molecules on a gold surface [5]. In order to increase the printing speed, two-dimensional arrays of up to 10 × 10 DPN polymer tips were fabricated by microfabrication. The minimum feature size achieved by printing with this DPN polymer tip array still remained in the sub-100 nm domain [12]. The drawback of the array DPN technique was that individual tips could not be addressed. In general, once the complete ink adsorbed on the DPN tip surface vanished, the DPN tip needed to be re-inked and re-positioned on the sample to continue the printing process.

The discontinuity in printing, due to re-inking the tip in DPN, was overcome in 2006 by the NFP technique. A continuous supply of ink was achieved by an outlet hole in the tip and a capillary connection to a large reservoir on the backside of the NFP chip. In order to

maintain the high resolution writing capabilities of DPN, the sharp tip was kept as a point-contact and it was surrounded by the capillary outlet. The mechanism of the liquid transfer to the sample was rather complex compared to DPN. Next to the diffusion process, condensation and recondensation of the ink in close vicinity to the capillary outlet occurred [4]. The NFP was also operated in an environmentally controlled chamber, in order to manage the wetting of the tip and the evaporation of solvent through the outlet. To increase the writing speed, an array of 12 cantilevers was manufactured, with each an individual reservoir for an eventually different ink. One of the main challenges in the operation of cantilever arrays is the precise individual tip sample distance control. In these experiments, only one cantilever was monitored by the feedback system of the SFM. The remaining cantilevers were expected to interact with the sample surface in the same manner. Writing tests were performed with an ink consisting of 16-mercaptohexadecanoicacid dissolved in acetonitril. A line with a width of 78 nm was reliably printed with a speed of 15 $\mu m \cdot min^{-1}$ [14].

In the NADIS technique, the small available ink volume stored on the DPN tip surface was increased by fabricating a hollow tip. In order to contact the sample surface, an apertured outlet hole was milled at the tip apex. The ink was placed as a droplet on the backside and capillary forces kept the ink inside the hollow tip. Once the tip touched the sample surface, a meniscus was shaped around the apertured outlet hole. Receding the tip from the sample surface broke the meniscus and left a droplet of ink behind. Also in the NADIS technique, the environmental conditions were controlled. In order to reduce evaporation, especially, from the large ink's liquid-air interface at backside of the tip, the NADIS probe was filled with less volatile ink solvents. The evaporation of the solvent had a strong influence on the dimensions of the meniscus around the aperture hole. Furthermore, the printing conditions changed over time due to evaporation of the ink's solvent. This resulted in an increasing concentration of dissolved dispensing molecules. Writing experiments were performed with glycerol on a polished silicon wafer with a native silicon dioxide layer on top. Ink volumes of 40 al were dispensed in 0.5 s. One filling of the NADIS probe was able to dispense more than 1000 of such droplets [17].

Comparably to NFP technique, the SIP improved the NADIS technique for continuous printing. In contrast to NFP, the SIP used silicon dioxide capillaries and cantilevers with larger hydraulic cross sections, except in Deladi et al. [21, 22]. The apertured outlet hole was fabricated individually by focussed ion beam milling. The advantage of focussed ion beam milling was that the outlet hole could be placed at the tip apex like NADIS or in close vicinity to the tip apex like NFP. Writing experiments were performed in water to avoid inadequacies due to evaporation. This idea can be further improved by dispensing in a non miscible surrounding liquid like water based inks in an oil based surrounding liquid. This would result in a well defined smaller ink meniscus shape for high resolution printing. Spots of streptavidin in HEPES were printed on a functionalized surface with a copolymer of polylysine and polyethylenglycol. The resulting spot diameter was 3 µm at an aperture hole of 1 µm. The dispensing was initiated by applying externally a pressure pulse of about 2 mbar for 2-3 s [23]. Furthermore, a similar experiment to the one of Barber [1] was performed with the SIP to selectively introduce a fluorescent dye into the cell [24].

The micropipettes employed in the FPN technique were pulled capillaries instead of microfabricated ones. The obtained capillaries had an outer diameter of 10 nm and an interior diameter as small as 3 nm at the tip. The capillary was filled by capillary force and connected to an external pressure source. At the tip of the capillary, a small droplet formed, which was shaped and hold in place by the surface tension of the liquid and the amount of externally

applied pressure. As soon as the capillary was in contact with the sample, a meniscus formed around the outer diameter of the tip. In order to avoid the drying of the liquid and, as a consequence, the clogging of the capillary, the FPN needed to be operated at absolute humidity. The liquid dispensing properties of the FPN were demonstrated by etching a 0.1 µm wide line into a 120 nm thick chromium layer [25]. The applicability to print high density arrays seems to be limited since each capillary had to be fabricated and mounted individually.

1.1.2 Sensing with scanning force microscope enhanced micropipettes

SFM enhanced micropipettes not only allow high precision dispensing, they can also be used for scanning force microscopy imaging. Table 1.1 gives a short overview of the scanning force microscopy imaging characteristics of the previously mentioned SFM enhanced micropipettes. The differences in the scanning force microscopy imaging characteristics originate mainly in the application, specific design and fabrication process.

Tabel 1.1: Scanning force microscopy imaging characteristic

	DPN [6]	Polymer DPN [12]	NFP [13, 14]	SIP [20, 24]	FPN [25]
Cantilever stiffness [$N \cdot m^{-1}$]	0.05	n.a.	0.03-0.3	0.1	0.1-10
Tip radius [nm]	10	70	250	200	10

In case of DPN, conventional commercially available SFM chips were used [6], whereas for polymer DPN, the stiffness of the cantilever was replaced by a soft elastic polydimethylsiloxane tip with a height in the range of 15 µm [12]. For NFP and SIP, the optimal design for the hollow cantilever implied a trade off between the hydraulic properties and sealing versus a low cantilever stiffness. The complexity of the microfabrication process resulted in a comparatively large tip radius for the NFP technique. In case of SIP, the tip radius was defined by silicon nitride molding of a pyramidal etched pit in monocrystalline silicon [20, 21]. It is expected that by thermal oxide sharpening, the tip radius can be reduced to about 10 nm [27].

SFM enhanced micropipettes allow a combination of dispensing and imaging together with the highly sensitive force feedback of the SFM. This has the unique advantage that small amount of liquid can be dispensed at specific locations of interest on the surface. In a series of experiments this capability proved to be crucial to distinguish between gently imaging the membrane of a living cell and, if desired, to perforate the cell membrane and insert substances into the cell body [24]. In contrast to this approach, Korchev et al. [28] employed conventionally pulled microcapillaries to determine the distribution of ion conductive channel proteins. For this, they used a combination of the patch clamp technique [29] and scanning ion conductance microscopy [30]. A micropipette has the distinct advantage of dispensing highly localized bio-active solutions stimulating and enhancing the ion transfer through the channel proteins. Therefore, they replaced the usually employed conductive tips by micropipettes for the scanning ion conductance microscopy. During these experiments, the ion current was measured while the surface topography was scanned. An overlay of the ion current image with the topography image allowed the identification of channel proteins within the cell membrane. Microfabricated SFM enhanced pipettes like NFP or SIP would facilitate those measurements by using conventional scanning force microscopes. Therefore, they need to be further developed with the integration of an electrode, preferably at the tip.

So far, the discussion of SFM enhanced micropipettes was only on dispensing liquids and scanning force microscopy imaging. Following the approach from Barber in 1911 [1], SFM enhanced micropipettes can also be used to aspirate samples at highly localized positions. These samples can then be further transferred to an external analyzer via a capillary connection. Until now, no publications of the NFP or SIP were found reporting any aspiration based research. This approach would be very useful in combinatorial screening, especially with the new solid state materials used, since it offers an attractive method to identify the composition with the highest catalytic activity. Cong et al. [31] determined the optimal material configuration by creating a large array of spots with different catalysts compositions. Each spot was separately heated to the desired temperature while the gas mixture was sampled by placing a conventionally fabricated suction capillary right above it. The gas mixture was then further analysed in the mass spectrometer to assess the level of catalytic activity. Instead of investigating different catalytic compositions, Jambunathan et al. [32] used a similar approach to determine the influence of different crystallographic orientations and local poisoning on the catalytic activity. Miniaturizing the suction capillary would allow a smaller spot size (currently 1.5 mm) and a faster analysis due to a higher localization of the detection (currently 1 min. each spot) [31]. Especially, in the domain of crystallographic surfaces a small suction aperture and a high precision scanning would be favorable.

The SFM enhanced micropipette could also be extended to provide on-chip analysis of the aspirated solution. In the works of Braun et al. [33] and Burg et al. [34, 35], the mass of bio-molecules was determined by the high resonating quality of a cantilever. Slight changes in the cantilever mass directly translated into a shift in resonance frequency. The cantilever mass changed due to adsorption of bio-molecules out of the solution. In this research, the mass was resolved down to 1 ng [33]. Even higher resolutions, up to 0.3 fg, were achieved by resonating microchannels in vacuum [35]. Commonly known techniques from lab-on-a-chip or micro-total analysis systems could also be used to analyze the aspirated solution of different bio-molecules. The solution of bio-molecules can be separated by, already existing, systems such as capillary electrophoresis. The final identification can be performed by either amperometric [36, 37] or cyclic voltammetry detection [38]. For further development towards on chip analysis, the previously mentioned techniques can be integrated into the SFM enhanced micropipette chips.

As it turns out, a promising direction for a further development of the SFM enhanced micropipette is towards an on-chip integrated fluid electrochemical SFM. The first step would be to integrate electrohydrodynamic pumping, i.e. based on electroosmotic (EO) pumping. This on-chip pumping removes bulky and leakage affected fluidic connection between the SFM and the SFM enhanced micropipette. Importantly, a high variety of different liquids, individually on-chip stored, can be addressed and dispensed through the tip. The next step comprises the improvement towards electrochemical sensing, as previously discussed. To increase sensitivity and decrease the measurement time, a placement of the sensors as close as possible to the tip would be preferable. Finally, it is important to keep in mind that regardless of the fabrication complexity, a SFM enhanced micropipette remains a disposable laboratory accessory. Wear on the sharp tip and cross contamination require a frequent exchange. Even though parallel batch microfabrication may reduce the price, costs remain a critical factor for its success.

1.2 Structure of the thesis

At the beginning of this thesis the fabrication of the SIP was previously developed by Hug et al. [20]. Here, strategies to integrate different electrodes, platinum (Pt), silver (Ag) and silver chloride (AgCl), into the SIP were developed. With these electrodes experiments for EO pumping and electrochemical sensing were performed. This can be considered as the first step towards the integrated fluid electrochemical SFM.

1.2.1 Fabrication of the scanning ion pipette

In this chapter, an extensive and detailed analysis of the important design guidelines and fabrication steps is presented. As a general overview, the capillaries, the cantilever and tip were outlined as top open surface trenches in one wafer. Into another wafer, holes serving as connections were etched through the complete cross section. For assembling, the two wafers were aligned, in such a way that the trenches of the first wafer were connected to the through wafer connections of the second wafer. Afterwards, the two wafers were bonded together by silicon direct bonding and fuse bonding in an oxidation atmosphere. This step capped the trenches at the bonding interface. In order to release the cantilever and to have full optical access to capillaries, the surrounding Si was removed from the side of the first wafer. Finally, the opening of the fluidic system at the tip was drilled by a focussed ion beam. This fabrication process was highly versatile with regards to the capillary geometry, allowing the layout of a complex fluidic system into the SIP.

1.2.2 Evaporation induced pumping within the scanning ion pipette

Evaporation induced pumping represents a straightforward implementation of a micropump into the SIP. The working principle of an evaporation based micropump is as follows: The hydrophilic capillaries of the SIP are filled instantaneously with a water based solution. Once the fluid reaches the capillary outlet, it starts evaporating. The capillary pressure keeps the outlet of the capillaries wetted, and thereby, replaces autonomously the evaporation loss by drawing additional water through the capillaries. This results in a unidirectional pump, which for instance can be used to suck in liquids through the tip‘s hole and concentrate them inside the outlet of the capillaries. The implementation of such a pump does not require any additional fabrication step of the SIP. Only the geometry of the capillary outlet area needs to be increased to enhance the evaporation induced pumping. In this chapter, the pumping effect is modelled and verified with experiments. Evaluating the evaporation pump was one of the first experiments, it helped to develop a feeling and understanding of the challenges imposed by the dimensions of the SIP capillaries, with a cross section of less than 10 μm^2.

1.2.3 Electroosmotic pumping with Pt electrodes

In order to achieve bidirectional active pumping, the SIP is extended with an EO pump. A general encountered problem with the design of EO pumps is the coupling of the electrical current into the ionic solution, which is commonly done with electrodes made out of Pt. However, using Pt electrodes inherently implies that the electrochemical transfer of electrons from the electrode into the solution initiates electrolysis of the liquid into gas. These gases emerge as bubbles and may block the conductive path between the electrodes and, hence, inhibit a further actuation of the pump.

In this chapter, the design and analysis of an EO micropump with Pt electrodes is presented. The mixing of electrolyzed gases with the functional fluidic system is avoided by

a novel concept of a liquid-gas separator. This liquid-gas separator is placed between the electrodes and the EO pump driving the emerging gas bubbles away, via an exhaust capillary. In order to identify and verify the optimal design of an EO pump for dispensing and sucking liquids into the SIP, the fabrication process was simplified. Instead of thermal fusion bonding, low temperature anodic bonding was used to fabricate the capillaries. Nevertheless, an integration of the Pt electrodes into the original SIP fabrication process seems feasible, due to the high melting temperature of Pt. During the thermal oxidation sufficiently thick Pt electrodes are stable and do not degrade because of surface diffusion [39].

1.2.4 Integration of Ag electrodes into the scanning ion pipette

In order to avoid the electrode instability during the thermal fuse bonding of the SIP fabrication, highly conductive Ag electrodes are deposited as a post SIP fabrication process. Especially, Ag can be used as a metal for electroless deposition. This technique provides a unique and highly flexible method to deposit and structure metal films inside closed capillaries. The idea behind it is to fill a solution of Ag ions as well as a reducing agent into the capillaries. During the electrochemical reaction, the Ag layer starts to grow on the sidewall of the capillary forming the Ag electrode. Simultaneously, the Ag layer is structured by controlling the capillary filling of the electroless Ag solution to certain parts of the fluidic system, e.g. by means of a microfluidic stopvalve. In this chapter, the composition of the electroless Ag solution is analysed based on morphology, thickness and conductivity of the deposited electrode. Furthermore, the electrode structuring by a microfluidic stopvalve is modelled. Finally, a deposition of independent electrodes inside the SIP capillaries is shown.

1.2.5 Electroosmotic pumping and electrochemical sensing with Ag/AgCl electrodes

Taking the process of electroless Ag deposition and further transforming the Ag layer partially into AgCl, allows the fabrication of Ag/AgCl electrodes. These electrodes have the outstanding advantage that during pumping, the electrochemical reaction transforms Ag into AgCl and vice versa, rather than electrolyzing the liquid. Hence, liquid-gas separators for the ventilation of the emerging electrolyzed gases during EO pumping, as required for Pt electrodes, can be omitted. Furthermore, Ag/AgCl electrodes are the most common and well understood electrodes for biological and chemical measurements [40]. This chapter presents the design, fabrication and experimental analysis of Ag/AgCl electrodes for EO pumping and electrochemical sensing.

1.2.6 Imaging and dispensing with the scanning ion pipette

First, experiments with the SIP for imaging and dispensing were performed. In order to get a first hand-on experience, a less delicate sample, in less challenging conditions, was chosen, than anticipated for the expected SIP imaging of a living cell. The imaging capabilities were illustrated by imaging in tapping mode a fixed and dried Escherichia Coli bacteria. In case of dispensing with the SIP, no similar results as presented by Meister et al. [23] were achieved. This was mainly caused by leakage afflicted sealing between the SIP and the SFM holder. This, again, shows the necessity of improving SIP techniques towards autonomous on-chip fluid handling.

1.3 Theoretical background of the thesis

1.3.1 Microfluidics

In this section, only a brief discussion of the fluidic properties of the capillaries is presented, mainly to derive equations which are used in the following chapters. For more details please refer to microfluidic handbooks like the one of Bruus [41]. In general, three main assumptions can be taken, which facilitate the microfluidic modelling regarding the capillary dimensions and flows experienced in this thesis. First of all, the no-slip boundary condition defines the velocity of the liquid at the capillary sidewall to zero. The idea behind is that the momentum difference between the molecules of the liquid, which are close to the capillary sidewall, and the molecules of the wall, which do not move, diminishes within the range of the molecular mean free path of the liquid. In this thesis, mainly water was employed, which has an intermolecular distance well below 1 nm. Second, the flow within the capillary is expected to be laminar. This can be reasoned by a low Reynolds number $Re \equiv \rho_l v l_c / \eta$, where ρ_l, v, l_c and η represent the liquid density, the mean velocity, the characteristic cross sectional length of the capillary and the dynamic viscosity of the liquid, respectively. For a maximum characteristic cross sectional length of 20 µm and a maximum mean velocity of up to 1 mm·s^{-1}, the Reynolds number was $Re \ll 1$, indicating laminar flow. Third, in case of capillary forces, which are defined by the liquid-air interface, any influence from gravity can be neglected. This is expressed by the Bond number $Bo \equiv \rho g l_c^{\,2} / \gamma$, where g and γ represent gravity and the liquid-air surface tension, respectively. For the employed dimensions and water, the Bond number was $Bo \ll 1$, indicating the dominance of the capillary force.

Poiseuille flow in capillaries with a rectangular cross section

In order to define the hydraulic resistance R_{hy}, which is expressed by the relation between flow Q and pressure p, the Navier-Stokes equation under the condition for a pressure driven, steady state, laminar flow needs to be solved. This flow characteristic is also known as the Poiseuille flow, considering a long capillary with the length L and a rectangular cross section, width w and the height h, where $w > h$. The coordinate system is defined as such that the x-direction points along the length of the capillary and the y-direction defines the width w with its origin in the center of the capillary, $-0.5w \le y \le 0.5w$, and finally, the z-direction defines the height h with its origin at the bottom of the capillary, $0 \le z \le h$. Applying a hydrostatic pressure p_{hy} over the capillary causes a flow velocity field $v_x(y,z)$ over the capillary cross section which can be expressed as

$$0 = \eta \nabla^2 [v_x(y,z)] - \frac{p_{hy}}{L}. \tag{1.1}$$

Even though the rectangular cross section is highly symmetric, no analytical solution can be found. Solving Eq. (1.1), with a Fourier expansion under the no-slip condition results in the cross sectional velocity field $v_x(y,z)$ as

$$v_x(y,z) = \frac{4h^2 p_{hy}}{\pi^3 \eta L} \sum_{n,\,odd}^{\infty} \frac{1}{n^3} \left[1 - \frac{\cosh\left(n\pi \frac{y}{h}\right)}{\cosh\left(n\pi \frac{w}{2h}\right)} \right] \sin\left(n\pi \frac{z}{h}\right). \tag{1.2}$$

The flow rate Q is determined by the integration of the velocity field $v_x(y,z)$ over the cross section,

$$Q = 2\int_0^{0.5w}\int_0^{h} v_x(y,z)\,dz dy = \frac{h^3 w p_{hy}}{12\eta m L}\left[1 - \frac{192}{\pi^5}\sum_{n,\,odd}^{\infty}\frac{1}{n^5}\frac{h}{w}\tanh\left(n\pi\frac{w}{2h}\right)\right] \approx \frac{h^3 w p_{hy}}{12\eta L}\left[1 - 0.630\frac{h}{w}\right] \tag{1.3}$$

Out of this equation, the hydraulic resistance R_{hy} of a rectangular capillary with $w > h$ can be extracted

$$R_{hy} \approx \frac{h^3 w}{12\eta L}\left[1 - 0.630\frac{h}{w}\right]. \tag{1.4}$$

Capillary forces or Young-Laplace pressure at the liquid-air interface

The capillary pressure originates in the interaction forces at the interface between different materials, regardless their state of matter (solid, liquid or gas). The first step to built a model which quantitatively describes this interfacial interaction is to compare the molecular interaction inside one of the materials with the interaction at the interface. In the first case, inside the bulk of the material, the molecule is completely surrounded by molecules of the same type, with which it interacts and forms chemical bonds (not necessarily covalent bonds). In the second position, at the interface, this same molecule is now partially surrounded with molecules of the other type to which it also forms a chemical bond. In case the energy for the chemical bond between the two types of molecules differs, a separation, by establishing a well defined interface, is energetically preferred. This can be expressed by the surface tension γ. These phenomenons can be addressed with the thermodynamic description of Gibb's total free energy of the system *G*. In this, the surface tension γ is defined as the change of Gibb's free energy *G* per interfacial surface area *A* at fixed pressure *p*

$$\gamma \equiv \left.\frac{\partial G}{\partial A}\right|_p . \tag{1.5}$$

Usually, the temperature is an important parameter in the thermodynamic definitions. In the discussed circumstances of a microcapillary at least partially surrounded by a bulk silicon chip with a sufficient heat capacity and conductivity, a temperature change at the interface due to a change in Gibbs free energy is assumed to be insignificant. In order to comply with the minimum condition of the Gibb's free energy, which is demanded by thermodynamics, a so called Young-Laplace pressure p_c is required. This needs to compensate for changes δz in the interfacial surface area *A*,

$$\partial G = \partial G\big|_p + \partial G\big|_A = \gamma\delta A - A\delta z p_c = 0 . \tag{1.6}$$

It is assumed, that the interfacial surface area *A* can be described by the superposition of two different radii R_1 and R_2. An infinitesimal small change in radius by δz and neglecting higher order terms of δz results in

$$\delta A \approx \delta z\left(\frac{1}{R_1} + \frac{1}{R_2}\right)A . \tag{1.7}$$

With Eq. (1.6) and Eq. (1.7), the Young-Laplace pressure p_c can be isolated to

$$p_c = \gamma\left(\frac{1}{R_1}+\frac{1}{R_2}\right). \tag{1.8}$$

The last question to be answered in this section is, what happens at the point, where the interfaces of three different materials intersect, i.e. a gas bubble attached to the sidewall of the capillary. At one point the liquid gas circumference of the gas bubble touches the sidewall, forming the triple point. The angle at which the liquid gas interface intersects with the sidewall is the so called contact angle θ. Moving this triple point by the length δl into the gas bubble causes a change in the different interfacial surface areas represented by the surface tension γ. This can be expressed by the change in the total Gibb's free energy G,

$$\delta G = \gamma_{sl}\delta l - \gamma_{sg}\delta l + \gamma_{sg}\cos\theta\,\delta l = 0, \tag{1.9}$$

where the indice s, l and g represent solid, liquid and gas surface, respectively. Finally, Young's equation can be used to define the contact angle θ

$$\cos\theta = \frac{\gamma_{sg}-\gamma_{sa}}{\gamma_{lg}}. \tag{1.10}$$

Electroosmosis

The basic principal of electroosmosis is well explained in the papers from Zhou and Foley [42], as well as, Morf et al. [43], next to the microfluidic handbook from Bruus [41]. Electroosmosis describes an electric field induced movement of a liquid parallel to a charged surface. This can be especially exploited in the microfluidic domain as an EO micropump, since smaller capillary dimensions enhance surface interactions. For this purpose, the pumping solution containing dissolved ions at a specific pH value is filled into the silicon dioxide capillary of the SIP. At the silicon dioxide surface, the silanol groups (SiOH) are deprotonated into charged silanoate (SiO^-), in case the pH value is higher than the isoelectricpoint of the capillary surface. This surface charge σ_{ch} creates an electric field reaching into the solution. In there, the positive counterions of the solution are attracted and assembled at the surface in order to compensate for the negative surface charge σ_{ch}. These attracted ions form a so called electric double layer. The first layer of the double layer consists of immobile counterions, which are strongly attracted by the charged sidewall, the so called Stern layer [44], and the second layer consisting of diffuse loosely bound ions, the so called Gouy-Chapman layer. For the electroosmosis, the Stern layer does not contribute, since it is immobile, but its charge reduces the potential at the interface between the Stern layer and the Gouy-Chapman layer. This remaining potential is known as the ζ-potential. This drop of the ζ-potential within the Gouy-Chapman layer is responsible for the electrohydrodynamic interaction. With the Poisson-Boltzmann equation the exponential decay of the potential into the bulk of the solution can be described. This defines the thickness of the Gouy-Chapman layer, until the potential diminishes, this thickness is also known as the Debye layer thickness λ_D. The thickness of the Debye layer λ_D is a function of the temperature T, the valence Z of the counterions in solution and their concentration c_0. It can be approximated by the Debye-Hueckel approach to

$$\lambda_D = \sqrt{\frac{\varepsilon\varepsilon_0 k_B T}{2(Ze)^2 c_0}}, \tag{1.11}$$

where ε, ε_0, k_B and e denote the electrical permittivity of the solution, the electrical

permittivity of vacuum, the Boltzmann constant, and the elementary charge, respectively. This is valid within the limit of $Ze\zeta \ll k_B T$. Hence, the ζ-potential can be calculated to

$$\zeta = \frac{\sigma_{ch}\lambda_D}{\varepsilon\varepsilon_0}. \tag{1.12}$$

Assuming now, that an electric field E is applied parallel to the capillary sidewall, these positive ions start to move at the capillary surface and drag the bulk solution. The velocity of this electroosmotically induced flow v_{eo} can then be expressed by the Smoluchowski equation to

$$v_{eo} = \varepsilon\varepsilon_0\zeta\frac{E}{\eta}. \tag{1.13}$$

The effect of the electric field on flow is summarized by the EO mobility $\mu_{eo} = v_{eo}/E$, which can, therefore, be expressed by the Helmholtz-Smoluchowski equation to

$$\mu_{eo} = \frac{\varepsilon\varepsilon_0\zeta}{\eta} = \frac{\sigma_{ch}\lambda_D}{\eta}. \tag{1.14}$$

In order to design fluidic systems, the EO effect needs to be integrated into the fluidic quantities flow Q and the pressure p. Thus, the velocity profile of the EO flow is derived. The complete EO interaction is confined to the Debye layer λ_D. For the investigated capillary dimensions, the Debye layer λ_D is much thinner than the smallest dimensions of the capillary cross section, therefore, the velocity of the EO flow is assumed to be constant throughout the EO active capillary cross section A_c. Having a voltage drop U_{eo} over the length l_c of the EO active capillary leads to the EO flow Q_{eo}

$$Q_{eo} = v_{eo}A_c = \mu_{eo}A_c\frac{U_{eo}}{l_c} = \mu_{eo}\rho_{el}U_{eo}\frac{1}{R_{el}}, \tag{1.15}$$

where R_{el} represents the electrical resistance of the capillary $R_{el} = \rho_{el}l_c/A_c$, with the solution's specific electrical resistance ρ_{el}. Hence, the EO induced pressure p_{eo} can be calculated to

$$p_{eo} = Q_{eo}R_{hy} = \mu_{eo}\rho_{el}U_{eo}\frac{R_{hy}}{R_{el}}, \tag{1.16}$$

according to Eq. (1.4), and with the hydraulic resistance R_{hy} of the EO active capillary. Since the EO active capillary is integrated into a larger more complex fluidic system, hydrostatic pressure p_{hy}, induced for instance by the hydraulic resistance of the additional capillaries, need to be integrated. Due to the small capillary dimensions, the velocity profile $v(x,y)$ over the capillary cross section is a superposition of the constant EO velocity v_{eo} and the hydrostatic laminar velocity $v_{hy}(x,y)$, $v(x,y) = v_{eo} + v_{hy}(x,y)$. According to Eq. (1.3), this yields to a flow Q through the EO active capillary

$$Q = \frac{p_{eo} + p_{hy}}{R_{hy}}. \tag{1.17}$$

1.3.2 Scanning force microscopy

A brief introduction into the scanning force microscopy is given here, for more detailed description please refer to [3, 45, 46]. The SFM-sensor chip consists of a cantilever with a tip at its end. In contrast to standard optical microscopy where the individual pixel values of the

image are obtained in parallel, in scanning force microscopy the pixel values are individually determined by scanning the tip over the sample surface. For this purpose, the sharp tip, with a radius in the range of nanometers, is brought in close proximity to the surface. In this close vicinity, attractive forces like van der Waals forces cause an interaction between the tip and the surface and the soft cantilever (stiffness in the range of 0.01 $N \cdot m^{-1}$ - 0.1 $N \cdot m^{-1}$) [47] is slightly deflected. This deflection is typically measured optically. For this purpose, a laser beam is reflected from the backside of the tip onto a position sensitive photo array. In order to keep the deflection of the cantilever low and to avoid crushing the tip into the sample surface, the SFM is usually operated in a feedback configuration. While scanning over the surface, the deflection of the cantilever is kept constant by continuously adjusting the tip sample distance. The image of the adjusted distance is, then, further transformed into a scanning force map by knowing the stiffness of the used cantilever. On specific surfaces and under good scanning conditions, a resolution down to the atomic level can be reached [48].

In this thesis, for SFM enhanced micropipettes, specially shaped hollow cantilevers were employed. To calculate the cantilever stiffness, the second moment of area I in the height direction z is required:

$$I_z = \frac{1}{12}(w_o h_o^3 - w_i h_i^3), \tag{1.18}$$

where w_o, h_o, w_i and h_i represent the width and the height of the outer dimensions, as well as width and the height of the inner hollow dimensions, respectively. For small tip sample interaction forces, the clamped cantilever beam acts like a spring with a cantilever stiffness k using Eq. (1.18)

$$k = Y\frac{3I_z}{L^3} = Y\frac{(w_o h_o^3 - w_i h_i^3)}{4L^3}, \tag{1.19}$$

where Y and L represent the Young's modulus and the cantilever length, respectively.

1.3.3 Microfabrication

Only a brief summary of the microfabrication processes used in this thesis is given. For further information please refer to the handbooks for microfabrication [49-51]. In case a more detailed description is required, it is presented in the respective chapter. For photolithography, a standard photolithography aligner was mainly employed. In case a higher resolution was required, a mask stepper was used. The pattern was transferred into layers or into the bulk with two different dry etching techniques; Isotropic reactive ion etching (RIE) was used for layer or shallow trenches into bulk of the silicon (Si) wafer and anisotropic deep reactive ion etching (DRIE) was used for deep trenches into the bulk of the Si wafer. Different wet etching techniques were required. Potassium hydroxide (KOH) or tetramethylammonium hydroxide (TMAH) anisotropically removed Si selectively to silicon dioxide (SiO_2) and silicon nitride (Si_3N_4). Buffered hydrofluoric acid (BHF) removed isotropically SiO_2 selectively to Si and Si_3N_4. Phosphoric acid (H_3PO_4) removed isotropically Si_3N_4 selectively to Si and SiO_2. SiO_2 was thermally grown on Si. Si_3N_4 layers were deposited by either low pressure (LPCVD) or plasma enhanced chemical vapor deposition (PECVD).

Chapter 2

Fabrication of the scanning ion pipette

This chapter presents an extensive and detailed analysis of the scanning ion pipette (SIP) fabrication. This process was highly versatile and allowed the layout of a complex capillary network to form fluidic systems. These capillaries consisted of silicon dioxide (SiO_2), which made the system highly hydrophilic and facilitated optical access to observe fluidic filling effects inside the capillary. In addition, with this process a freestanding cantilever including a sharp tip was created which was suitable for scanning force microscope (SFM) imaging.

2.1 Process flow

The fabrication of the SIP was based on standard bulk micro-machining from well established MEMS processes. The main innovation, previously developed by Hug et al. [52, 53], was to fabricate closed, partially freestanding capillaries by separating the design over two wafers: the fluidic-system-wafer and the base-wafer. The fluidic-system-wafer incorporated the fluidic system e.g. the cantilever and the tip in case of the SIP. They were outlined as shallow top open trenches. The base-wafer incorporated the fabrication frame, the chip outline, and the chip's handling part, as well as the reservoir implemented as a fluidic through wafer connection. They were fabricated as deep bulk trenches and connections through the complete wafer cross section. For assembly, the two wafers were aligned in such a way that the trenches of the fluidic-system-wafer were connected to the through wafer connections of the base-wafer. Afterwards, the two wafers were bonded together by silicon direct bonding and fuse bonding in an oxidizing atmosphere. This step capped the trenches of the fluidic system at the bonding interface. In order to release the cantilever and to have full optical access to the fluidic system, the surrounding silicon (Si) was removed from the side of the fluidic-system-wafer. Finally, the outlet hole at the tip was milled by a focussed ion beam (FIB).

2.1.1 Fluidic-system-wafer

The fluidic-system-wafer's flow chart is presented in Fig. 2.1. A 300 nm thick thermal SiO_2 layer was grown on a double side polished 390 µm thick Si wafer. **a)** The cavity for the tip was outlined by reactive ion etching (RIE) into the SiO_2. **b)** The pyramidal pit for the mold of the tip was etched in a potassium hydroxide solution (KOH). A small but significant undercut of the SiO_2 masking due to the KOH etching was expected. **c)** This SiO_2 masking undercut was removed by wet etching half of the SiO_2 thickness (150 nm) in a buffered hydro flouric acid solution (BHF). **d)** The molded tip was formed by low pressure chemical vapor deposition (LPCVD) of 100 nm silicon nitride (Si_3N_4). **e)** The Si_3N_4 layer was limited to only the apex of the tip by RIE from the front side. The Si_3N_4 on the backside was as well removed by RIE and the remaining 150 nm of SiO_2 were removed in a BHF solution. **f)** The KOH

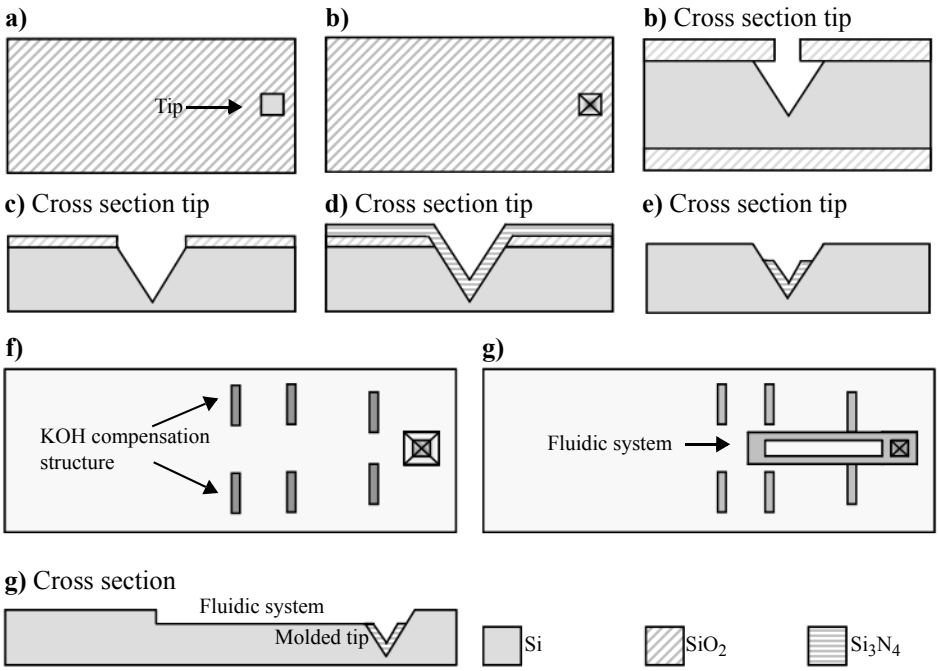

Fig. 2.1 Flow chart fluidic-system-wafer: Starting with a layer of thermal SiO_2 on a double side polished 390 µm thick Si wafer. **a)** The cavity for the tip was outlined by RIE etching into the SiO_2. **b)** The pyramidal pit for the tip was KOH etched. **c)** SiO_2 masking undercut was removed by wet etching in BHF. **d**) LPCVD Si_3N_4 deposition to mold the tip. **e)** Limiting the Si_3N_4 layer to only the apex of the tip by RIE and completely removing remaining SiO_2 with BHF. **f)** The KOH compensation structures were outlined by RIE. **g)** The fluidic system and cantilever were outlined with DRIE.

compensation structures protecting the convex edges of the fluidic system and defining the cantilever were etched by RIE as 300 nm shallow trenches, for further details see section 2.2.4. **g**) As last step, the fluidic system including the cantilever was patterned with deep reactive ion etching (DRIE) as 5 µm deep trenches.

2.1.2 Base-wafer

The base-wafer's flow chart is presented in Fig. 2.2. A 300 nm thick thermal SiO_2 layer and a subsequent 150 nm thick LPCVD Si_3N_4 layer were grown on a double side polished 390 µm thick Si wafer. **a)** The breaking points for later releasing the SIP chip were outlined by RIE into Si_3N_4. **b)** To create a so called shadow mask, a layer of 100 nm Si_3N_4 LPCVD was deposited. This shadow mask has the advantage that, the structure can be opened later in the process, without another photolithography on deeply patterend surface. **c)** The outline and the handling part of the chip, as well as the fluidic connection or reservoirs were outlined by RIE through the Si_3N_4 and SiO_2, stopping on the Si surface. **d)** The cavities for the outline of the chip's handling part and the reservoir were etched in a KOH solution to about 160 µm depth. The breaking points were opened by wet etching the second Si_3N_4 layer of 100 nm in a phosporic acid solution (H_3PO_4). The now open breaking points allowed the KOH to attack the breaking beams. The KOH etching was continued through the complete wafer. Afterwards the breaking beams were preferably very thin and the rectangular convex edges of the chip's handling part were not attacked. **e)** The complete Si_3N_4 and SiO_2 layer were removed by H_3PO_4 wet etch and BHF wet etch, respectively.

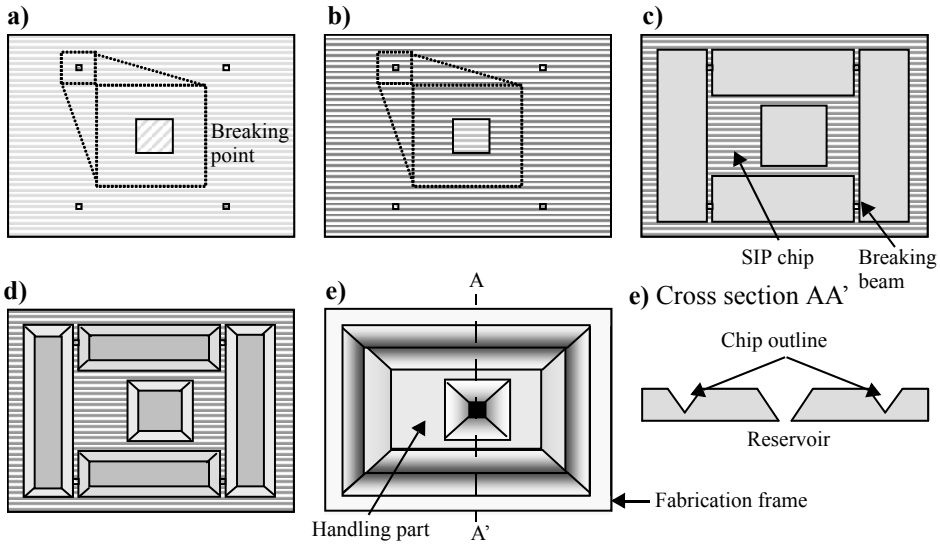

Fig. 2.2 Flow chart base-wafer: Starting with a layer of thermal SiO_2 and subsequent LPCVD Si_3N_4 on a double side polished 390 µm thick Si wafer. **a)** The breaking points were outlined by RIE into Si_3N_4. **b)** To create a shadow mask another Si_3N_4 LPCVD layer was deposited. **c)** The handling part of the chip and the fluidic connection or reservoirs were outlined by RIE through the Si_3N_4 and the SiO_2 layers. **d)** The cavities for the outline of the chip's handling part and the fluidic connection were etched with KOH for about 160 µm. The breaking points were opened by wet etching the second Si_3N_4 layer with H_3PO_4 and continuing the KOH wafer through the complete wafer. **e)** Removing the remaining Si_3N_4 and SiO_2 layer in H_3PO_4 and BHF, respectively.

2.1.3 Bonded wafers

The bonded wafer's flow chart is presented in Fig. 2.3. **a)** The wafers were cleaned and activated in a RCA solution (NH_4OH 27%: H_2O_2 30%: H_2O = 1: 1: 5 at 70° C for 10 min.). For the silicon direct bonding, the wafers were aligned, in such a way, that the trenches of the fluidic system were connected by the reservoir in the base-wafer to the outside. The wafers were pressed together with 0.6 MPa. This wafer sandwich was wet thermally oxidized for a SiO_2 thickness of 1.5 µm. A 500 nm plasma enhanced chemical vapor deposition (PECVD) Si_3N_4 layer was deposited on the fluidic-system-wafer side for a KOH etch mask. The Si_3N_4 and SiO_2 layer were etched with RIE, such that a ring, 1 cm wide, remained at the wafer edge to avoid leaking of the chuck, used in the subsequent KOH step. In addition, a cross through the center was structured, dividing the wafer in quarters to give the wafer more structural stability. **b)** The wafer stack was etched in a KOH solution from the fluidic-system-wafer into the base-wafer. The base-wafer side was protected by placing it into a Teflon chuck. The KOH etching was timed and stopped, once it was optically confirmed that the cantilever was fully released. On selected chips, the outlet hole as the fluidic connection from the fluidic system through the tip to the sample was milled with a FIB. To remove the accumulating charges during FIB milling, a thin gold (Au) layer was deposited up front. This Au layer was, afterwards, removed with a solution of iodine, iodine/potassium to regain the transparency of the fluidic system. To individualize the SIP chips, the wafer was placed on a soft rubber substrate with the base-wafer facing down. Then, the fixation of the SIP chip to the fabrication frame was broken by gently pressing with a tweezer on the handling part of the chip. Finally, the single SIP can be picked up from the rubber substrate. A sketch of the final individualized SIP chip is shown in Fig. 2.3 c).

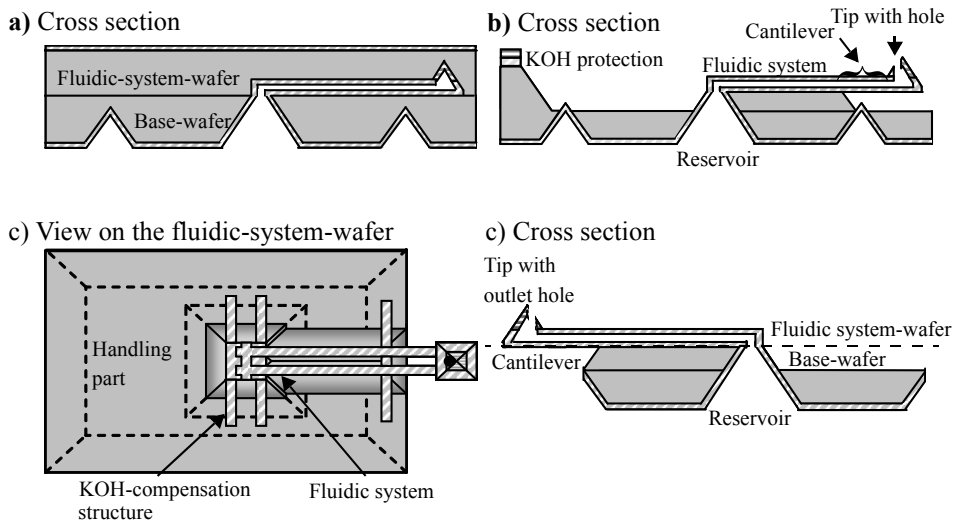

Fig. 2.3 Flow chart bonded wafer **a)** The wafers were cleaned and activated with RCA. For the silicon direct bonding, the wafers were aligned in such a way that the trenches of the fluidic system were connected by the through wafer openings in the base-wafer to the outside. This wafer sandwich was afterwards wet thermally oxidized. A PECVD Si_3N_4 layer was placed on the fluidic-system-wafer side for the KOH etch mask. **b)** The wafer stack was KOH etched from the fluidic-system-wafer into the base-wafer. The etching was stopped once the cantilever was fully released. The base-wafer side was protected by placing it into a Teflon chuck. On selected chips, the fluidic connection from the fluidic system through the tip to the sample was milled with a FIB. c) Sketch of a final individualized SIP chip.

2.2 Design considerations and fabrication results

2.2.1 Overall dimensions

The overall dimensions of the SIP were designed as such that it could be mounted on a commercially available SFM without any major modifications on the clamping system. Fig. 2.4 a) shows a scanning electron microscope (SEM) image of the base-wafer side of the SIP. The maximum SIP dimensions were measured to be 1.5 mm × 3.5 mm (width and length) with the positively inclined sidewalls from the KOH etching and these dimensions were close to the commercial available SFM chips. The SIP chips were successfully mounted and used on a SFM from Veeco[1] and JPK Instruments[2] without any modifications. In our group we use a SFM from Nanosurf[3], which requires the integration of alignment features. The integration seems to be technically possible and they could be fabricated in the KOH etching step **d)** and **e)** of the base-wafer fabrication, see image Fig. 2.2. In image Fig. 2.4 a), the SIP's fluidic connection to the holder of SFM or the reservoir can be seen. The fluidic connection was shaped during the KOH etching as an inverted truncated pyramid with a height of 390 µm and square shaped base plate with a width of 580 µm. In order to have a short fluidic connection to the tip, it was placed at a distance of 30 µm to the front edge of the SIP chip. A detailed description of the fluidic interfacing between a Veeco SFM and the SIP is given in chapter 7. Fig. 2.4 b) shows a SEM image of the SIP from the fluidic-system-wafer side. It can be seen

1. Veeco, NanoScope and Nano IV
2. JPK Instruments, Nanowizard
3. Nanosurf, Nanite

a) Base-wafer side b) Fluidic-system-wafer side

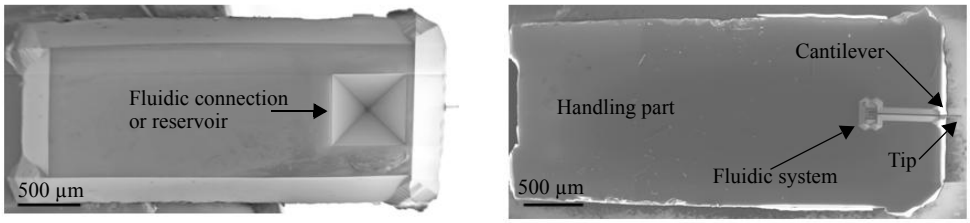

Fig. 2.4 SEM image of a fully fabricated and individualized SIP. a) From the base-wafer side, showing the fluidic connection or the reservoir. b) From the fluidic-system-wafer side showing the fluidic system, the cantilever and the tip.

that the space used for the fluidic system was rather small compared to the large non structured handling part of the chip. This offers the opportunity to integrate additional fluidic elements, like additional reservoirs, pumps or sensors. Finally, the fluidic system was elevated from the handling part due KOH etching release of the cantilever. Its elevation was measured with a white light interferometer to be 80 µm.

2.2.2 Cantilever and tip

In order to reasonably image a delicate biological sample in liquid, the SIP should have a cantilever with a low stiffness, preferably in the range of 0.01 - 0.1 $N \cdot m^{-1}$ [54]. From the SEM image shown in Fig. 2.5 a) the length of the cantilever was measured to be 155 µm. Its transition from the fluidic system and its clamping was well defined by the KOH compensation structures. In order to calculate the second moment of area I_z required to calculate the cantilever stiffness k, an image of the cross section was taken as shown in Fig. 2.5 b). One capillary of the cantilever was cleaved at its transition point to the fluidic system. The interior cross section was measured to be 3.7 µm × 2.2 µm, while the SiO_2 sidewall thickness of the protected bottom was measured to be 1.5 µm and the top, which was exposed to the KOH etching, was measured to be 1.2 µm. This resulted in a calculated cantilever stiffness of $k = 6.5\ N \cdot m^{-1}$ according to Eq. (1.19) with a Young's modulus Y of thermally grown SiO_2 of 87 GPa [55]. In order to decrease the cantilever stiffness its length should be extended but also the SiO_2 sidewall thickness should be decreased during thermal oxidation. Nevertheless, scanning force microscopy experiments showed that the stiffness is low enough for imaging even in contact mode. Finally, the dynamic behavior of the cantilever was measured[1]. It revealed a resonance frequency of 159 kHz and a quality factor of 186, which makes the SIP also suitable for scanning force microscopy imaging in tapping mode.

In order to achieve high resolution in scanning force microscopy imaging and printing a sharp tip with an apex radius of curvature in the range of 10 nm is required [56]. Fig. 2.5 c) shows the tip at the end of the cantilever from the side. The tip height was measured to be 2.4 µm. The molding of the Si_3N_4 tip into the SiO_2 of the cantilever can be seen. In the final fabrication step, the KOH release, the SiO_2 got slightly attacked and remained smoothened, whereas the Si_3N_4 tip was not etched and remained sharp. In a more detailed view of a tip, as shown in Fig. 2.5 d), the tip radius was measured to be around 40 nm. Furthermore, the outlet hole in the tip can be seen, its radius was measured to be 50 nm. Placing the hole in the very close vicinity of the apex, allowed to maintain the sharp tip for high scanning force

1. JPK Instruments, Nanowizard

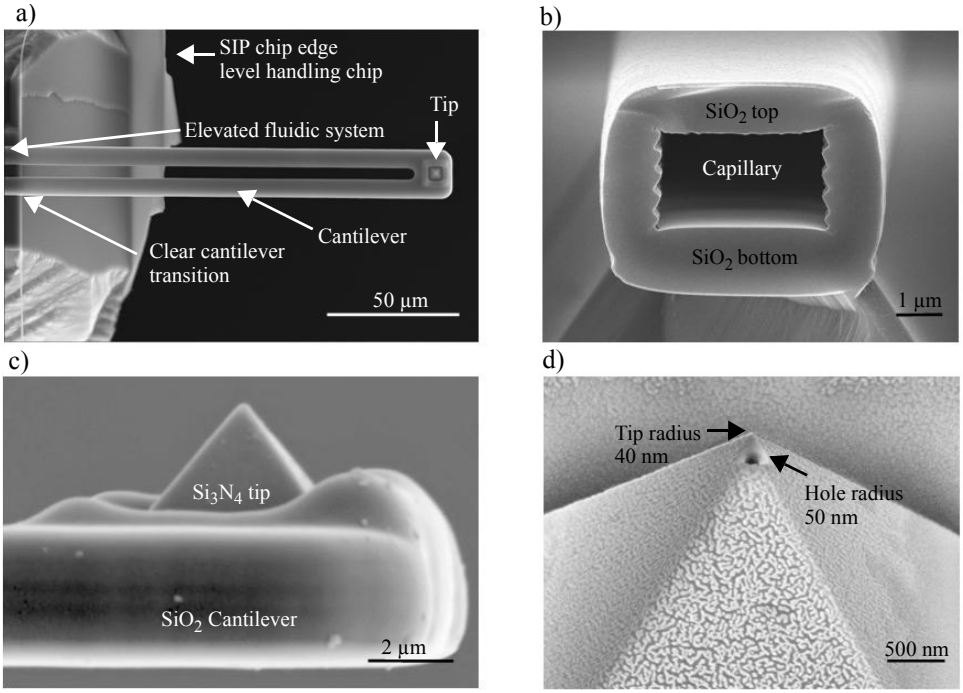

Fig. 2.5 SEM image of: a) a clamped 155 µm long SiO_2 cantilever. b) The cross section of a cleaved cantilever. The interior cross section was measured to be 3.7 µm × 2.2 µm. c) The molded 2.4 µm high Si_3N_4 tip and d) a closer view of the tip, showing the tip 40 nm radius and the FIB milled hole with a radius of 50 nm. The surface texture on the tip was of a 10 nm thick gold layer to improve the resolution during SEM and FIB milling.

microscopy imaging resolution and to be in close proximity for highly localized dispensing. For dispensing, the SIP should be operated immersed in water. The dispensing rate should be in the range of 0.1 $pl \cdot s^{-1}$, which is equivalent to an average liquid velocity of 12.7 $mm \cdot s^{-1}$ within the outlet hole of 50 nm radius. Since the hydraulic resistance of the hole in the tip dominated the hydraulic resistance of the SIP, a calculated applied pressure of 4 kPa was necessary to achieve the desired dispensing rate, see Eq. 1.3.

2.2.3 Fluidic system

The fabrication process allowed a very flexible layout of the fluidic system, hence, a complex network of capillaries could be designed. No geometric restrictions for the design concerning the maximum capillary length could be determined. The maximum length of the fluidic system was defined by the longest path from the reservoir to the tip. The innovation of the SIP fabrication by Hug et al. [53] allowed the fabrication of reasonable fluidic system lengths in the range of millimeters, and sufficiently thick SiO_2 sidewalls in the range of 1 µm. This can be reasoned by the Deal and Grove [57] model for SiO_2 growth during wet thermal oxidation. In their model, it was assumed that after already a few minutes, the SiO_2 growth was limited by diffusion of oxidizing species through an increasing thickness of SiO_2 to the Si/SiO_2 interface and not by capillary length dependent gas phase diffusion. The capillary width was considered as a critical parameter. It was expected that stress induced cracks may introduce leaks into the capillary. This stress originated in the mismatch of expansion coefficients between Si (2.6×10^{-6} [58]) and SiO_2 (5×10^{-7} [58]). This was especially

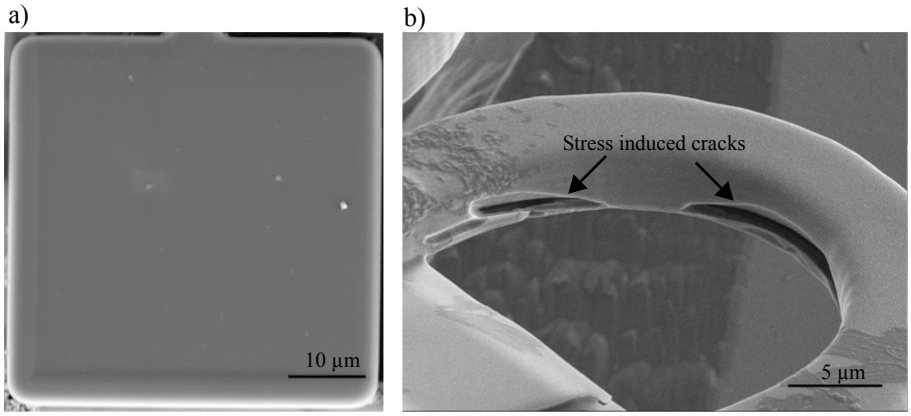

Fig. 2.6 SEM image of: a) a stable 50 µm wide square shaped membrane. b) A small radius of curvature in the fluidic system's capillaries yielded a high stress and induced cracks into the capillary sidewall.

enhanced during the cooling after the oxidation from 1100° C down to 23° C. Nevertheless, after the fabrication, this cracking problem was not observed, since squared membranes with widths up to 50 µm were produced without any cracks, as shown in Fig. 2.6 a). But unexpectedly, stress induced cracks were observed on the inside of curvatures with a small radius, as shown in Fig. 2.6 b). The radius of curvature was in this case 12 µm. It seemed that considerable amount of stress accumulated in the inside of the curvature, so that the SiO_2 sidewall cracked.

Another important aspect in the design and fabrication of capillaries, with such a small cross section (below 10 µm), were surface contaminations. They resulted in considerable contamination of the minute amounts of liquids within the capillaries of the fluidic system. In this fabrication process, the capillaries of the SIP were fabricated by thermal oxidation at 1100° C and this resulted in a very pure and clean SiO_2 capillary surface, which was in addition highly chemically inert. Even though, this contamination sensitivity became even more important for chemical solutions, for instance in case of the electroless silver deposition, described in chapter 5.

2.2.4 Specific design for anisotropic KOH etching

The fabrication of KOH exposed convex corners of the chip outline and of the fluidic system required special design features, so called KOH compensation structures, to compensate for the different crystallographic KOH etch rates [59]. The first KOH compensation structures were employed during the base-wafer fabrication. They were included into the breaking beams. These beams had to protect the convex rectangular SIP chip corners during KOH etching and they had to fix the SIP to the fabrication frame of the wafer during fabrication. After the fabrication, these beams were broken to seperate the SIP from the wafer. Hence, it was important that the beams were weak enough to reliably break, before the chip breaks, preferably along its weak crystal planes. A thinning of the breaking beams was achieved by opening the breaking points in step **e)** of the base-wafer fabrication, see Fig. 2.2. The etch depth ratio of the KOH etch before and after opening the breaking points had to be carefully chosen, so that the breaking beams were thin enough and that rectangular SIP chip corners were just not attacked. Fig. 2.7 a) and b) shows a SEM image of an appropriate thin breaking beam and a protected SIP chip corner.

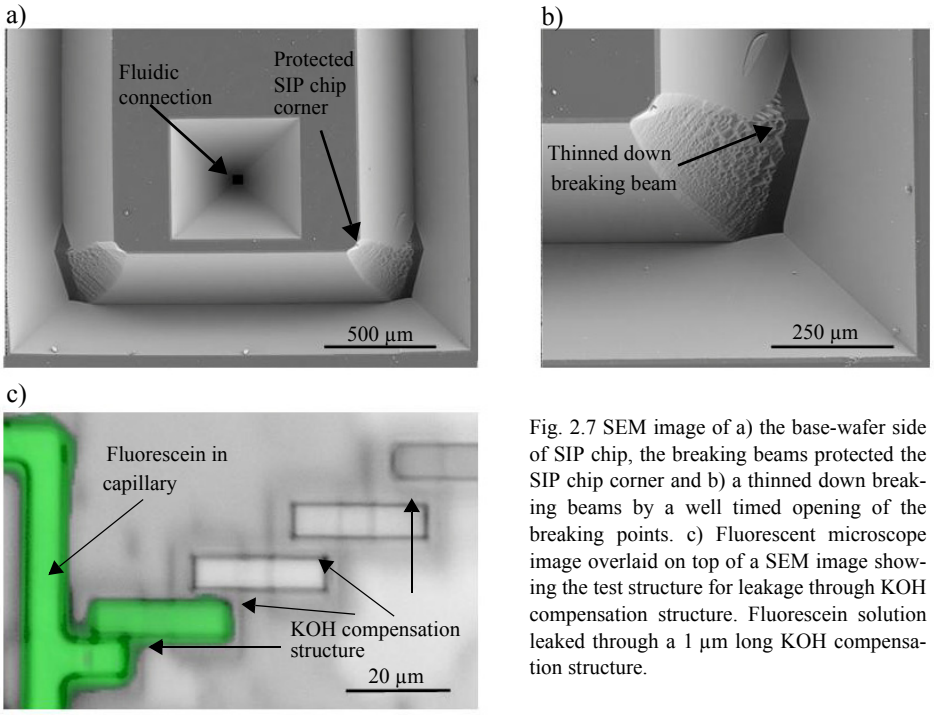

Fig. 2.7 SEM image of a) the base-wafer side of SIP chip, the breaking beams protected the SIP chip corner and b) a thinned down breaking beams by a well timed opening of the breaking points. c) Fluorescent microscope image overlaid on top of a SEM image showing the test structure for leakage through KOH compensation structure. Fluorescein solution leaked through a 1 µm long KOH compensation structure.

During the release of the cantilever, the final KOH etching, the convex corners of the fluidic system needed to be protected. Special care in the design needed to be taken for the length and thickness of the KOH compensation structures. The length had to compensate for the slightly different KOH etch rates over the wafer. In the used etch-bath, the experienced etch rate differences were less than 5%. The main reason for etch rate differences was a non homogeneous temperature distribution within the KOH etch bath. The KOH etching was stopped once all cantilevers on the wafer were released, hence, a KOH compensation structure length of 75 µm longer (150%) than the cantilever was considered to be sufficient. KOH not only etches Si but also attacks the SiO_2 of the KOH compensation structure (typical etch rate selectivity Si/SiO_2 in the range of 1/200) [59]. The SiO_2 thickness of the KOH compensation structure was determined by DRIE etching a trench and subsequent oxidation. A too shallow trench for the KOH compensation structure would result in an insufficiently thick compensation structure, which then would be completely etched away before the end of the KOH etching. A too deep trench would not be reliably closed during the thermal oxidation and a leakage through the KOH compensation structure would occur. This can be avoided with the correct ratio between depth to SiO_2 thickness ratio. Knowing that 55% of the SiO sidewall was grown out of the initial Si interface [58], the trench could be completely closed and fluidically sealed. From experiments, the RIE trench depth for the KOH compensation structure was chosen to be 0.3 µm, resulting in a calculated SiO_2 thickness of 0.55 µm [58]. This thickness was sufficient to withstand the KOH etching and this trench depth was shallow enough to be reliably closed during oxidation. An experiment verifying the complete oxidation of the KOH compensation structure is shown in Fig. 2.7 c). In detail, capillaries with an increasing spacing were connected with KOH compensation structures to the fluidic

system. The spacing varied from a minimum of 1 µm and increased by steps of 1 µm. It can be seen that fluorescein solution could only be detected in the first capillary, hence, the KOH compensation structure was reliably closed after 1 µm.

2.2.5 Remarks on silicon direct bonding

Most of the failed wafers broke after the thermal oxidation due to faulty bonding. It turned out, that for a successful bonding, the bonding interfaces needed to be the cleanest possible and with the least etched structures necessary. Next to that, the cleaning and activation step with RCA, right before the silicon direct bonding, was crucial. Especially, after the silicon direct bonding, a major risk was imposed by non bonded areas in contact with the fluidic system. These voids resulted in comparably large patches of SiO_2 at the interface during the subsequent thermal oxidation. The wafers probably broke because of stress induced by the mismatch of thermal expansion coefficients between these SiO_2 patches, compared to the bulk Si, considering also the temperature step at the end of the thermal oxidation step. An infrared microscope image, like the one presented in Fig. 2.8, reveals those non bonded areas and according to their size and distribution a continuation in processing can be decided. The image presented in Fig. 2.8 was taken close to the breaking edge. The observed Newton's fringes were a good indicator of a faulty bonding and of stress concentrations.

2.3 Laboratories involved

The process for the SIP fabrication was first developed in Comlab, the joint IMT-CSEM cleanroom facility in Neuchatel, Switzerland. I had the pleasure to fabricate the first devices presented here in this thesis under the supervision of T. Akiyama. The second generation was fabricated at the DIMES facilities in Delft, Netherlands. For the transfer of the process flow to the equipment and the established processes within DIMES, I worked close together with P.M. Sarro. During the fabrication, I was supported by J. Slabbekoorn. The hole in the tip was milled with a FIB at the faculty of TNW with the help of H. Miro and P. Alkemade.

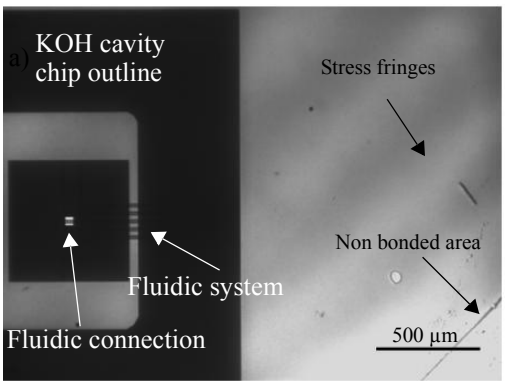

Fig. 2.8 Infrared microscope image of stress fringes and non bonded areas at the interface between the two wafers. This image was taken after the thermal oxidation. Image taken in transmission mode, with observation from the fluidic-system-wafer.

2.4 Conclusions and outlook

In summary, a successful fabrication of a scanning ion pipette was shown. The fabrication uses only well established microfabrication processes. This process allowed a very versatile layout of capillaries without any major geometric constrains forming a complex fluidic system. The fabricated SiO_2 capillaries were hydrophilic and transparent. This resulted in a self filling of the capillaries which could be optically observed. In addition, freestanding cantilevers and molded Si_3N_4 tips can be included into the system forming the SIP. Nevertheless, the integration of metals as possibly electrodes into the capillary is complicated due to the high oxidation temperatures. Hence, the deposition of metal layers is preferably done after the fabrication. Finally, for future fabrication, the sides of the capillaries can be buried in Si such that only the top is visible, by integrating the KOH compensation structures into the base-wafer. This would give the system more mechanical stability, may avoid leakage due to the small radius of curvature and it clamps the cantilever from three sides which should increase the resonance quality factor.

Chapter 3

Evaporation induced pumping within the scanning ion pipette

Evaporation induced pumping represents a straightforward implementation of a micropump into the scanning ion pipette (SIP). The working principle of an evaporation based micropump is as follows: The hydrophilic capillaries of the SIP are filled instantaneously with a water based solution. Once the fluid reaches the capillary outlet, it starts evaporating. The capillary pressure keeps the outlet of the capillaries wetted, and thereby, replaces autonomously the evaporation loss by drawing additional water through the capillaries. This results in an unidirectional pump, which for instance can be used to suck in liquids through the tip‘s hole and concentrate them inside the outlet of the capillaries. The implementation of such a pump does not require any additional fabrication steps of the SIP. Only the geometry of the capillary outlet area needs to be increased to enhance the evaporation induced pumping. In this chapter, the pumping effect is modelled and verified with experiments. Evaluating the evaporation pump was one of the first experiments. It helped to develop a feeling and understanding of the challenges imposed by the dimensions of the SIP capillaries, with a cross section of less than 10 μm^2.

Evaporation based pumps in microfluidic systems caught considerable attention in recent years, especially due to their simple integration into the fabrication process and their considerably high pumping pressure, up to the capillary pressure. One of the first reported evaporation based pumps in a microfluidic system was presented by Namasivayama et al. [60]. Their evaporation pump consisted of a hydrophobic patch stopping the capillary filling of the microfluidic system, thus creating a well defined water-air interface. The hydrophobic patch ended in the center of a T-junction. This enabled two ways of controlling the evaporation induced flow by either adjusting the temperature at the hydrophobic patch or the airflow through the straight channel of the T-junction. In their case a stable flow of 10 $pl \cdot s^{-1}$ was achieved, for a capillary cross section of typically 50 µm × 600 µm. A very active field of exploring applications for microfluidic systems is lab-on-a-chip. Here, the small footprint of the evaporation pumps is considered advantageous [61]. Zimmermann et al. [62] controlled the flow by actively adjusting the temperature at the evaporation pump. For their microfluidic system consisting of capillaries with a square cross section of 30 µm × 30 µm flow rates from 10 $pl \cdot s^{-1}$ up to 1.2 $nl \cdot s^{-1}$ were achieved. Walker et al. [63] extended the pumping mechanism to also concentrate a flow of bovine serum albumin solution. Finally, evaporation based micropumps were successfully used in chromatographic applications to drag solutions through long capillaries with very small cross sections. The evaporation based micropump provided sufficient pressure to have a reasonable throughput and separation [64].

3.1 Theory of evaporation induced pumping in microcapillaries

The following section briefly introduces the theoretical background of the pumping mechanism. A more detailed description can be found in Namasivayam et al. [60]. For illustration, a sketch of the SIP with an evaporation pump is shown in Fig. 3.1 a). The working principle is as follows: A droplet of water is placed into the reservoir which fills immediately the hydrophilic fluidic system and starts to evaporate inside the evaporation cell. In the evaporation cell the capillary pressure keeps the entrance of the microcapillaries into the evaporation area wetted and thereby, replaces the evaporation loss by drawing water through the fluidic system. To increase the evaporation induced flow, the evaporation area can be further increased by spreading the microcapillaries out into a manifold of top open capillaries. This increases the flow rate but inherently also the flow induced pressure drop over the hydraulic resistance of the fluidic system. This results in two different flow regimes: In the low flow regime, the pressure drop over the fluidic system p_{sys} is lower than the capillary pressure p_c, all open ended capillaries are kept wet and the flow rate Q is limited by the evaporation rate (shown in Fig. 3.1 b) top). In the high flow regime, a maximum evaporation induced flow rate is reached, the pressure drop p_{sys} over the fluidic system equals the capillary pressure p_c. In this case the hydraulic resistance $R_{hy,sys}$ of the fluidic system and the capillary pressure p_c limit the flow rate Q. The capillary pressure p_c can no longer keep the full surface of the evaporation area wetted, hence, not all top capillaries are wetted. The evaporation rate is self limiting by reducing the evaporation area, as shown in Fig. 3.1 b) bottom.

In further, a quantitative model for the low flow regime, anticipated in this chapter, is developed. Water evaporates in the evaporation cell and diffuses through the opening into the surrounding laboratory environment. Thus a gradient of partial water vapor pressure $\partial p_v / \partial x$ establishes inside the evaporation cell, which drives the evaporated water vapor out. Fick's 1st law describes the diffusion of water vapor within the evaporation cell and hence, defines the evaporation rate N_E per area as:

$$N_E = \frac{D}{N_A k_B T} \frac{\partial p_v}{\partial x}, \tag{3.1}$$

where D, k_B, N_A and T denote the water vapor diffusion constant, the Boltzmann constant, the Avogadro constant and the temperature in the evaporation cell, respectively [65]. The x-coordinate is defined as being normal to the evaporation cell bottom plane.

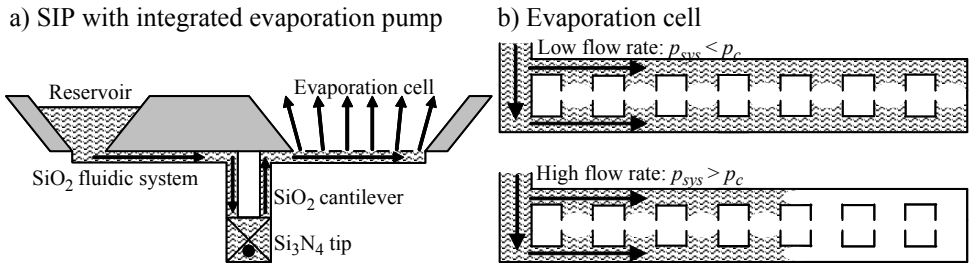

Fig. 3.1 a) Sketch of a SIP with an integrated micropump. Evaporating water induces suction flow inside the SFM-chip. b) Different filling levels of the evaporation cell depending on flow induced pressure drop over the fluidic system p_{sys} and capillary pressure p_c at the water-air interface inside the evaporation cell.

Due to conservation of water, the diffusion flow rate of water vapor inside the evaporation cell equals the pump rate Q inside the capillary. To obtain the pump rate Q, the evaporation rate N_E, which represents a molar flow density, needs to be further transformed into a molar flow by the area of evaporation A_E. In addition, the partial water vapor pressure p_v at the water-air interface in the evaporation cell's bottom ($x = 0$) is given by saturated water vapor pressure p_{vsat}. Finally, the molar flow is transformed into a volume flow by the molecular weight of water vapor M [0.018 kg·mol^{-1}] and the liquid density ρ_l:

$$Q = \frac{M}{\rho_l} A_E N_E = \frac{M}{\rho_l} \frac{D}{N_A k_B T} A_E \left. \frac{\partial p_v}{\partial x} \right|_{x=0} . \tag{3.2}$$

For the investigation of the micropump, it is beneficial to separate the pump rate Q into a geometry independent Q_{NG} and a geometry dependent Q_G parameter. The molecular weight M, the liquid density ρ_l, the diffusion constant D are clearly not geometry dependent, whereas the area of evaporation A_E depends on the geometry. So far, the partial water vapor pressure gradient $\partial p_v / \partial x$ was not allocated, according to its geometry dependency. It is assumed, that at the water-air interface the water vapor pressure is saturated and that it decays to the relative humidity in the lab. This decay is influenced by the geometry of the evaporation cell. For a first approximation, the partial water vapor pressure gradient $\partial p_v / \partial x|_{x=0} = p_{vsat}\, dp_{x0}$ is split into two terms: geometry independent saturated water vapor pressure p_{vsat} at the water-air interface and the geometry dependent water vapor pressure gradient dp_{x0}. This leads to the description of the pump rate Q as:

$$Q = Q_{NG}\, Q_G , \tag{3.3}$$

where

$$Q_{NG} = \frac{M}{\rho_l} \frac{D}{N_A k_B T}\, p_{vsat} \text{ and } Q_G = A_E dp_{x0} . \tag{3.4}$$

A further look reveals, that the geometry independent factors Q_{NG} are also the only temperature T dependent ones; The temperature has a minor influence on the liquid density ρ_l [66]. Gates et al. [67] reported a linear dependency of the diffusion constant D of water vapor on the temperature T. The temperature T dependency of the saturated water vapor pressure p_{vsat} can be described by the Clausius-Clapeyron-equation although numerical values found in the work from Weast et al. [66] were used for a more accurate modelling. Finally, in case of the geometric depending factor Q_G the area of evaporation A_E stayed temperature T independent, since the experiments were performed in the low flow regime.

3.2 Experimental

As the temperature is the most convenient control parameter of the pump rate, a therefore, suitable SIP chip and measurement setup was designed.

3.2.1 Design of the scanning ion pipette with an integrated evaporation based pump

The evaporation based pump integrated into the SIP was designed to operate in the low flow regime, where the capillary pressure p_c dominates the pressure drop p_{sys} over the fluidic system. The fluidic system consisted of two capillaries in parallel to reduce the hydraulic

resistance. Each capillary had a cross section of 2.25 µm × 3.75 µm (height × width) and a length of 2.1 mm between the inlet and the reservoir. The hydraulic resistance was calculated to be $R_{hy,sys} = 4.7 \times 10^{17}$ Pa·s·m^{-3}, according to Eq. (1.4). These capillaries were connected to the evaporation cell, which ended in a manifold of 48 top-open capillaries. In there, the capillary pressure at the exit to the top-open part was calculated to be $p_c = 65$ kPa, employing Eq. (1.8). This resulted in a theoretical, maximum flow of $Q_{max} = 130$ pl·s^{-1} for the low flow regime. The geometry of the evaporation cell had the shape of an inverted truncated pyramid with a bottom plane of 30 µm × 480 µm and a height of 390 µm. The side walls were inclined with the KOH specific angle of 54.7°. Finally, the SIP fabricated chips needed to be modified with a polydimethylsiloxane (PDMS) gasket of cylindrical shape on top of the inlet reservoir, diameter 1 mm height 3 mm in order to increase the measurement time and minimize particle concentration changes.

3.2.2 Instrumentation and method

In the setup for the flow measurement, the SIP chip was mounted on a 3 mm thick resistively heated aluminium plate. The heat transfer to the SIP chip was improved by using a heat sink compound[1]. The temperature was measured with a k-type thermocouple at the close vicinity of the chip. It was then mounted on an inverted fluorescence microscope[2] with integrated filter sets. The experiment was observed by monitoring the evaporation cell with a cooled CCD camera[3]. The magnification was set such that one pixel corresponded to 0.4 µm. The whole chip setup was covered with a non transparent box to eliminate airflow and illumination from the outside.

For the pump rate Q determination the accumulation of fluorescent labelled microspheres[4] inside the evaporation cell was observed, hence, microspheres with a diameter of 0.2 µm were chosen. This diameter was less than 10% of the fluidic system's smallest dimension, which avoided the interference of the microspheres with the capillary. A low microsphere concentration of 5.7×10^{12} #·m^{-3} was chosen to minimize the risk of clustering and of a diffusion driven flow of microspheres in the opposite direction of the water flow. The solution of microspheres was freshly prepared for each experiment by degassing water at a temperature of 90° C for 10 min. After cooling, the microspheres were added to the solution and it was sonicated for 15 min. to split possible microsphere clusters and to obtain a homogeneous distribution.

On the instrumentation side the small dimension and, therefore, the low fluorescent light intensity of the microspheres challenged the measurement of the pump rate Q. The usual way of measuring the microsphere velocities in the capillary was no longer possible due to their low light intensity and high flow speed. Therefore, an alternative approach was chosen. Each microsphere represented a water volume defined by the concentration. The pump rate Q could then be deduced from the accumulation of microspheres in the evaporation cell, which in contrast to the water could not evaporate. The accumulation of microspheres was observed by the CCD camera taking an image every 15 s. The detection of individual microspheres was improved by adjusting the brightness and the contrast of camera to obtain an optimal dispersion in the high grey scale values. This series of images was imported into *Matlab* to count the accumulation of microspheres. The counting algorithm proceeded as

1. Dow Corning, DC340
2. Carl Zeiss, Axiovert S100
3. Kappa, CF 8/4DXC
4. Polyscience, Flouresbrite YG carboxylate microspheres

follows: First, spots containing clusters or individual microspheres were detected by discarding the background information of the evaporation cell. In detail, the grey scale value of the pixel was compared to the average of its surrounding. It was kept in case it differed to the average by a certain threshold, otherwise it was set to zero. Then, individual microspheres in the spots were identified by further transforming the image into a gradient one. This enabled to count the local gradient grey scale maxima in the spots, representing the microspheres.

3.3 Results and discussion

3.3.1 Verification of the measurement method

For the determination of the pump rate Q individual microspheres inside the evaporation cell needed to be identified and counted. A typical 8-bit greyscale image obtained by the CCD camera from the bottom of the evaporation cell is shown in Fig. 3.2 a). The first filtering algorithm with a threshold value of 35 on a square of ten by ten pixels successfully deleted the background information and extracted spots containing microspheres, as shown in Fig. 3.2 b). It could be seen that the size and the intensity of the spots vary. It needed to be assumed that these spots contain clusters of microspheres. The identification of individual microspheres was not straight forward since the pixel resolution of the camera (0.4 µm) was larger than the diameter of an individual microsphere (0.2 µm). Also the microspheres had a depth dispersion within the evaporation cell, exceeding the microscopes depth of focus. Individual microspheres could only be identified in the gradient image. This is exemplarily shown on one of the spots from Fig. 3.2 b) transformed into to a gradient image shown in Fig. 3.2 c). This spot in the gradient image contained two local minima, representing two microspheres.

This algorithm was verified by conducting an experiment with constant temperature, T = 296 K, and constant relative humidity (33%) at the outlet of the evaporation cell. In case the algorithm worked properly, it would detect a constant accumulation of microspheres. Fig. 3.2 d) shows the microspheres counted by the algorithm. Linear fitting was in good agreement with the data and revealed a slope of 0.064 #·s^{-1}, which equalled a pump rate of 11 pl·s^{-1}. Towards the end of the experiment, the noise increased since more and more clusters containing several microspheres appeared rather than spots with single microspheres.

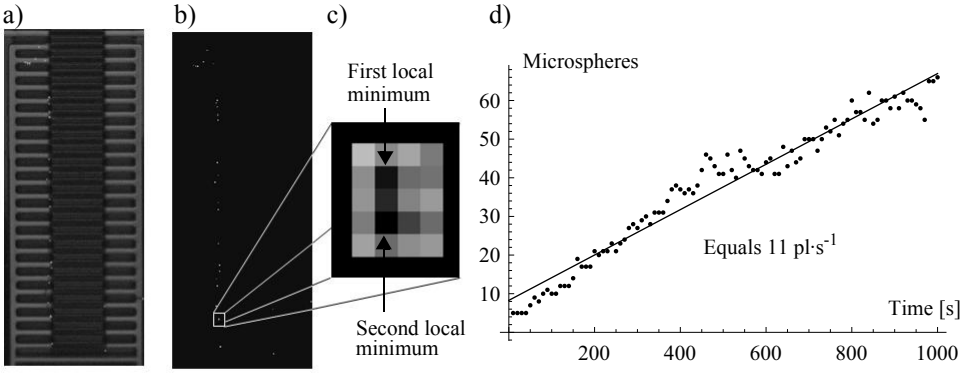

Fig. 3.2 a) Optical microscope image bottom evaporation cell including clusters microspheres (white spots). b) Filtered image to remove the background information. c) Detailed view of a cluster of microspheres. Image is further transformed into a gradient image. d) Accumulation of microspheres at constant evaporation conditions.

3.3.2 Deduction of the model parameters

For the modelling of the geometry independent part Q_{NG} of the pump rate Q reliable values were found in literature, Weast et al. [66] and Gates [67]. They can be well fitted in the investigated temperature range from 296 K to 338 K by:

$$Q_{NG} = \frac{M}{\rho_l N_A k_B T} \frac{D}{T} p_{vsat} = (a + bT) \exp\left[-\frac{\Delta H_{vap}}{N_A k_B} \frac{1}{T}\right], \tag{3.5}$$

where a and b were fit parameters and the water evaporation enthalpy $H_{vap} = 45.1$ kJ·mol^{-1}. Based on these literature values the fit parameters were concluded to $a = 6.49 \times 10^{-2}$ m^2·s^{-1} with $\pm 8.2 \times 10^{-4}$ m^2·s^{-1} (1σ) and $b = -4.45 \times 10^{-5}$ m^2·s^{-1}·K^{-1} with $\pm 2.3 \times 10^{-6}$ m^2·s^{-1} (1σ).

The geometry dependent parameters Q_G were more challenging to assess and only an estimation can be provided. The experimental area of evaporation A_E can be estimated from Fig. 3.2 a). The microspheres were not homogeneously dispersed on the bottom of the evaporation cell, they were aligned at the capillaries entrance into the evaporation cell. The capillary pressure p_c of the top-open capillary was not sufficient to dominate the pressure drop p_{sys} over the fluidic system. For the modelling, the area of evaporation A_E was, therefore, reduced to the cross section of the capillaries. In further, any curvature of the water-air interface by the contact angle between the liquid and the silicon dioxide surface was neglected, as well as bending by corner flow in the two bottom corners. In addition, the amount of active capillaries was reduced to 29 since the second row of the evaporation cell was not completely wetted, presumably due to a contamination. The amount of active capillaries did not vary throughout the experiment, indicating the low flow regime.

The geometry dependent water vapor pressure gradient dp_{x0} had to take the special geometry from the fabrication process into account. A sketch of the geometry of the evaporation cell, as well as, the entrance of the capillaries as top-open trenches at the evaporation cells bottom is shown Fig. 3.3 a). Due to the KOH etching, the shape of the evaporation cell had the typical shape of an inverted, truncated pyramid. In addition, the capillaries enter the bottom of the evaporation cell as top-open trenches. This represented a

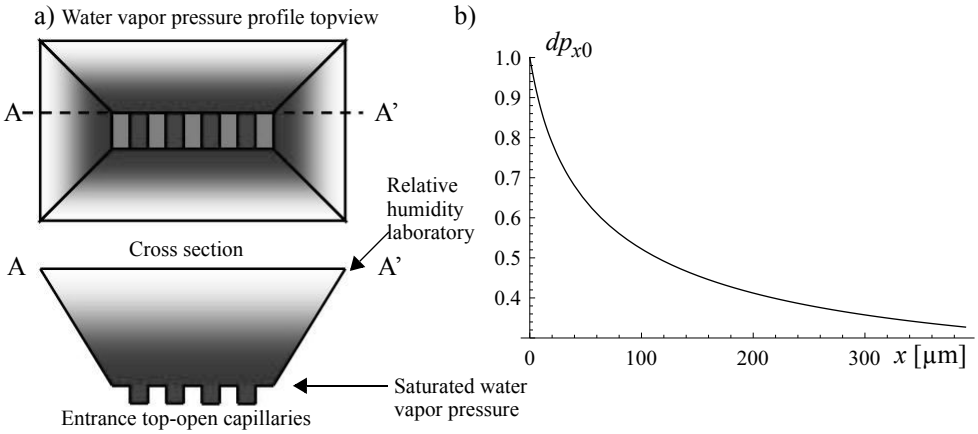

Fig. 3.3 a) Evaporation of water in inverted truncated pyramid shaped evaporation cell. b) Modelled water vapor pressure profile inside the evaporation cell.

complex geometry, which imposed a lot of challenges for an accurate modelling. To get a good first approximation of the water vapor profile, the model was reduced to take only the widening of the KOH inverted truncated pyramid and the flux along the x-axis into account. The boundary conditions for the numerical model were: saturated water vapor pressure p_{vsat} at the bottom of the evaporation cell, and a 33% relative humidity from the laboratory environment at the exit of the evaporation cell. The modelled water vapor pressure profile is shown in Fig. 3.3 b). The gradient at the water-air interface was steeper than in reality, since not the complete bottom of the evaporation cell was wetted, hence, the water vapor pressure was lower than saturated water vapor pressure. This led to the following geometry dependent part of equation (3.3): $Q_G = A_E\, dp_{x0}$,with $A_E = 2.15 \times 10^{-10}$ m^2 and a gradient of water vapor pressure $dp_{x0} = 160$ m^{-1} at the bottom of the evaporation cell $x = x_0$.

3.3.3 Temperature dependent pump rate

Finally, the influence of the temperature T on the pump rate Q was investigated by changing the temperature at the water-air interface. For this, the sample holder was resistively heated and the temperature was recorded in parallel with CCD images of fluorescent microspheres in the evaporation cell. The pumped water volume according to the accumulation of microspheres, represented by open circles (o), is shown in Fig. 3.4 a). The non linearity in the graph was due to an increasing temperature throughout the experiment, causing an increasing pump rate Q. The model (dots) was fitted to the data with a standard deviation of 0.4 nl. The model predicted well the temperature T dependency of the pump rate Q_{NG}. However, the geometry dependency of the pump rate Q_G needed to be corrected by a factor of 3.133, indicating that the area of evaporation A_E was larger than assumed in the model. From this fit the pump rate Q depending on the temperature T can be deduced and it is displayed in Fig. 3.4 b). With the current setup a pump rate Q = (0.74 ml·s^{-1} - 0.51 µl·s^{-1}·K^{-1}·T) exp[-45.1 kJ·mol^{-1}/($N_A\, k_B\, T$)] ranging from 7 pl·s^{-1} at 23° C up to 53 pl·s^{-1} at 65° C could be achieved.

3.4 Conclusions and outlook

In summary, a successful integration of an evaporation driven micropump into the SIP was shown. A model for predicting the pump rate induced by the evaporation pump was presented. The implemented micropump was characterized by a temperature dependent pump rate Q of 7 pl·s^{-1} at 23° C, increasing up to 53 pl·s^{-1} at 65° C. The accuracy of the model

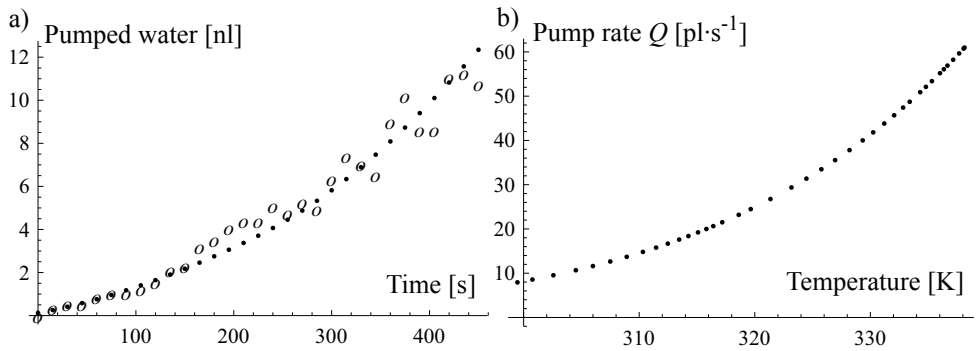

Fig. 3.4 a) Pumped water with an increasing pump rate by increasing the temperature (experimental data, open circles o; fitted model, dots). b) Dependency of the pump rate Q on the temperature T.

mainly depended on the complex structure of the evaporation cell. These shortcomings should be overcome by a new design, taking the incomplete filling of the top-open capillaries and the inverted truncated pyramid shaped evaporation cell into account. An evaporation pump integrated into the SIP can be potentially used for sucking liquids through a hole in the tip. The applied suction pressure depends on the pressure drop induced by the evaporation flow over the resistance of the hydraulic system. For future applications of the evaporation pump, a robust, i.e. more or less evaporation independent, pump can be designed by enlarging the evaporation area so that the pressure drop over the fluidic system is higher than the capillary pressure. In this case, the flow rate is defined by the hydraulic resistance of the fluidic system. A possible application is electroplating inside closed microfluidic capillaries. The main purpose of the evaporation pump is to keep the concentration of the plating solution over electrodes constant during the deposition time, regardless of the increasing plating solution concentration inside the evaporation pump. This application is shown for electro plating of silver in the next chapter.

Chapter 4

Electroosmotic pumping with Pt electrodes

In order to achieve bidirectional active pumping, the scanning ion pipette (SIP) is extended with an electroosmotic (EO) pump. A key challenge of the design of EO pumps is the coupling of the electrical current into the ionic solution, which is commonly done with electrodes made out of platinum (Pt). However, in that case, the electron transfer is linked to electrolyzing the solution and gases are formed. These gases emerge as bubbles and may block the conductive liquid-path between the electrodes and, hence, inhibit a further actuation of the pump. Furthermore, once a gas bubble is fully developed and stretched out over the complete capillary cross section, they become almost immobile since in these dimensions, capillary forces from the liquid-gas interface are the dominant force. It is, therefore, imperative to keep these bubbles away from the EO pump and the functional liquid part of the fluidic system.

Several methods to avoid mixing the electrolyzed gases with the functional fluidic system have been investigated and reported in literature. Brask et al. [68] used a hybrid approach for the current-coupling by assembling an ion exchange membrane between the electrodes and the EO active capillary. These membranes were permeable for the ionic current and reliably stopped the electrolyzed gases to enter the fluidic system. In order to omit bulky fluidic connections or a membrane, Hug et al. [69] used a design of different electrical resistances within the fluidic system. In their work, the electrodes were placed into top open reservoirs which were connected to wide capillaries. These wide capillaries connected the submicron wide EO pump. Applying a voltage between the electrodes led to a large voltage drop over the EO pump since their fraction of the total electrical resistance was comparatively large. Another approach of omitting bulky fluidic connections and thus allowing further miniaturizing of the EO pump was the integration of photocurable gel electrodes inside the fluidic system as shown by Takamura et al. [70].

All the above mentioned EO pump designs avoided the interaction of liquid and gas inside the microcapillaries, nevertheless, there are publications investigating this interaction in the microdomain. Strategies to handle and separate segmented liquid-gas flows have been developed [71] and in particular, a theoretical description of gas bubbles inside microchannel contractions has been presented by Jensen et al. [72]. In their work, it is mentioned that such contractions exert considerable Young-Laplace pressure on gas bubbles. Paust et al. [73] used microfluidic contractions formed by tapered capillary sidewalls to passively guide gases for direct methanol fuel cells. With the current solutions an integration into the SIP is not possible. A solution for an EO pump with a small footprint, a low actuation voltage and a fabrication suitable for the integration into the SIP needs to be developed.

Here the design, fabrication and analysis of an EO micropump suitable for the integration into the SIP is presented. The mixing of electrolyzed gases within the functional fluidic system is avoided by a novel concept of a liquid-gas-separator (LG-separator). This

LG-separator is placed between the electrodes and the EO pump and it drives the emerging gas bubbles away via an exhaust capillary. The strong capillary forces from the liquid-gas interface in the micrometer ranged capillaries enable the LG-separator to reliably work solely by its geometry.

This chapter is structured as follows: First, the physical background of the liquid-gas separation of the LG-separator is explained. Afterwards, the complete fluidic system containing the LG-separator, the EO pump and the connecting capillaries is modelled to extract the relevant design parameters for the fabrication, as well as the pressures and flows within the fluidic system. Finally, the fabrication process for the EO pump is outlined and the experimental validation of the design is presented.

4.1 Model of an electroosmotic pump with a liquid-gas-separator

As mentioned above, to derive the relevant design parameters, a model of the EO pump with LG-separator embedded into a fluidic system is developed. The model of the LG-separator describes the development of a gas bubble at the electrode and its propagation within the capillary. The complete fluidic system is modelled based on its transformation into an equivalent electrical circuit diagram. This electrical equivalent is solved with the Kirchhoff equations to determine the pressures and flows.

4.1.1 Model of the liquid-gas-separator

Geometry of the liquid-gas-separator and general assumptions

The LG-separator consisted of tapered sidewalls and an electrode integrated into the bottom of the capillary, as shown in Fig. 4.1. It is integrated into the fluidic system with its narrow side, the inlet, oriented towards the EO pump and with its larger side, the outlet, facing the exhaust. The electrode of the pump, at which the gas bubble forms, is located inside the LG-separator, this bubble is geometrically confined by the bottom and the sidewalls. It will be shown in the following section that in a tapered capillary the bubble moves towards the wider side and, hence, away from the electrode. The bubble growth is analytically described in three dimensions. Behind the electrode pointing towards the outlet of the pump, the bubble may stretch over the complete cross section of the capillary and may touch the top. At this moment, the water column within the capillary is separated and any pressure changes between the inlet and the outlet of the LG-separator acts directly on the bubble, respectively on their two independent menisci. The LG-separator compensates for these external pressure changes by its backpressure. In order to model the backpressure, it is assumed that the capillary is much higher than wide and, hence, the curvature of the meniscus is completely defined by the width [74], which reduces the model to two dimensions.

The movement of the gas bubbles was modelled to be quasi static. Effects of lubrication or viscosity were not included. In addition, the model was assumed to be isothermal, since any heat would be immediately removed by thermal conduction through the surrounding bulk silicon (Si). Moreover, the following parameters were used in the model: the viscosity of the liquid (water) $\eta = 1\ \mathrm{mJ \cdot m^{-2}}$, the surface tension of the water-air interface $\gamma_{la} = 73$ mPa·s, and the contact angle of $\theta = 52.3$ for the silicon dioxide (SiO_2) capillary and water.

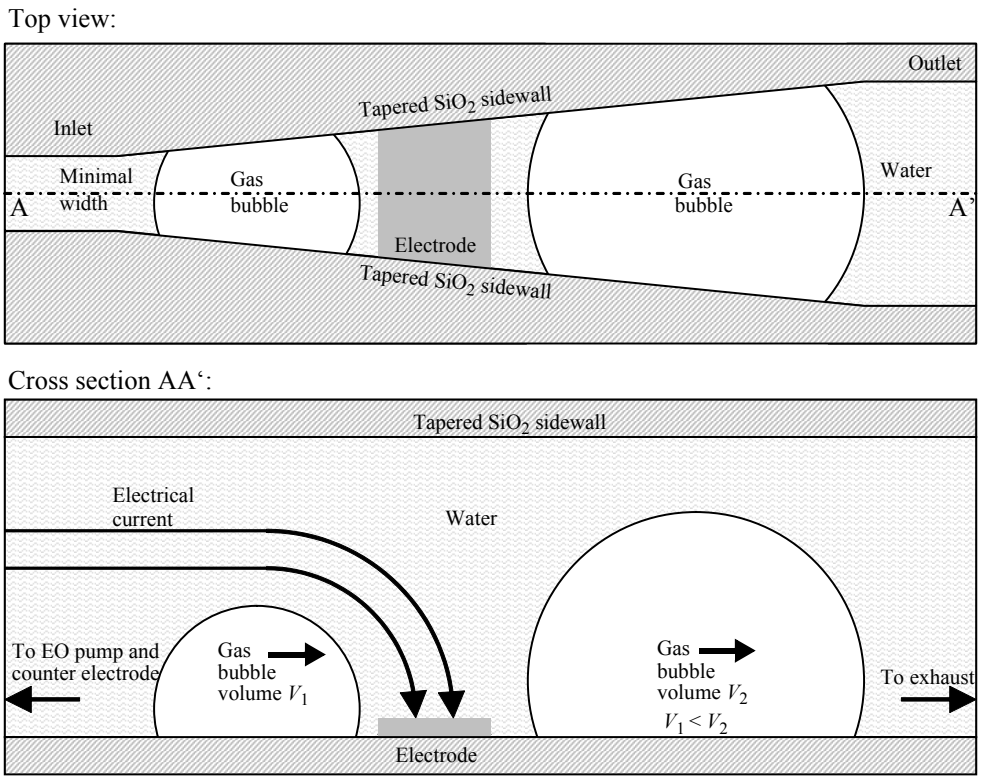

Fig. 4.1 Sketch of the LG-separator. It enables the coupling of electrical current into the solution and the separation of the emerging electrolyzed gas bubbles from the functional liquid fluidic system. Its operation is based on tapered sidewalls which drive the electrolyzed gas bubbles with increasing bubble volume away from the electrode towards the exhaust.

Bubble development at the electrode

Electrolysis initiates the bubble growth at the electrode. Assuming, that the electrolyzed gas conserves its internal energy U_{int}, according to the ideal gas law, enables us to define its internal pressure p_{int} and its volume V

$$U_{int} = p_{int} V . \tag{4.1}$$

In the absence of any external pressures the internal pressure p_{int} needs to match the Young-Laplace pressure p_c, $p_{int} = p_c$, which describes the effect of the liquid gas surface tension γ_{la} confining the liquid-gas interface of the bubble. Due to the properties of a liquid, the shape of the liquid-gas interface is spherical with the radius R. The capillary Young-Laplace pressure p_c can then, according to Eq. (1.8), be described by

$$p_c = \frac{\gamma_{la}}{R} . \tag{4.2}$$

At the bottom, the bubble encounters the transition between three different interfacial energies, the solid-liquid, the liquid-air and the solid-air interfacial energy. At this intersection, Young's equation demands that the angle enclosed by the tangent of the liquid-gas interface and the bottom equals the contact angle θ. Fig. 4.2 a) shows the spherical bubble at the bottom of the capillary. A z coordinate is introduced which is perpendicular to

the bottom of the capillary. The height of the bubble-center is $R_h = R\cos\theta$. Fig. 4.2 b) shows the horizontal cross section of the spherical bubble in its center. Due to symmetry, the bubble's horizontal center is also in the center between the capillary sidewalls. The bubble-center's distance R_w from the tapered sidewall is defined as $R_w = w\cos\beta$, where w is half of the capillary width and β the taper angle of the capillary. The taper of the capillary is defined as $w = w_0 + x\tan\beta$, where w_0 and x denote, half of the initial capillary width at the electrode and the distance of the bubble-center from the electrode, respectively. The direction x is defined to origin at the smaller edge of the electrode and to point towards the outlet of the LG-separator.

This initial bubble B_0 can grow until it touches the tapered capillary sidewall. Its radius R_0 then equals the distance between the center of the bubble and the sidewall $R_0 = w_0\cos\beta$ at the smaller side of the electrode $x_0 = 0$. The internal energy U_0 of the initial bubble B_0 can be calculated to

$$U_0 = p_0 V_0 = \frac{\gamma_{la}}{R_0} \int_{-R_0}^{R_0\cos\theta} \int_{0}^{2\pi} \int_{0}^{\sqrt{R_0^2 - z^2}} r\,dr\,d\omega\,dz. \tag{4.3}$$

As soon as, the initial bubble B_0 touches the sidewall, two more transition points between three different interfacial energies occur, at which the Young's boundary condition requires the contact angle θ. Hence, the bubble needs to change its shape to a new first bubble B_1 and as a consequence its position $x_0 \rightarrow x_1$ shifts within the capillary. Fig. 4.3 a) shows the geometry of the first bubble. The shape of the first bubble B_1 remains spherical, due to the absence of any external pressures. The radius R_1 of the first bubble can be calculated to

$$R_1 = R_w / \cos\theta = (w_0 + x\tan\beta)\cos\beta\,\sec\theta\,, \tag{4.4}$$

which defines the first bubble's B_1 internal energy U_1 to

$$U_1 = \frac{\gamma_{la}}{R_1}\left(\int_{-R_1}^{R_1\cos\theta} \int_{0}^{2\pi} \int_{0}^{\sqrt{R_1^2 - z^2}} r\,dr\,d\omega\,dz - 2\int_{R_1}^{R_1} \int_{0}^{2\pi} \int_{0}^{\sqrt{R_1^2 - z^2}} r\,dr\,d\omega\,dz \right). \tag{4.5}$$

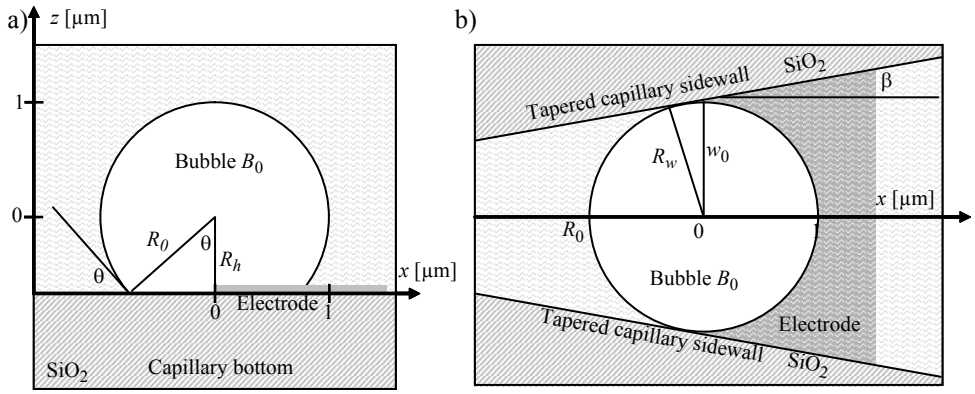

Fig. 4.2 Sketch of the spherical initial bubble B_0. a) Vertical cross section through bubble-center revealing the height of the bubble-center R_h. b) Horizontal cross section through bubble-center revealing the maximum radius of the initial bubble $R_0 = R_w$. In this sketch, the initial opening $w_0 = 1$ µm, the taper angle β = 10° and the contact angle θ = 52°.

This transition from the initial bubble B_0 to the first bubble B_1 is considered to be isothermal. Moreover, the bubble positions and deforms itself faster than new gas is generated by electrolysis. The rate of the gas development can be adjusted by the applied current and this can be chosen small enough to fulfill this criteria, and hence, the bubble can be considered as a closed system during this short transition phase. According to the ideal gas law, the internal energy U_{int} then remains constant

$$U_{int} = U_0 = U_1 . \tag{4.6}$$

Inserting Eq. (4.3) and Eq. (4.5) into Eq. (4.6), replacing the radius R_1 with Eq. (4.4), and solving of the first bubble's center position $x = x_1$ yields

$$x_1 = w_0 \cot\beta \left(\sqrt{\frac{\left(\cos\frac{\theta}{2}\right)^4 (\cos\theta - 2)}{3\cos\theta + \sec\theta(2\sec\theta - 9)}} - 1 \right) . \tag{4.7}$$

Since the square root is less than 1 for $0 < \theta < \pi/2$, the bubble clearly detaches from the electrode and jumps into its new position $x_1 < 0$. This is illustrated in Fig. 4.3 a), where a horizontal cross section through the center of the first bubble B_1.

This shift in position needs to be considered for the placement of the electrode within the LG-separator. The bubble may not escape through the inlet of the LG-separator into the EO pump. The position of the first bubble's center as a function of the taper angle β is shown in Fig. 4.3 b). It can be seen that for small taper angles β the position x_1 of the first bubble reaches far into the narrow part of the capillary. The maximum distance of the bubble's liquid-gas interface into the LG-separator is the same as the minimum distance l_{ie} from the inlet of the LG-separator to the electrode. By the geometry, the minimum distance l_{ie} can be calculated to

$$l_{ie} > w_0 \left[\cot\beta + \frac{\sqrt{\left(\cos\frac{\theta}{2}\right)^4 (\cos\theta - 2)(\cos\beta\sec\theta - \cot\beta)}}{\sqrt{3\cos\theta + \sec\theta(2\sec\theta - 9)}} \right] . \tag{4.8}$$

The minimum distance l_{ie} to the inlet of the LG-separator is shown Fig. 4.3 b), on the right ordinate axis.

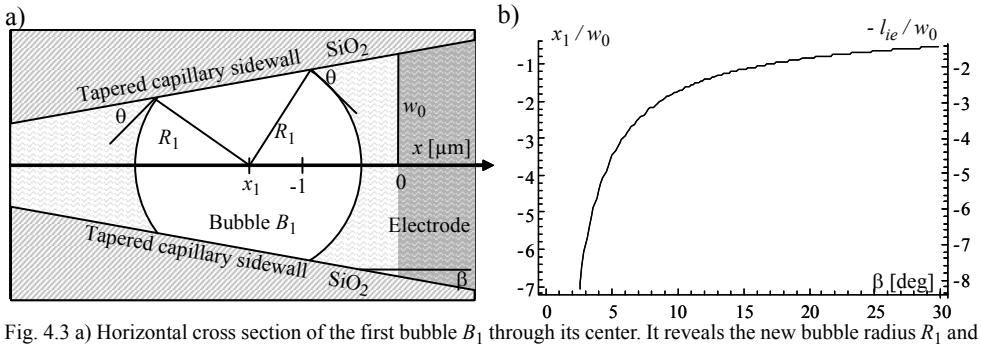

Fig. 4.3 a) Horizontal cross section of the first bubble B_1 through its center. It reveals the new bubble radius R_1 and its position within the capillary x1. In this sketch, the initial opening $w_0 = 1$ µm, the taper angle $\beta = 10°$ and the contact angle $\theta = 52°$. b) On the left ordinate the position x1 of the first bubble B_1 and on the right ordinate the minimum distance from the electrode to the inlet of the LG-separator is shown as a function of the taper angle β.

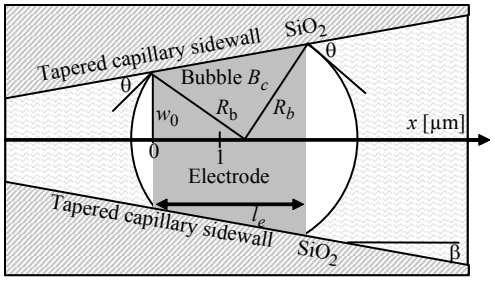

Fig. 4.4 Sketch of the critical bubble at the bottom of the capillary. From this sketch the minimum electrode length l_e can be determined. In this sketch, the initial opening $w_0 = 1$ µm, the taper angle $\beta = 10°$ and the contact angle $\theta = 52°$.

Bubble movement within the liquid-gas-separator

During the electrolysis, continuously more bubbles start to grow at the electrode. These bubbles merge with the first bubble B_1 once their liquid-gas interfaces touch each other. This lets the first bubble B_1 grow and move towards the electrode and then past the electrode and finally out of the LG-separator. During this movement, it is important that the bubble does not disconnect the electrical path between the electrodes which would stop the EO pumping. This might occur in two different ways. First, the bubble may cover the electrode completely, hence, a minimum electrode length l_e is required for preventing this, and second, the bubble stretches out over the complete cross section and reaches the top, hence, a minimum height h_c of the capillary is required. Fig. 4.4 shows the situation of the critical bubble B_c, which is the bubble of which the smaller liquid-air meniscus just touches the small side of the electrode on the capillary bottom. The liquid-gas interface has a circular shape of R_b at the bottom of the capillary. By geometry, $R_b = w_0 / \cos(\beta + \theta)$, and the minimum electrode length l_e equates to

$$l_e > 2R_b \sin(\beta + \theta) = 2w_0 \tan(\beta + \theta). \tag{4.9}$$

For the minimum height h_c, the radius R_c of the critical bubble is needed and can be determined by geometrical considerations to $R_c = R_b / \sin\theta$. From this, the minimum height of the capillary is

$$h_c = R_c(1 + \cos\theta) = w_0 \sec(\theta + \beta)[\cot\theta + \csc\theta]. \tag{4.10}$$

The minimum electrode length l_e and the minimum capillary height h_c as a function of the taper angle β is shown Fig. 4.5. It can be seen that larger taper angles β enforce an even large electrode length l_e and a larger minimum capillary height h_c.

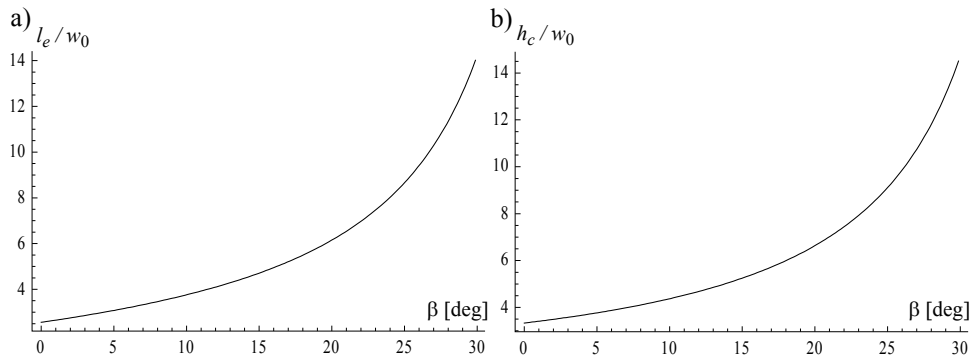

Fig. 4.5 The dimensions of the critical bubble Bc determine the minimum electrode length l_e and the minimum capillary height h_c. a) The minimum electrode length l_e and b) the minimum capillary height h_c as a function of the taper angle β.

Backpressure of the liquid-gas-separator.

During further actuation, the bubble in the outlet section of the LG-separator grows further and eventually stretches out over the complete cross section. At this moment, the bubble separates the water column inside the capillary into two detached liquid-gas interfaces, i.e. into two different menisci. Any pressure difference between the inlet and the outlet of the LG-separator acts directly on the bubble and displaces its respective menisci. In order to still reliably couple the current into the solution, the bubble may not be driven back over or behind the electrode, which could happen if the pressure on the meniscus facing the outlet exceeds the one acting on the other meniscus from the other side by a threshold value. This threshold is built up by the Young-Laplace pressure of the two independent menisci, and it can be considered as the backpressure tolerance p_b of the LG-separator. In order to calculate this backpressure p_b, it is assumed that the capillary is much higher than wide and, hence, the curvature of the meniscus is completely defined by the width [74] which reduces the model to two dimensions. The bubble can then be represented by the two detached menisci, as shown in Fig. 4.6. The dependency of the backpressure p_b on the initial capillary width w_0 and the taper angle β are best explained by setting the initial opening w_0 at the position x_1 of the first meniscus and define the position of the second meniscus by the bubble length l_b. The Young-Laplace pressure drop p_1 and p_2 over the respective menisci can be calculated to

$$p_1 = \frac{\gamma_{la}}{R_1} = \gamma_{la}\frac{\cos(\theta+\beta)}{w_0} \text{ and} \tag{4.11}$$

$$p_2 = \frac{\gamma_{la}}{R_2} = \gamma_{la}\frac{\cos(\theta-\beta)}{w_0 + l_b\tan\beta}. \tag{4.12}$$

Furthermore, for the backpressure p_b the bubble length l_b is parameterized by the bubble parameter $b_p = l_b / w_0$ which leads to the backpressure as

$$p_b = p_1 + p_2 = \frac{\gamma_{la}}{w_0}\left[\cos(\theta+\beta) - \frac{\cos(\theta-\beta)}{1 + b_p\tan\beta}\right]. \tag{4.13}$$

As long as, p_b is positive, the bubble will be reliably conducted away. In order to generate high backpressures p_b, the initial width w_0 of the capillary at the electrode should be chosen as small as possible. The choice of the optimal taper angle β is more complex. Fig. 4.7 a) shows the backpressure p_b versus the parameterized bubble length b_p. For small parameterized bubble lengths b_p, the backpressure p_b becomes negative and the bubble moves to lower values of x. For taper angles $\beta > \pi / 2 - \theta$, the backpressure p_b always stays negative, which represents a hydrophobic behavior of the capillary. The backpressure p_b saturates for long bubbles in the Young-Laplace pressure p_1 of the first meniscus. The maximum bubble parameter b_{pmax} is limited by the distance l_{eo} of the electrode to the outlet

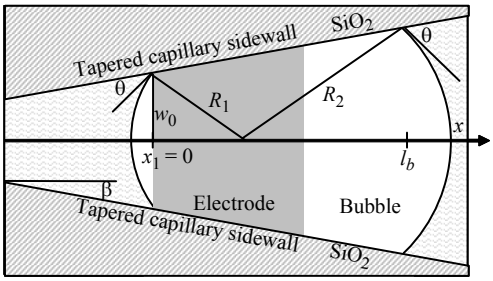

Fig. 4.6 Sketch of an horizontal cross section showing the entrapped bubble stretched over the complete cross section of the capillary. The capillary is cut along the symmetry line in its center. The sketch reveals the two menisci radii, R_1 and R_2 which are essential for the calculation of the LG-separator backpressure p_b.

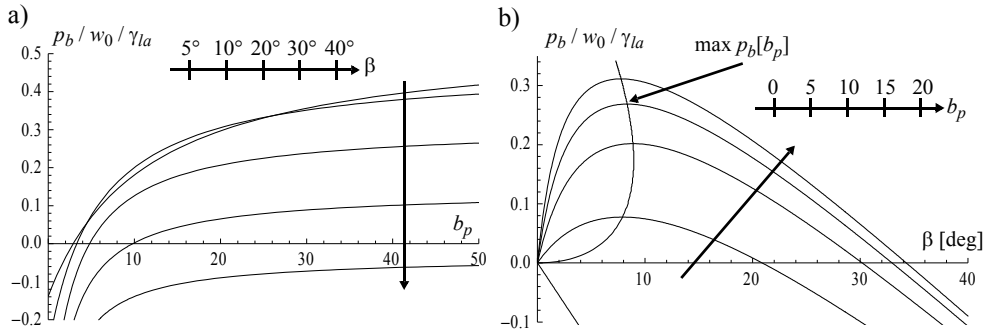

Fig. 4.7 a) The LG-separator backpressure p_b as a function of the bubble parameter. A minimum bubble length is required to have a positive backpressure p_b. At long bubble lengths the backpressure p_b saturates to the Young-Laplace pressure of the first meniscus. The smaller the taper angle β, the higher the saturation backpressure p_b. b) The backpressure p_b as a function of the taper angle β. At small taper angles β the backpressure p_b steeply increases until it reaches its maximum. This maximum is reached, for a contact angle θ = 52°, for a taper angle β < 10° for all bubble lengths.

of the LG-separator $b_{pmax} = l_{eo}/w_0$. Moreover, this assumes that the aspect ratio remains high towards the end of the LG-separator. The backpressure p_b versus the taper angle β is shown in Fig. 4.7 b). The maximum backpressure p_b, reached by a specific taper angle β can be determined from the graph. The backpressure p_b rises steeply for small taper angles β and declines slowly for larger taper angles β. The value of the taper angle β for the maximum backpressure p_b at a contact angle θ of 52° stays below a taper angle β of 10° for all bubble lengths.

Summary of the design parameters for the liquid-gas-separator

Fig. 4.8 shows a LG-separator with its design critical lengths. The capillary width w_0 at the electrode and the taper angle β should be chosen in order to guarantee a reproducible fabrication and a high backpressure p_b of the LG-separator to reliably conduct the electrolyzed gases away. From the above mentioned considerations, the smallest possible capillary width w_0 should be chosen since all critical design values and the backpressure p_b scale with the inverse of the width w_0. In addition a taper angle β of 10° represents a good choice. With this taper angle β, the electrode should be placed according to: The distance of the electrode to the inlet of the LG-separator l_{ie} is about w_0, see Eq. (4.8) and Fig. 4.3 b). The minimum length of the electrode l_e is about 4 w_0, see Eq. (4.9) and Fig. 4.5 a). The distance of the electrode to the outlet of the LG-separator l_{eo} is about 20 w_0, see Eq. (4.13) and Fig. 4.7. The capillary should have a minimum height h_c of about 5 w_0, see Eq. (4.10) and Fig. 4.5 b).

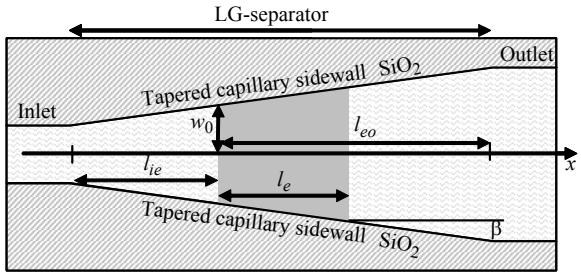

Fig. 4.8 Sketch of the LG-separator showing its critical dimensions. The capillary sidewall has the opening of w_0 at the electrode. The capillary sidewall is tapered with the angle β. The electrode has the length l_e. The small electrode edge has a distance l_{ie} from the inlet and a distance l_{eo} from the outlet.

4.1.2 Model of the complete fluidic system

A sketch of a corresponding fluidic system with an embedded EO pump is shown in Fig. 4.9 a). The chip is fluidically contacted via large reservoirs (capacity 0.2 µl). Within the chip, the EO pump is fluidically contacted by the pump inlet and pump outlet capillary and electrically contacted via the electrodes placed inside a LG-separator.

Filling of the fluidic system and operation of the electroosmotic pump

In order to derive the boundary conditions for the modelling, the filling and the operation of the EO pump needs to be taken into account. For the experiment, a droplet of aqueous solution was placed in the reservoir of the pump inlet and outlet. The Pt electrodes were connected through the contact pads, which were situated in the opening of the exhaust capillary. By applying a voltage between the two electrodes, a current was coupled into the solution. This started the electrolysis and the LG-separator conducted the emerging gas out of the exhaust capillary. At the same time, the current coupled into the solution led to: a proportionally small voltage drop over the first electrode inside the LG-separator and the pump inlet, a proportionally larger voltage drop over the EO pump, and a proportionally small voltage drop from the pump outlet to the second electrode, in the second LG-separator. These voltage drops induced EO pressures and thereby induced a flow through the inlet capillary towards the pump, as well as a flow out of the pump into the outlet capillary.

Flow determination within the fluidic system

Next to the EO induced flow the model needs to integrate the influence of evaporation driven flow through the exhaust capillary, hydrostatic pressure induced flow, and flow induced due to misalignment of the electrodes inside the LG-separator. The layout of the EO pump, as shown in Fig. 4.9 a), can be transformed into an equivalent electrical circuit, as shown in Fig. 4.9 b). The flows and pressures within the EO pump can be determined by solving the equivalent electrical circuit diagram. The capillaries are replaced by resistors with a specific hydraulic resistance as described in chapter 1. R_c, R_p, R_x, denote the hydraulic resistance of the pump inlet and outlet, the EO pump, and the exhaust capillary, respectively. The EO pressures are represented by voltage sources, p_p and p_x for the EO pump and the EO active part of the exhaust capillary. This yields the following equations:

$$p_p = \mu_{eo}\rho_{el}R_pI_{el} \text{ and } p_{x1,2} = \mu_{eo}\rho_{el}(R_{xeo} \pm \varepsilon)I_{el}, \tag{4.14}$$

where R_{xeo} represents the average hydraulic resistance of the EO active part of the exhaust capillary and ε the difference in hydraulic resistance according to an alignment mismatch of the electrodes.

Furthermore, the hydrostatic pressure p_{hy} could have been integrated into the model as an initially charged capacitor. Its value represents the different filling levels in the reservoir of the pump inlet and outlet, as well as an inclination of the chip. However, the consideration as a time independent voltage source p_{hy} simplifies the model and is a reasonable approximation since the displaced liquid volumes are small compared to the volume of the reservoir of about 0.2 µl. If, for example, both reservoirs are half filled, a displaced volume of 10 pl results in a hydrostatic pressure change of 1 µPa, which is negligible compared to the experienced pressures within the fluidic system.

At the transition between the exhaust capillary and the reservoir, a meniscus is formed, due to the sudden enlargement of the cross section. The Young-Laplace pressure of this meniscus prevents a filling of the exhaust reservoir through the capillary. The pressure drop over the meniscus is modelled by an additional voltage source p_m. Without any voltage

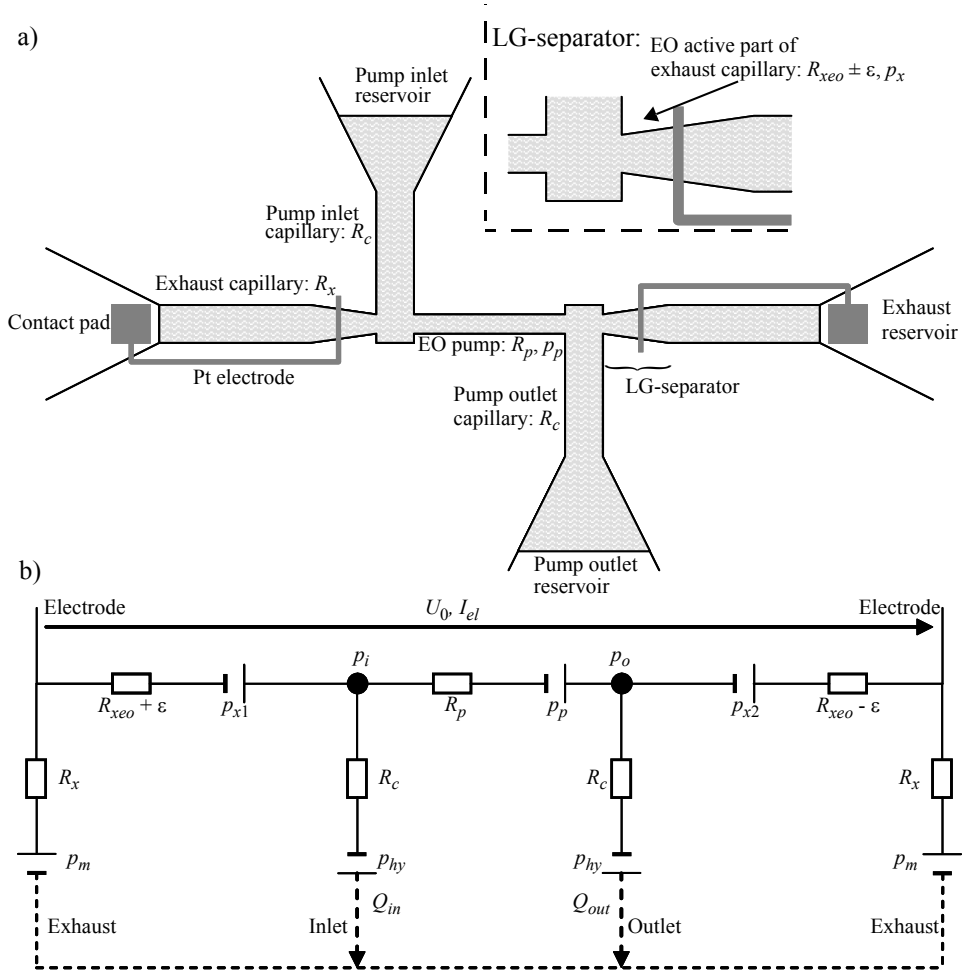

Fig. 4.9 a) Schematic sketch of fluidic system including the EO pump with LG-separator. b) Equivalent electrical circuit for the determination of flow and pressures within the fluidic system.

applied, water already evaporates from the meniscus, inducing an evaporation driven flow ν. This evaporation driven flow defines the value of the voltage source $p_m = \nu\,(R_c + R_x)$ at $I_{el} = 0$. Once the pump is actuated, the shape of the meniscus adjusts according to the applied pressure at the exhaust capillary outlet, which slightly changes the evaporation area, and thus the evaporation induced flow ν.

Integrating all these effects leads to a definition of the Kirchhoff equations for the independent pressure at the pump inlet p_i and pump outlet p_o as:

$$\begin{aligned} \frac{p_i - p_{x1} - p_m}{R_x} + \frac{p_i + p_{hy}}{R_c} + \frac{p_i - p_o + p_p}{R_x} &= 0 \\ \frac{p_o + p_{x2} - p_m}{R_x} + \frac{p_o - p_{hy}}{R_c} + \frac{p_o - p_i - p_p}{R_x} &= 0 \end{aligned} \quad . \tag{4.15}$$

Solving this system of equations for p_i and p_o leads to the flow Q_{out} into the outlet capillary and the flow Q_{in} into the inlet capillary as:

$$Q_{out,\,in} = \nu \pm \frac{p_{hy} R_p R_x}{R_c[R_p R_x + R_c(R_p + 2R_x)]} \pm I_{el}\mu_{eo}\rho_{el}\left(\frac{R_p(R_x - R_{x,\,incl})}{R_p R_x + R_c(R_p + 2R_x)} \mp \frac{\varepsilon}{R_c + R_x}\right) . \tag{4.16}$$

Measuring Q_{out} and Q_{in}, and plotting it versus I_{el}, reveals the contributions from the evaporation induced flow ν, the hydrostatic pressure induced flow p_{hy} and the flow induced by the misalignment of the electrodes ε. At $I_{el} = 0$ the evaporation induced flow ν can be seen as the average offset of Q_{out} and Q_{in}:

$$\left.\frac{Q_{out} + Q_{in}}{2}\right|_{I_{el} = 0} = \nu . \tag{4.17}$$

The hydrostatic pressure difference p_{hy} can be determined from the difference between Q_{out} and Q_{in}:

$$\left.\frac{Q_{out} - Q_{in}}{2}\right|_{I_{el} = 0} = \frac{p_{hy} R_p R_x}{R_c[R_p R_x + R_c(R_p + 2R_x)]} . \tag{4.18}$$

The misalignment of the electrodes is expressed in the derivative of the average of Q_{out} and Q_{in} with respect to the current I_{el}:

$$\frac{d}{dI_{el}}\left(\frac{Q_{out} + Q_{in}}{2}\right) = \frac{\varepsilon\mu_{eo}\rho_{el}}{R_c + R_x} . \tag{4.19}$$

Dimensioning of the capillaries

The requirements on the design of the fluidic system were: A robust implementation regarding the manufacturing process and the actuation, and flows in the range of 10 pl·s^{-1}, which amounts to an average velocity of 50 µm·s^{-1} inside the pump outlet capillary. The EO pump should be, in the future, integrated into the SIP. This constrained the overall height of the capillaries to 10 µm. For the pump outlet and inlet capillaries with a width of 20 µm were chosen. This led to a hydraulic resistance for a 800 µm long capillary which was low compared to the hydraulic resistance of the EO pump. The EO pump had a width of 1.5 µm. This implied a trade-off between reliability during fabrication, appropriate pump backpressure p_b and sensitivity towards clogging. The minimum length of the pump is determined by the rounding of the corners during lithography and thermal oxidation. The minimum pump length was set to 30 µm, for a well-defined hydraulic resistance of the pump. In order to increase the flow, two of those pumps were connected in parallel, which halved the hydraulic and electrical resistance. The exhaust capillary's width was designed to 20 µm and a length of 800 µm to reach the reservoir. This exhaust capillary was placed at the outlet of the LG-separator. The design of the LG-separator was more complex. In order to have the highest backpressure p_b capacity of the LG-separator, an inlet width of 1.5 µm was chosen. The taper angle β was defined to reach a high backpressure p_b while maintaining at the same time the ability to reliably be defined during fabrication. During mask fabrication a tapered line was represented by a pixelated step-like profile with a minimum step size of 250 nm.

These steps needed to be reliably smoothened out during lithography, deep reactive ion etching (DRIE) and thermal oxidation. A safe choice seemed to be a taper angle of $\beta = 11°$, resulting in 39 steps over a length of 50 µm. In order to increase the reliability of LG-separator and to reduce the influence of the corner rounding, a 5 µm long capillary was placed between the entrance of the LG-separator and the EO pump. Finally, the electrode was placed at a distance of 10 µm from the inlet of the LG-separator. This provided enough margin for a possible electrode misalignment. All this resulted in a complete footprint of 100 µm × 15 µm (length × width) of the EO pump.

4.2 Fabrication

Based on the design considerations outlined above, an EO pump with a LG-separator was fabricated. In here, extra attention was taken in order to have a design which is tolerant towards fabrication and modelling uncertainties. In order to identify and verify the optimal design for an EO pump for dispensing and sucking liquids into the SIP, the fabrication process was simplified, compared to the one presented in chapter 2.

4.2.1 Process flow

For the microfluidic system, capillaries with a constant height and variable width, and fluidic connections were required, as well as electrodes inside the capillaries for EO, on-chip pumping. The process flow was based on photolithography, Si etching, thermal oxidation, lift-off metallization and anodic bonding for a two wafer process. A simplified process flow is shown in Fig. 4.10. **a)** The first wafer was a double-side polished, 525 µm thick silicon (Si) wafer. **b)** The capillaries were outlined by DRIE into the frontside of the wafer. The trench-width varied from 2 µm up to 20 µm with a depth of 10 µm for the 20 µm wide capillary. **c)** These capillaries were subsequently narrowed by thermally growing 1.5 µm of SiO_2, which reduced the initial width by 1.65 µm (55% of the SiO_2 grows out of the Si surface [75]). **d)** As it turned out, a SiO_2 thickness of 1.5 µm was too thick for a reliable anodic bond, because of an insufficiently strong electrical field between the two wafers. Consequently, the SiO_2 surface was highly anisotropically thinned by reactive ion etching (RIE) to a final thickness of 100 nm, as suggested by Lee et al. [76] and Plaza et al. [77]. Advantageous was also that more ions were implanted into the SiO_2, which further enhanced the bond-strength. **e)** The fluidic connection to the chip was established by Si-wet-etching the reservoirs. These reservoirs were shaped as cavities through the wafer to also fluidically connect the backside to the frontside. The etching was performed from the backside through the wafer and stopped at the front side at the thin SiO_2 membrane. The Si-wet-etching was first performed in potassium hydroxide (KOH) for a high etchrate and **f)** then finished in tetramethylammonium hydroxide (TMAH) for a gentle stop at the SiO_2. This reduced the risk of etching the SiO_2 frontside, in case a membrane broke. **g)** Finally, the complete SiO_2 was removed from the backside by RIE to ensure a good electrical contact and to open the membranes for the fluidic connection. **h)** The second wafer was a standard boron type glass wafer for anodic bonding. **i)** The metallization of 15 nm tantalum (Ta) and 150 nm Pt was deposited in a lift-off process. **j)** Both wafers were RCA[1] cleaned right before the anodic bonding process. The wafers were aligned in such a way that the capillaries ended in the fluidic connection. The wafers were anodically bonded at 400° C and an applied voltage of 1000 V for 1.5 h.

1. $NH_4OH : H_2O_2 : H_2O = 1 : 1 : 5$ @ 70° C for 1 h

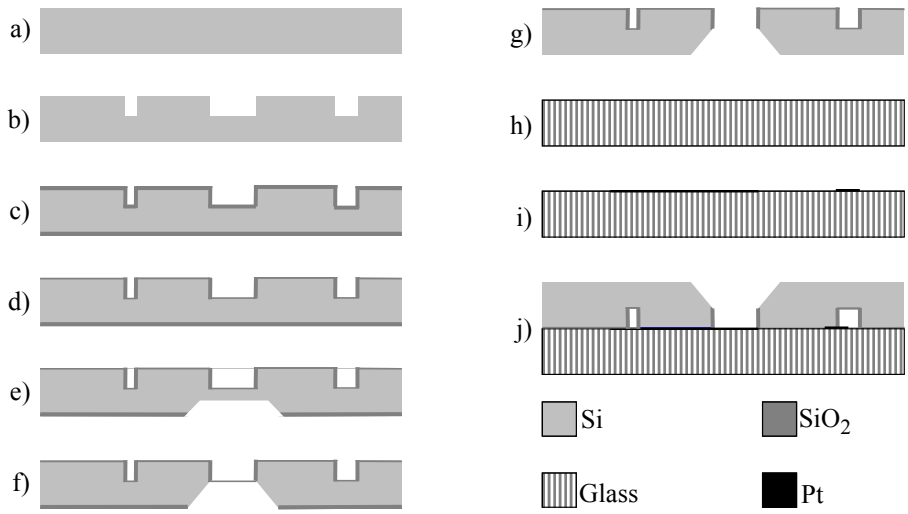

Fig. 4.10 Process flow for the integration of Pt electrodes into the microfluidic capillaries. **a)** double sided polished 525 µm wafer. **b)** Outlining the capillaries as DRIE trenches. **c)** Thermal oxidation in order to narrow down the width of the capillaries. **d)** RIE to thin down the thermal oxide layer on the front surface for reliable bonding. **e)** KOH etching the reservoirs as cavities from the backside of the wafer, stopping inside the Si. **f)** final etching of the cavities in TMAH for soft landing in SiO_2 membrane. **g)** RIE from the backside to remove the SiO_2 for good electrical contact during anodic bonding and to remove the SiO_2 membrane inside the cavities for fluidic connection. **h)** Boron type glass wafer for anodic bonding. **i)** Lift-off metallization of 15 nm Ta and additional 150 nm Pt. **j)** Anodic bonding of the two wafers to close the capillaries

4.2.2 Fabrication results and discussion

The capillary's dimensions were measured for accurately modelling the device. The first measurement determined the height of the capillaries. The well-known phenomena of an aspect ratio dependent etching for DRIE was investigated, the wider the opening, the faster the etch process [75]. It was necessary to extract the precise height of the capillaries with different widths from a test run. Fig. 4.11 a) shows a cross section of DRIE trenches with a width from 1 µm to 20 µm. 50 µm deep trenches were etched, where the etch depth was adjusted for the widest capillary. Fig. 4.11 b) shows the normalized etch depth with regard to the 20 µm wide capillary. This can be used to determine the different capillary heights of the fluidic system and, hence, their hydraulic resistance. Fig. 4.12 a) shows two important results: the width of the EO pump and the rounding of the corners. The width of the EO pump can be

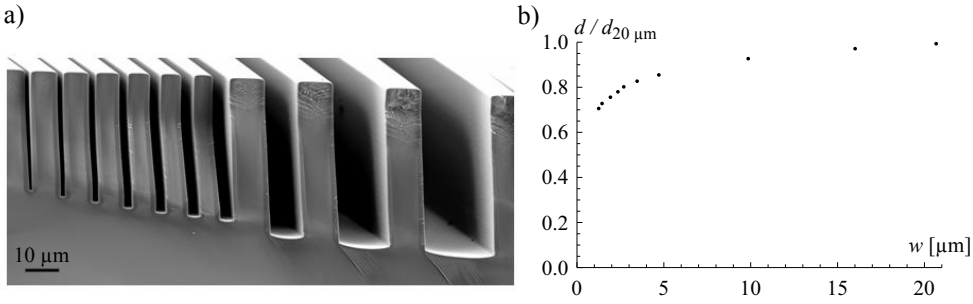

Fig. 4.11 a) Scanning electron microscope (SEM) image showing that the depth of the DRIE trenches depended on the width of the capillaries. b) The normalized depth with respect to a 20 µm wide capillary, extracted from a).

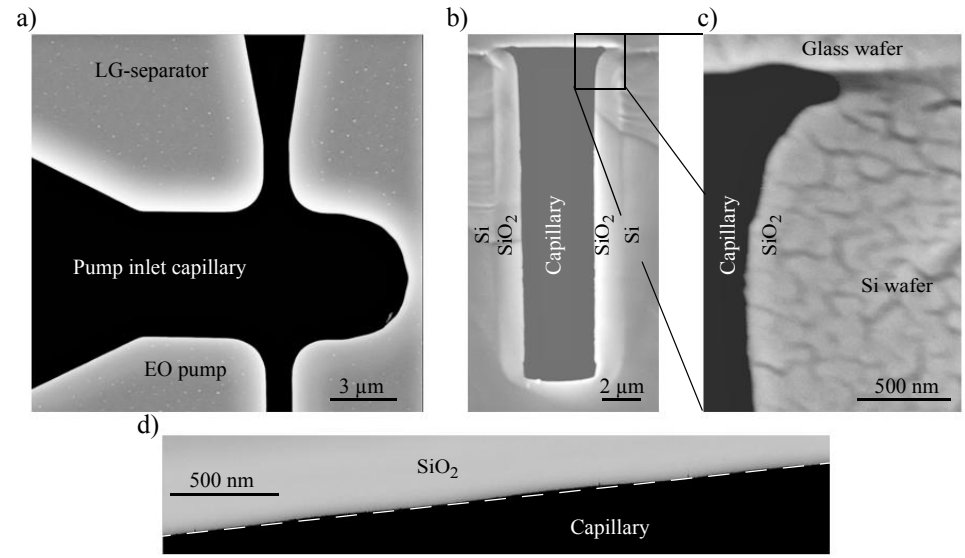

Fig. 4.12 SEM images of: a) Top view of a DRIE and thermally oxidized pump inlet with the exhaust capillary on the top and part of the EO pump at the bottom. The corners were rounded with a radius of 2.2 µm. The width of the EO pump was determined to 1.5 µm. b) and c) Shows a cross section of pumping capillary. b) The sidewall of the capillary deviated of about 1° from verticality. The thermal oxide thickness can be determined to 1.4 µm. c) The imperfection of the bonding on the top corner resulted in enhanced cornerflow but has no major consequences during the actuation of the pump. d) The stepping of the tapered sidewall of 5° resulted in a local variation of the taper angle β ± 0.6° after etching and thermal oxidation.

determined to be 1.5 µm. The intended width of 0.5 µm could not be reached probably, due to widening during the DRIE. In future, this needs to be narrowed down in order to generate higher EO pump backpressures. The corners were initially rounded with a radius of 2 µm in the mask design to avoid stress concentrations and ensure repeatability in fabrication. The corner radius increased only up to 2.2 µm during fabrication. The cross section of the capillary was investigated by cutting it open, as shown in Fig. 4.12 b). For a 20 µm deep and 4 µm wide capillary, an inclination angle of the sidewall of 89° was measured, justifying the assumption of a rectangular capillary cross section. In addition, the 1.4 µm thick SiO_2 capillary sidewall can be seen, indicated by the higher greyscale. Finally, the top corner of the capillary rounded off during DRIE, thermal oxidation and RIE. The radius for this edge was measured to be 0.6 µm. After bonding, this recess resulted in a shallow 0.3 µm wide and 0.2 µm high additional capillary, see Fig. 4.12 c). This shallow part of the capillary did not make a contribution to the hydraulic resistance but increased the cornerflow. A closer look was taken at the pixelation of the tapered sidewall to determine the minimum taper with acceptably rounded off steps. The problem with the pixelation of diagonal lines in the mask design is addressed in Fig. 4.12 d). For a low taper angle β of 5°, only a slight deviation from the diagonal line of 20 nm per 1 µm long step was detected. This resulted in a local variation of the taper angle β of ± 0.6°.

A result of the Pt lift-off process is shown in Fig. 4.13 a). A triangle with an opening angle of 25° resulted in a curved edge with a radius of 500 nm. This was a sufficiently small feature size, since the minimum Pt features in this design were 10 µm. However, the 185 nm thick Ta/Pt line had a strong influence on the bonding quality, as shown in Fig. 4.13 b). It resulted in a non bonded area along the Pt line with a distance up to 25 µm away from the Pt

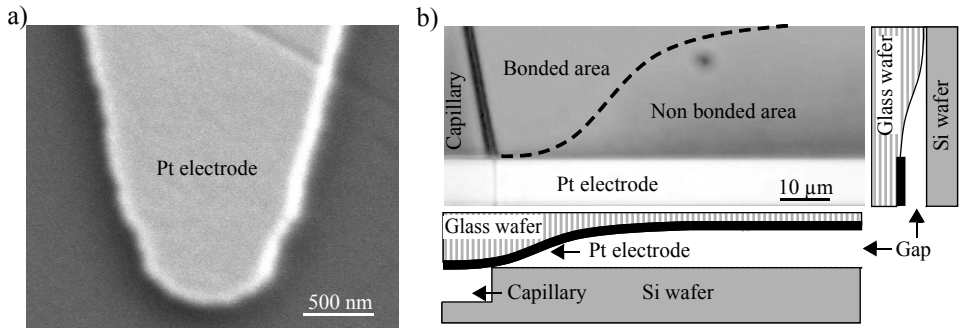

Fig. 4.13 a) SEM image of a Pt lift-off fabricated tip with a opening angle of 25°. The tip rounded of with a radius of 500 nm, which defines a sufficient small feature size for the fabrication. b) Optical microscope image of a non bonded area underneath the Pt electrode. This imperfection imposed a major reliability issue during actuation since hydrolysis can occur in this small gap and the emerging gases may leak into the pumping capillaries.

edge. This non bonded area decreased the closer it reached the capillary. Two effects can explain this void in the bond: the steric hindrance of the Pt line and the gas enclosure during the bonding step underneath the electrode. These gases, emerging during the bonding, were partially removed via the capillaries, which were connected to the outside. Applying a vacuum, in the range of 10 mbar, to support the extraction of this gas, did not increase the bonding quality. In this case, a plasma occurred between the electrodes and this plasma current limited the applied voltage of the bonding setup to less than 1000 V. These gaps imposed a major drawback, not because of a liquid connection, since their hydraulic resistance was comparably high, but because hydrolysis occurred at higher currents in these gaps. These emerging electrolyzed gases escaped into the pumping capillary.

4.3 Experiments, results and discussion

In the first part of this section, the LG-separator for reliably venting the electrolyzed gases was investigated with respect to its backpressure p_b tolerance and its gas-flow driving capability. In the second part, the EO pump was analyzed regarding to its linearity of the pump rate versus the electrical current, and the validity of the fluidic systems model. For each experiment, the chips were cleaned in an oxygen plasma for 20 min. to remove any organic residues and to activate the SiO_2 surface. For the experiments the capillaries were filled with deionized water[1] having a specific resistivity of 12 MΩ·cm. As flow marker a low concentration of 0.1 mmol·l^{-1} fluorescein[2] solution was employed.

4.3.1 Liquid-gas-separator

The first experiment verified Eq. (4.11), which states that the Young-Laplace pressure depends on the taper angle β. The experiment compared two taper angles β_1, β_2 by passively entrapping a gas bubble in a 10 µm deep capillary with a maximum width at the meniscus of 5 µm. An optical image of the capillary layout is shown in Fig. 4.13 a). The capillaries were filled by water flowing in from the bottom and the air being pushed out of the system through the top. The flow split at the split-point into two independent flows. In the following section of the capillary, it was important that the meniscus progressed with the same speed, until it reached the entrapment-point. From that moment onwards, the gas bubble was entrapped in

1. Elga, Purelab UHQ
2. Fluka, Fluorescein sodium

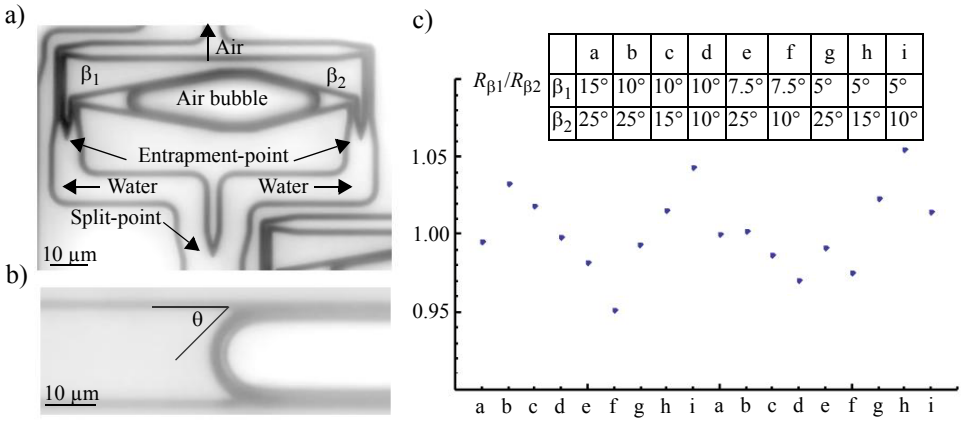

	a	b	c	d	e	f	g	h	i
β_1	15°	10°	10°	10°	7.5°	7.5°	5°	5°	5°
β_2	25°	25°	15°	10°	25°	10°	25°	15°	10°

Fig. 4.13 Optical microscope image of: a) an entrapped air bubble in tapered capillary and b) of the static contact angle θ inside the capillary. c) Ratio between the radii of two opposing mensici in a capillary with two different taper angles β_1 and β_2.

the middle capillary and compressed by the Young-Laplace pressure. After a certain time the bubble stayed at its equilibrium position, hence, the pressure inside the gas bubble was constant and must have matched the Young-Laplace pressure of the two entrapping menisci.

For a set of paired taper angles β_1, β_2 two different meniscus positions were investigated by entrapping two different volumes of air. For the analysis, the capillaries were filled and the images were taken immediately afterwards, in order to avoid the dissolution of air in water. The contact angle θ of water on SiO_2 inside the capillary was measured to be θ = 45°, as shown in Fig. 4.13 b). The Young-Laplace pressures at the meniscus was determined by measuring radius of the meniscus in horizontal cross section of the capillary center. According to Eq. (4.11), the Young-Laplace pressure was equal for both menisci in case their radius was equal. For the investigated taper angles β a good matching of the Young-Laplace pressure of the two menisci can be concluded, as shown Fig. 4.13 c). The ratio between the measured radii was 0.999, which was close to one representing a perfect matching. The standard deviation of this experiment was 0.026.

In order to calculate the maximum backpressure p_b of the LG-separator (β = 11°, w_0 = 2.7 µm and electrode placement of l_{ie} = 12 µm from the inlet), the capillary Young-Laplace pressure p_1 of the first meniscus needed to be calculated. According to Eq. (4.11), the capillary pressure of the first meniscus was calculated to be p_1 = 16.1 kPa. The Young-Laplace pressure p_2 of the second meniscus in the exhaust capillary needed to be assessed differently, since the exhaust capillary had a cross section with an aspect ratio of only 1. According to White [78], the capillary pressure of a rectangular cross section can be estimated by substituting the radius of the meniscus by the hydraulic radius $r_h = A/s/\cos\theta$, where A is the cross sectional area and s the wetted circumference. This leads to a Young-Laplace pressure p_2 of the second meniscus to p_2 = 15.5 kPa. Based on Eq. (4.13) the backpressure p_b of the LG-separator can be calculated to p_b = 0.6 kPa with θ = 45°, β = 11° and w_0 = 2.5 µm. This defined its tolerance towards pressure changes which can be caused by contact angle θ changes due to contamination or cross section changes.

Finally, the gas flow driving capability of the LG-separator when integrated into the EO pump was investigated at a driving current of 20 nA and with using deionized water. Fig. 4.14 shows three images, taken with a time difference of 7 s, of the emerging gas bubbles in the exhaust capillary. Based on that, the flow of hydrolyzed gas was evaluated to be 2 pl·s^{-1}.

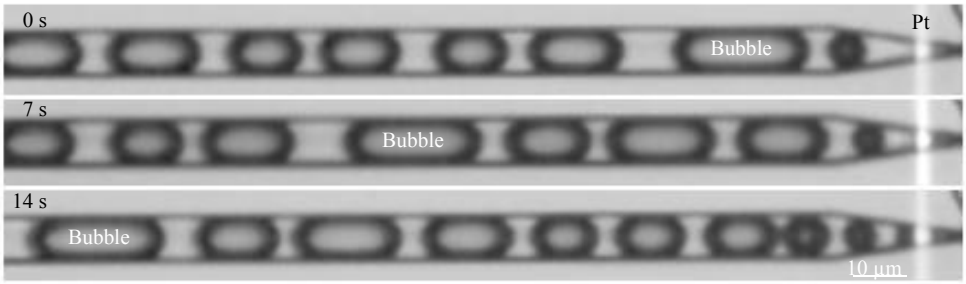

Fig. 4.14 Optical microscope image of an active LG-separator with a driving current of 20 nA. The time difference between the images was 7 s. The hydrogen evolution is estimated to generate a flow of 2 pl·s^{-1}.

4.3.2 Electroosmotic flow determination

Experimental setup

For determining the EO flow, deionized (DI) water was chosen as the liquid to be propelled. Using deionized water resulted in a large Debye layer thickness λ_D on the SiO_2 surface, due to the low concentration of ions; see also chapter 1 for more information. This led to a high EO mobility μ_{eo} and, hence, to an enhanced flow. A drawback of the current design was that water evaporated out of the pumping capillaries' reservoirs during the experiment and, therefore, keeping a constant concentration of ions in the solution was impossible. The evaporation would have also concentrated any contaminations in the reservoir and, by diffusion, in the capillaries. In order to perform several measurements with the EO pump, the least contaminating solution, deionized water, was chosen. To trace the pumping action inside the capillary, a plug of fluorescein solution was chosen. In these geometric dimensions and time frames, the fluorescein-DI-water interface formed a clear meniscus, which was only slightly influenced by diffusion. The pump was actuated in a way that the fluorescein solution never reached the EO pump in order to avoid any contamination in the EO active part.

For the experimental setup, the chip with the pump was placed on an inverted florescence microscope[1], where the propagation of the fluorescein solution was monitored in a 400 µm long section of the pump outlet capillary. The low concentration of fluorescein and the resulting low fluorescent emission allowed a maximum frame rate of 14 frames per second. Special attention was paid to the brightness and contrast settings. The greyscale inside the capillary was chosen at a linear scaling from 0.15 up to 0.55 where 0.15 represented deionized water and 0.55, the fluorescein solution of 0.1 mmol·l^{-1}.

For the measurement, the electrodes were contacted via the contact pads inside the reservoirs of the exhaust capillary. Then, a droplet of deionized water was dispensed into the reservoir of the pump inlet and finally, a droplet of fluorescein solution was filled into the reservoir of the pump outlet. A sequence of images was taken, as shown in Fig. 4.15, and analyzed according to the greyscale distribution in the center of the capillary. A reference point, which was not affected by diffusion, needed to be found in order to follow the initial transition point between deionized water and fluorescein solution. Hence, it was assumed that the greyscale average between 0.55 and 0.15 represented half of the fluorescein concentration. In addition, the diffusion of fluorescein into deionized water and the diffusion of deionized water into the fluorescein solution was assumed to be more or less the same at

1. Zeiss, Axiovert S40 with a mounted camera AxioCam Mrm and a metal halide lamp HXP 120

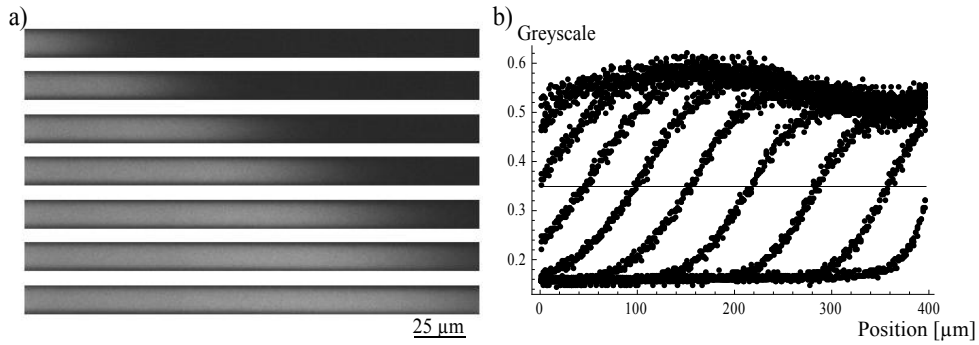

Fig. 4.15 a) Fluorescent microscope image of the flow of fluorescein solution into the fluidic system replacing deionized water. Images taken with a time difference of 200 ms in a 400 µm long capillary. b) Greyscale distribution in the center of the capillary deduced out of a).

the low concentration used. Hence, a greyscale of 0.35 was not affected by diffusion, and its progression in the center of the capillary was considered as the location of the original interface and traced. Fig. 4.15 shows a series of 5 consecutive greyscale distributions along the capillary's center. From this, the velocity v_{tp} of the transition point was obtained, which was then further transformed into the flow Q. According to Eq. (1.2) with $p_{hy} = QR_{hy}$, $y = 0$ and $z = h/2$, the center velocity v_{tp} for a Poiseuille flow in a rectangular capillary can be described as:

$$v_{tp} = \frac{48Q}{\pi^3(hw - 0.63h^2)} \sum_{n,\,odd}^{\infty} \frac{1}{n^3}\left[1 - \frac{1}{\cosh\left(n\pi\frac{w}{2h}\right)}\right]\sin\left(\frac{n\pi}{2}\right) \quad . \tag{4.20}$$

Solving the sum numerically for the exhaust capillary cross section with $w = 2h$ yields the flow Q depending on the center velocity v_{tp} as:

$$Q = \frac{h^2 v_{tp}}{0.9974} . \tag{4.21}$$

Flow measurement and model verification

This subsection determines and compares the four flow contributions with the model: evaporation induced flow ν, hydrostatic pressure p_{hy} induced flow, EO flow induced by the misalignment of the electrodes ε, and the intended EO flow. For the model validation, the solution's specific resistivity ρ_{el} and the EO mobility μ_{eo} needed to be experimentally defined. The solution's resistance was determined from Fig. 4.16 a) showing the current versus the potential applied between the bondpads of the electrodes. The nonlinearity in this graph was caused by the current-coupling of the electrode from the Pt into the solution. The consequence for the EO pump was, that for small currents, most of the potential drop occurred within the current-coupling of the electrode and not over the EO pump. With higher currents, the electrical resistance of the EO pump became more dominant and, hence, most of the applied voltage dropped over the EO pump. This can also be seen, by the curve converging towards a linear, ohmic behavior. To estimate the electrical resistance of the solution, the slope at a high potential, at 4.7 V, was determined. The electrical resistance of the solution was determined to be $R_{es} = 230$ MΩ. With the geometry, the specific resistance of the

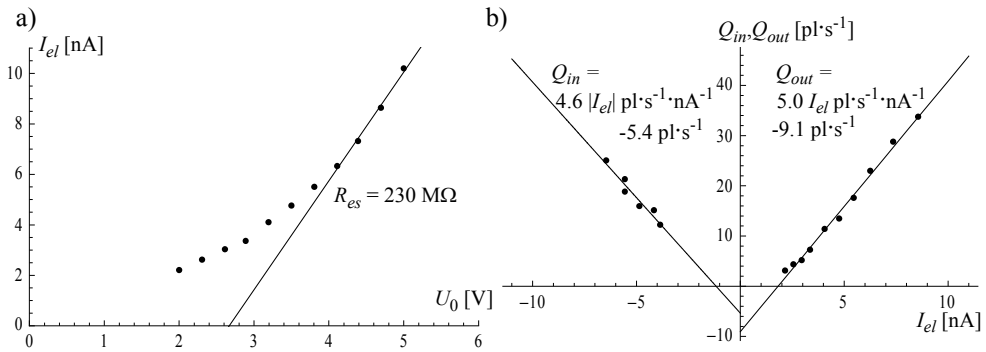

Fig. 4.16 a) Voltage current curve of the EO pump. At low voltages the system is mainly determined by the current-coupling of the electrode. The higher the applied voltage the higher the voltage drop over the fluidic system. The curve approaches the ohmic behavior of the solution inside the fluidic system. b) Current dependency of the flow into the EO pump Q_{in} and the flow out of the EO pump Q_{out}. At zero EO current the median of the two flows was induced by evaporation through the exhaust capillaries. The difference between the two flows was induced by a hydrostatic pressure between the two reservoirs connected to the in and outlet of the EO pump. The different slopes of the flows were introduced by misalignment of the electrodes within the LG-separator.

solution was calculated to be ρ_{el} = 100 Ωm. This was contradicting to the initial specific resistance of the deionized water, but could be explained by minute liquid volume inside the fluidic system. The specific resistance in this small amount of liquid is highly influenced by the concentration of hydroxide (OH^{-1}) and hydronium (H_3O^+) ions electrochemically generated at the electrodes and the presence of a small amount of contamination as a remaining from the fabrication process. In order to understand this decreased specific resistance of the solution, the kind and concentration of contaminating ions was estimated. The source of the contamination was speculated to be the residues of etching during fabrication and dissolved ions from the doped anodic bonding glass. Furthermore, the contamination is expected to be more of a saline character than an organic one, since the chips were cleaned in an oxygen plasma right before usage. Another observation supports this assumption that no local variations of the contact angle θ inside the capillary were detected which are a good indicator of organic contaminations. To assess the ionic concentration c of the contaminants, Kohlrausch's law and Ostwald's law of dilution was used. A solution's specific resistance of 100 Ωm can be reached with an ionic concentration c in the range of 1 mmol·l^{-1}, based on an estimated average limiting molar ionic conductivity in the range of 0.1×10^3 S·cm^{-2}·mol^{-1} (hydroxide ion, hydronium ion, alkali metals, values for the average taken from Coury [79]).

Knowing the ionic concentration c of the solution allowed to estimate the EO mobility μ_{eo}. The ionic concentration c led to a Debye layer thickness λ_D in the range of 10 nm on a charged SiO_2 surface. The surface charge σ_{ch} at neutral pH values was determined by Zhou et al. [80] to σ_{ch} = 0.026 C·m^{-2}. Finally, this can be used to estimate the EO mobility to $\mu_{eo} = 3 \times 10^{-7}$ m^2·V^{-1}·s^{-1}. Moreover, the here derived values of the Debye layer thickness λ_D and the EO mobility μ_{eo} were in good correspondence with those given by Wang et al. [81].

The experimental result for the flow Q_{out} out of the pump and the flow Q_{in} into of the EO pump are shown in Fig. 4.16 b) and summarized in Table 4.1. The evaporation induced flow ν, was determined to be ν = 7.2 pl·s^{-1}, according to Eq. (4.17). The modelled value for evaporation induced flow was in the range of 7.4 pl·s^{-1}. This value is based on the model developed in chapter 3, with an evaporation area of 2 times 9 µm × 20 µm at a temperature

of 20° C and a relative lab humidity of 33 %. The hydrostatic pressure p_{hy} induced flow was determined to be 3.7 pl·s^{-1}, according to Eq. (4.18). The hydrostatic pressure p_{hy} was related to a height difference of the meniscus in the pump inlet reservoir with respect to the meniscus in the pump outlet reservoir. From Eq. (4.18) a hydrostatic pressure difference of p_{hy} = 1.7 Pa was calculated. This corresponds to a height difference of the meniscus in the inlet reservoir of 0.17 mm, lower than in the outlet reservoir. The misalignment of the electrodes was optically determined to be 2 µm into the exhaust capillary of the pump inlet. The induced EO flow difference between Q_{out} and Q_{in} was determined to be 0.4 pl·s^{-1}·nA^{-1}, according to Eq. (4.19). Using the model and including the values for the specific resistance, the EO mobility μ_{eo} and a 2 µm electrode misalignment led to an EO flow of 0.5 pl·s^{-1}·nA^{-1}. Finally, the general EO induced flow was determined to be Q_{ineo} = 4.6 pl·s^{-1}·nA^{-1} and Q_{outeo} = 5.0 pl·s^{-1}·nA^{-1}, which is in good agreement with the modelled values of Q_{ineo} = 4.6 pl·s^{-1}·nA^{-1} and Q_{outeo} = 5.1 pl·s^{-1}·nA^{-1}.

Tabel 4.1: Flows within the fluidic system

	Measured	Modelled	
Evaporation induced flow ν	7.2 pl·s^{-1}	7.4 pl·s^{-1}	
Hydrostatic pressure p_{hy} induced flow	3.7 pl·s^{-1}		p_{hy} = 1.7 Pa
Electrode misalignment ε induced flow	0.4 pl·s^{-1}·nA^{-1}	0.5 pl·s^{-1}·nA^{-1}	Misalignment 2 µm
Flow into EO pump Q_{ineo}	4.6 pl·s^{-1}·nA^{-1}	4.6 pl·s^{-1}·nA^{-1}	
Flow out of EO pump Q_{outeo}	5.0 pl·s^{-1}·nA^{-1}	5.1 pl·s^{-1}·nA^{-1}	

4.4 Summary and conclusions

To summarize, a successful analytically modelling and realization of an EO pump was shown. The novel approach of implementing a LG-separator, based on a tapered capillary, allowed the current-coupling from the Pt electrode into solution without mixing the emerging electrolyzed gases with the pumping liquid. Likewise, an easy fabrication technique based on a standard MEMS process and anodic bonding can be employed. All this resulted in an EO pump with a very small footprint of 100 µm × 15 µm (length × width) and an actuation with a low voltage of 2 V to 5 V.

The LG-separator had a maximum backpressure of 0.6 kPa and was able to reliably conduct away gas flows in the range of 2 pl·s^{-1} generated by a current of 20 nA. The EO pump was modelled and measured. For deionized water, a flow out of the EO pump of Q_{out} = 5.0 pl·s^{-1}·nA^{-1} was achieved. At an applied voltage of 5 V, a current of 10 nA was measured which amounts to a flow of 50 pl·s^{-1}. The developed model for the fluidic system also integrated effects like hydrostatic pressure and evaporation, as well as fabrication imperfections like misalignment of the electrodes.

For a more detailed understanding of the electrode behavior a wider range of applied potentials is necessary. This would also allow a better prediction of the solutions specific conductivity and, hence, the EO mobility. In order to increase the backpressure of the EO pump an optimization can be achieved by connecting these pumps in series to obtain a multistage EO pump, as suggested by Takamura et al. [70]. Special attention needs to be taken in the design of the exhaust capillaries, since they will have to compensate for the increasing pressure between the stages. Moreover, a promising direction for further investigation would be the usage of the Pt electrodes for the electrochemical characterization of the pumping solution.

4.5 Outlook

Two different aspects are addressed in this section: First, the integration of the EO pump into the SIP and its dimensioning, for dispensing and sucking in liquids. Second, a first experiment of electrodeposition inside closed microfluidic capillaries with the help of the LG-separator is described.

4.5.1 Model of an electroosmotic pump integrated into the scanning ion pipette

This section briefly describes a design strategy to optimize the flow out of the EO pump with a fixed hydraulic load at its outlet. In case of the SIP, this hydraulic load is defined by the outlet hole in the tip. The flow out of the EO pump will be named dispensing flow in the following. The pump setup is comparable to the one sketched in Fig. 4.9 a), except that the electrodes are no longer electrically contacted via the reservoir of the exhaust capillary. Both, the exhaust capillaries and the pump inlet and outlet are completely filled with water in order to avoid suction by evaporation in case of a non actuated EO pump. The integration of the EO pump into the SIP requires a maximum overall height of the capillaries of 5 µm, in order to have a reasonable low cantilever stiffness, suitable for scanning force microscope imaging. From a fabrication point of view, the dimensioning of the capillaries for the fluidic system with an embedded EO pump can be chosen as follows: The capillaries for the pump inlet and pump outlet can be designed with a width of 20 µm. This leads to negligible hydraulic resistance even for capillary lengths of up to 1 mm. The width of the EO pump can be fabricated reliably down to 0.5 µm. The length is chosen to be 7.5 µm. In order to increase the hydraulic resistance of the exhaust capillaries, their width is chosen to be 4 µm, which should still provide enough margin for the LG-separator to reliably conduct the electrolyzed gases away. The length of the exhaust capillaries was chosen to be 2 mm for a high hydraulic resistance. The LG-separator should have a taper angle β of 5° with an inlet opening of 1 µm for a a sufficiently high backpressure. In order to reduce the EO active part of the exhaust capillary, the electrodes should be placed at a distance of 5 µm away from the inlet into the LG-separator. To compensate for corner rounding, a 1 µm wide and 3 µm long capillary connects the LG-separator to the EO pump inlet. For the hydraulic load, the radius of the hole in the tip is expected to be in the range of 100 nm, which is a compromise between reasonable dispensing flow and localization.

The flows and pressures are modelled in a similar approach as described earlier. Instead of the applied current, I_{el}, the applied voltage, U_0, is used, to express that the actuation of the

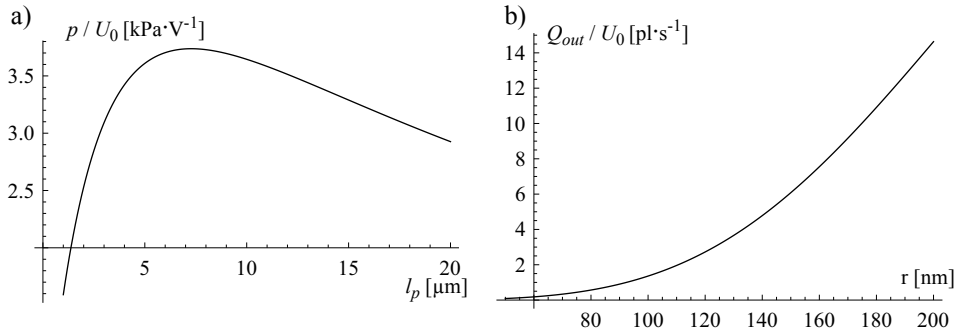

Fig. 4.17 a) Maximum EO pump backpressure per applied voltage depending on the EO pump length. b) Dispensing flow through a hole in the tip per applied voltage depending on the tip hole radius. ($\rho_{el} = 100\ \Omega{\cdot}m$, $\mu_{el} = 3 \times 10^{-7}\ m^2{\cdot}V^{-1}{\cdot}s^{-1}$)

EO pump can be performed at low voltages. Moreover, for these capillary dimensions, an EO pump length of already 1 µm leads to an electrical resistance of 300 MΩ, which is already close to the linear ohmic behavior of the EO pump, as shown in Fig. 4.16 a). For the modelling an EO mobility $\mu_{el} = 3 \times 10^{-7}\ m^2 \cdot V^{-1} \cdot s^{-1}$ and the solutions specific resistance $\rho_{el} = 100\ \Omega \cdot m$ was assumed. The backpressure at different pump lengths was calculated and presented in Fig. 4.17 a). For an optimal length of 7.5 µm, an EO pump backpressure of $p = 3.7\ kPa \cdot V^{-1}\ U_0$ can be reached. From Fig. 4.17 b) the dispensing flow through a 100 nm radius hole in the tip can be determined to be $Q_{out} = 1.5\ pl \cdot s^{-1} \cdot V^{-1}\ U_0$. This dispensing flow characteristic is in good agreement with the desired flow rates presented in chapter 2.

4.5.2 Electrodeposition inside closed capillaries

The LG-separator allowed the electrodeposition of metals inside closed capillaries, for example, the electrodeposition of silver (Ag). In that case a good process control could be achieved, since the current can be used to control the deposition rate of Ag. The idea was to generate a flow of electrodeposition solution over the electrode, which will be plated, towards the counter electrode. The flow rate must be sufficiently high, in such a way that the number of Ag ions lost due to electrodeposition is negligible, hence, the solution composition remains constant. The flow rate over the electrodes can be generated i.e. by an evaporation driven pump, since it is able to generate high flow rates relatively independent of the ionic concentration. In order to generate a homogeneous field over the to be plated electrode, the potential drop over the LG-separator needed to be comparably high. Once a sufficiently high potential between the electrodes is applied, the current induced a Ag deposition at the Pt deposition electrode, and water hydrolysis at the counter electrode, inside the LG-separator.The deposition quality could be monitored in-situ, by measuring the resistance of the Pt/Ag line and comparing it with the specific resistance of Ag.

First experiments were conducted for a solution of 0.01 $mol \cdot l^{-1}$ silver nitrate ($AgNO_3$) at a current of 100 nA, for 10 min. In Fig. 4.18, a silver layer was grown on the Pt electrode. In addition, a successful conduction of the emerging gases away from the counter electrode can be seen. For further improvement, complexing agents, like thiosulfate, should be added to obtain a denser layer with higher specific conductivity [82-84].

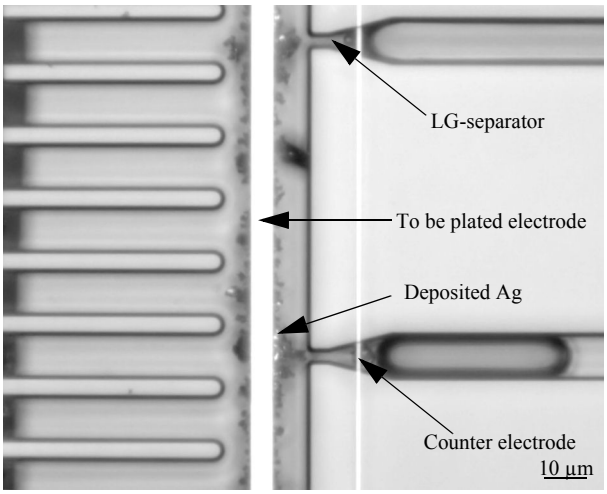

Fig. 4.18 Optical microscope image of an electrodeposition of silver inside closed microfluidic capillaries. The Pt line was used as the start electrode for the deposition. The counter electrode was placed inside the LG-separator. Conditions for this experiment were 0.01 $mol \cdot l^{-1}$ $AgNO_3$ at a current of 100 nA for 10 min.

Chapter 5

Integration of Ag electrodes into the scanning ion pipette

In the presented case, the crucial step of the scanning ion pipette (SIP) fabrication is the fuse bonding and the creation of the silicon dioxide (SiO_2) capillary walls during the thermal oxidation at 1100° C. A structured standard metal electrode within the SIP will not be able to withstand such high temperatures. Hence, the electrode needs to be deposited and structured as a post and preferably batch-like process. Unfortunately, commonly used and established metal deposition techniques like evaporation, sputter deposition or electroplating require open structures. Therefore, electroless deposition of the electrode becomes an interesting option for our case. It provides a unique and highly flexible method to deposit and structure metal films inside closed capillaries. The idea is to fill a solution of metal ions together with a reducing agent into the capillaries. During the electrochemical reaction, the metal layer starts to grow on the sidewall of the capillary forming the electrode. Especially Ag represents a good candidate for electroless deposition, since the proper process is well established, using the so called Tollens reaction [85-88]. Moreover, Ag is highly conductive and noble, hence, corrosion problems within the very thin deposited layer are reduced.

In literature, electroless deposition was used to fabricate three dimensional complex metallic micro and nanostructures [89], three electrode electrochemical sensor [90], microthermocouple [91] and microflow sensor [92]. To fabricate highly conductive Ag interconnects and vias, Bogush et al. [93] and Shacham-Diamand et al. [94] suggest to use a post electroless deposition process to comply with the highly contamination sensitive CMOS and bipolar fabrication environment.

In this chapter, a fabrication process is presented to obtain thick, highly dense, conductive, and structured Ag layers with a good adhesion to the SIP capillary sidewall. This deposition process is divided into its three main steps. First, the adhesion of the Ag layer on the SiO_2 surface of the capillary is improved by an intermediate polymeric-mercapto-silane (MPS) layer. This solved the experienced Ag electrode instability due to high capillary forces of a receding water meniscus. Second, the Ag layer is grown by multiple electroless depositions. This Ag layer is analyzed according to its composition, morphology, thickness and conductivity. Third, simultaneously to the deposition, the layer is also structured by limiting the filling with electroless solution to certain parts of the fluidic system, by means of microfluidic stopvalves. A sketch of the deposited and structured Ag layer is shown in Fig. 5.1.

5.1 Experimental

5.1.1 Intermediate polymeric-mercapto-silane layer

The intermediate MPS layer provides a strong adhesion between the SiO_2 surface and the Ag layer. It covalently bonds, at one side, with a silane-group to the hydroxyl terminated SiO_2 surface. The other side is preferably defined by either a mercapto or amino group to which Ag has a high affinity [95-97]. The classical approach to functionalize the surface with

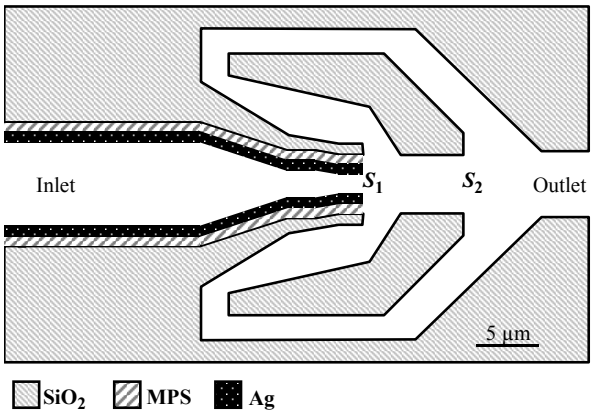

Fig. 5.1 Sketch (top view) of an electrolessly deposited Ag electrode. For an improved adhesion of the Ag layer to the SiO_2 surface an intermediate MPS layer was employed. Structuring of the Ag layer was performed with a microfluidic stopvalve at the position S_1 which controlled the filling of the capillary with electroless Ag deposition solution.

a MPS layer is to dip the sample in a solution containing the monomeric silane, diluted in methanol or toluene [95-102]. This process has an inherent problem: Most of the available silanes have two or three methoxy/ethoxy functional endgroups. These endgroups tend to form polymeric globuly, which also bond to the surface or remain inside the capillary after drying. To complicate matters further, this polymerization is in addition catalytically enhanced by the water layer covering the SiO_2 surface. The polymerization of the silane can be reduced by heating the SiO_2 surface and using dry toluene [103, 104]. Nevertheless, the removal of liquid silane solution is critical, especially in the case of the microcapillaries, and no satisfying solution could be found. In order to avoid these problems two measures are proposed in literature: The water layer on the SiO_2 was removed prior the silanization, and gas phase silanization was used [105-107]. For the capillaries, a satisfactory surface functionalization and a removal of the excessive gaseous silane could be achieved by:

1. Dehydrating the capillary surface and the reaction container by baking and venting it at 180° C for 20 min.
2. The MPS layer was formed by evaporating 50 µl of 3-mercaptopropyldimethoxymethyl silane in a volume of 30 ml at 180° C for 10 min.
3. The excessive silane was removed by venting the reaction container while continuously heating for additional 10 min.

5.1.2 Electroless Ag deposition

Ag startlayer deposition

A startlayer or seedlayer was necessary to provide a preferred point for the reduction of Ag^+ ions by a catalyst, from either a different material like tin(II) [89, 95], or already Ag itself [108-110]. Sensitizing with tin(II) was avoided, because it would require an additional filling step and this would have represented an additional source of contamination inside the microcapillary. The startlayer was formed by a two-step reduction deposition, as suggested by Schneider et al. [108]. In their approach, a strong reducing agent, borohydride, formed small Ag particles, which were then further enlarged. In order to control the reaction of the startlayer deposition, sodium hyphophosphite (NaH_2PO_2) was chosen which had a slightly weaker reducing strength than borohydride. Moreover, NaH_2PO_2 is also known as a reducing agent for electroless nickel plating [111, 112].

The electroless deposition of the startlayer was based on the solution described in the following section with the additional reducing agent NaH_2PO_2 at a concentration of 1 $mol \cdot l^{-1}$. It was performed by filling the capillaries with the electroless deposition solution, sealing them to avoid evaporation and keeping them in an oven at 65° C for 20 min. Afterwards, the capillary was rinsed with deionized water and blown dry.

Multiple Ag layer deposition

The major requirement of electroless deposition of the Ag layer in a batch-like process implies that an homogeneous and sufficiently thick layer has to be grown out of the minute available volume of the capillary above the layer. In order to increase the layer thickness and, hence, its conductivity, multiple deposition steps are necessary, which inherently increases the risk of clogging. To reduce the amount of depositions steps, a high concentration of electroless deposition solution is necessary, while the reaction must be kept controllable and reproducible. For this purpose, the Tollens reaction, also known as the silver mirror reaction is implied [85-88]. The composition of the electroless Ag deposition solution consisted of:

1. The Ag^+ ions in the form of 1 $mol \cdot l^{-1}$ silver nitrate, which was transferred into silver diamine by ammonium hydroxide 2 $mol \cdot l^{-1}$. The transfer from silver nitrate into silver diamine was necessary to avoid precipitation of silver oxide at high pH values (pH > 10). From the solid solution diagram of the system, silver oxide / ammonium hydroxide / water, a concentration of 2 $mol \cdot l^{-1}$ ammonium hydroxide was used to dissolve all possible silver oxide [113].
2. The reducing agent was 0.1 $mol \cdot l^{-1}$ glucose. As reducing agents for the Tollens reaction, glucose and hydrazine are commonly employed. Nevertheless, for this experimental study, glucose is used, because it is less toxic and safer to handle. In addition, glucose had a weaker reducing strength than NaH_2PO_2.
3. The reaction should preferably occur at the already existing Ag layer attached to the sidewall and not inside the bulk solution [114]. This can be achieved by controlling the reaction speed, which at these high concentrations could be achieved by adding 0.2 $g \cdot l^{-1}$ trisodium citrate as a complexing agent [115] and 0.01 $mol \cdot l^{-1}$ sodium hydroxide (NaOH) to the solution. The reaction kinetics were adjusted such that Ag^+ is slowly reduced and has enough time to adhere to the surface.
4. As a wetting agent, ethanol was added to a concentration of 20% vol. This was necessary, since the silanization transformed the former hydrophilic surface into a hydrophobic one. The use of surfactants was avoided, for this purpose, because of their interaction with the Ag^+ reduction and the competing adhesion interaction with the Ag at the MPS layer. In addition, ethanol did not poison the electroless deposition solution, since it is also known to be employed as a reducing agent in the Tollens reaction [116].

Similarly to the Ag startlayer, the deposition was performed by filling the capillaries with electroless solution and sealing them. The deposition took place during 20 min. at 65° C. To finish, the capillaries were rinsed with deionized water and blown dry.

5.1.3 Configuration of the Ag electrode by microfluidic structures

The requirements on the microfluidic structure are: to limit the filling of the capillary with electroless Ag deposition solution to the desired areas, and then, after the electrode fabrication, to still allow a complete and void free filling of the entire system. This can be achieved with so called microfluidic stopvalves, an example of which is shown in Fig. 5.1. The operational principle is based on an abrupt increase in the capillary's cross section at the

point S_1, which enforces a flattening, followed by bulging of the liquid's meniscus and, hence, induces an opposing burst pressure relative to the meniscus' Young-Laplace pressure [117-122]. For operating fluidic device later, it is important to overcome this stopvalve after the electroless Ag deposition and to achieve a void free filling of the remaining fluidic system. This switching from stopping to transmitting the solution should be done without applying any external pressure. The method chosen is to rather change the surface tension of the solution during the initial filling. This can be achieved for instance by changing the composition of the solution. The void free filling is explained according to Fig. 5.1, where the solution with a lower surface tension overcomes the burstpressure at the lip in S_1. Within the microfluidic stopvalve, the flow in the center capillary is decelerated by another sudden opening in the cross section S_2, until the side branches are completely filled. A complete filling of the side branches triggers the final filling of the complete stopvalve and the meniscus proceeds further within the capillary.

The model of the microfluidic stopvalve needs to take the limitations of the fabrication process into account. The capillaries and microfluidic stopvalve were outlined with only one lithography, etching and thermal oxidation step. This limited the design to only a two dimensional cross sectional change in the width. Previously, Man et al. [117] developed a two dimensional model, which described a sudden opening with sharp corners at a high aspect ratio. These, well defined, sharp corners can be achieved for capillaries in the range of 100 µm in diameter. However, rounding of the corners becomes critical for the investigated capillary having dimensions of less than 5 µm. Here, the corner radius is comparable to the opening width. In addition, the aspect ratio of the stop valve is not very high, hence, a three dimensional model is required, where the meniscus of the liquid-air interface stretches out over the complete capillary cross section. This over constrains the system and, therefore, a definition of the Young-Laplace pressure with only one unique radius is not possible. Therefore, two individual Young-Laplace pressures in the center of the width p_w and the height p_h were derived which were, afterwards, assembled to the total Young-Laplace pressure p_t inside the stopvalve. The stopping and filling of the microfluidic stopvalve is controlled by carefully balancing the hydrophobic Young-Laplace pressure p_w of the opening in the width with the hydrophilic Young-Laplace pressure p_h of the capillary's constant height.

The geometry for the opening in the width was modelled, as shown in Fig. 5.2. The capillary is filled from the left side with the solution and the meniscus at the liquid-air interface is curved with the radius R. The radius R is defined by the capillary width at the meniscus position, which itself can be described by the initial width w_0, the corner radius R_c and the opening angle κ. In the center of the corner radius, the opening angle κ spans from the normal of the capillary sidewall to the straight line to the meniscus contact point at the

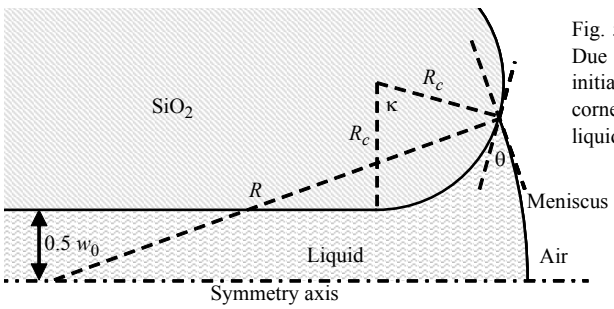

Fig. 5.2 Sketch of the microfluidic stopvalve. Due to the fabrication, the capillary with an initial width w_0 opens at the lip with a rounded corner with the radius R_c. The meniscus of the liquid-air interface is bent with the radius R.

rounded corner. This leads to the definition of the Young-Laplace pressure p_w of the width as

$$p_w = \frac{\gamma_{la}}{R} = -\gamma_{la}\frac{2\cos(\kappa+\theta)}{w_0 + 2R_c(1-\cos\kappa)}, \tag{5.1}$$

where γ_{la} and θ represent the liquid-air surface tension and the contact angle, respectively. The pressure p_w for an initial width $w_0 = 1$ µm, a corner radius $R_c = 1$ µm, at different contact angles θ is shown as a function of the opening angle κ in Fig. 5.3 a). The transition from hydrophilic filling to hydrophobic stopping can be determined by a change in sign of p_w at $\gamma = \pi / 2 - \theta$. For the microfluidic stopvalve, it can be seen, that the higher the contact angle θ, the more hydrophobic the pressure p_w and the earlier the transition to hydrophobic behavior with respect to the opening angle κ. The influence of the corner rounding is shown in Fig. 5.3 b) in a parametric form by $r_w = 2\ R_c / w_0$. In case of a negligible corner radius R_c and an opening angle κ of 180°, the hydrophobic pressure p_w equals the Young-Laplace pressure of a spherical droplet, with a diameter equal to the width of the capillary. With increasing corner radius R_c, the maximum hydrophobic pressure decreases, since the actual width at the maximum hydrophobic pressure is larger than the initial width w_0. Furthermore, the lower the contact angle θ, the more influential becomes the corner rounding, because the maximum hydrophobic pressure is reached at a higher opening angles κ.

The second, hydrophilic Young-Laplace pressure p_h of the constant capillary height h can be calculated to

$$p_h = \gamma_{la}\frac{2\cos\theta}{h}. \tag{5.2}$$

In order to get a good approximation of the total Young-Laplace pressure p_t at the microfluidic stopvalve, both the hydrophobic pressure p_w and the hydrophilic pressure p_h is weighted by its fraction of the wetted perimeter. The total Young-Laplace pressure p_t yields in

$$p_t = \frac{\gamma_{la}}{h + w_0 + 2R_c(1-\cos\kappa)}\{hp_w - [w_0 + 2R_c(1-\cos\kappa)]p_h\}. \tag{5.3}$$

(5.4)

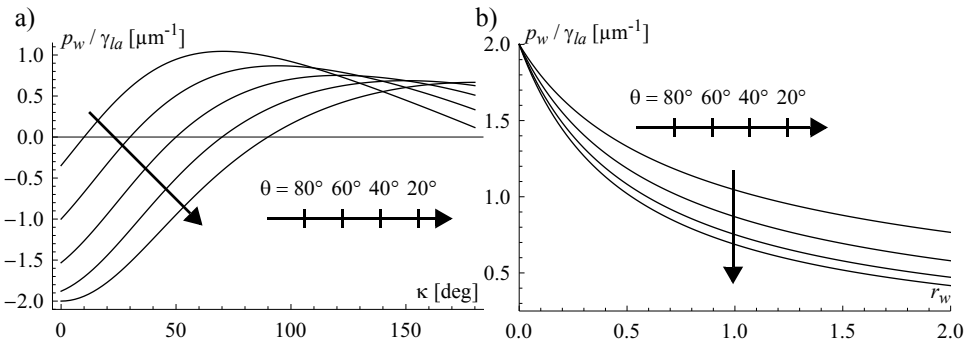

Fig. 5.3 a) Young-Laplace pressure p_w induced by the width of the microfluidic stopvalve as a function of the opening angle κ at an initial width w_0 of 1 µm and a constant rounding of the opening R_c of 1 µm. b) Maximum Young-Laplace pressure induced by the width as a function of the ratio r_w between initial width w_0 and the corner rounding R_c.

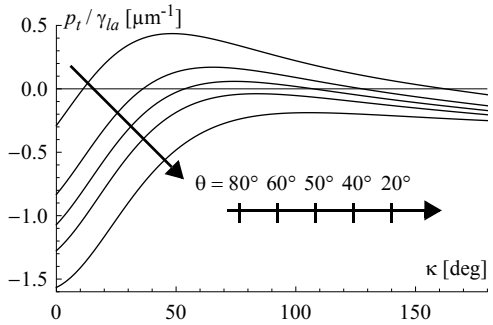

Fig. 5.4 Combined Young-Laplace pressure p_t as a function of the opening angle κ at an initial width w_0 of 1 μm, a rounded corner R_c of 1 μm and a capillary height h = 3μm. The microfluidic stopvalve is able to block solutions once p_t becomes positive. Hence, the stopvalve is designed such that the maximum opening angle κ stops solutions for a high contact angle θ and transmits solutions for a low contact angle θ.

The sign of p_t is defined as such that a negative pressure p_t results in a continuous capillary filling. The capillary filling is stopped as soon as the pressure p_t becomes positive. In this model, the influence of the corners between the capillary top / bottom and sidewall on the meniscus shape is neglected. The switching behavior of the microfluidic stopvalve can be seen in Fig. 5.4 showing the total Young-Laplace pressure p_t for a capillary height h = 3 μm, an initial width w_0 = 1 μm and R_c = 1 μm as a function of the opening angle κ. For contact angles θ below 45° the liquid is not stopped for opening angles κ up to 180° by the microfluidic stopvalve and the capillary is continuously filled. Whereas for contact angles θ larger than 45° the total Young-Laplace pressure p_t becomes positive, hence, the liquid is stopped, for sufficiently high opening angle κ.

5.2 Process characterization, results and discussion

The electroless Ag deposition process described in this chapter is intended for the microfabricated SIP. Nevertheless, the process was initially studied on commercial μ-capillaries[1] and larger microfabricated capillaries in order to study the influence of the solution's composition. These μ-capillaries were available in larger quantities and they were also easier to access for the electrical and topographical measurements. Prior to the deposition of the MPS layer, both capillaries, the SIP and the μ-capillary, were cleaned in an oxygen plasma for 20 min. in order to remove any organic residues deposited during storage, and to activate the SiO_2 surface. All solutions were prepared from analytical grade chemicals[2] and diluted in deionized water[3] with a specific resistance of 18 MΩ·cm.

5.2.1 Intermediate polymeric-mercapto-silane layer

A successful homogeneous silanization can be concluded from two observations: During the filling experiments, no considerable changes in contact angle θ were detected throughout the capillary. Moreover, a stable Ag layer throughout the MPS coated capillary was achieved. For the actuation of the microfluidic stopvalve, the solution's contact angle θ on the MPS coated capillary surface was investigated. In detail, a MPS coated SiO_2 capillary, 20 μm wide and 50 μm deep, was filled with a varying binary solution of water and ethanol. The capillary was designed in such a way that the solution entrapped an air bubble at a dead end. The contact angle θ was determined by measuring the radius of the meniscus of the air bubble. Fig. 5.5 a) shows the contact angle θ as a function of the volumetric ethanol content,

1. Hirschmann, μ-capillary, 10 μl and 25 μl
2. Sigma Aldrich, The Netherlands
3. Purelab UHQ

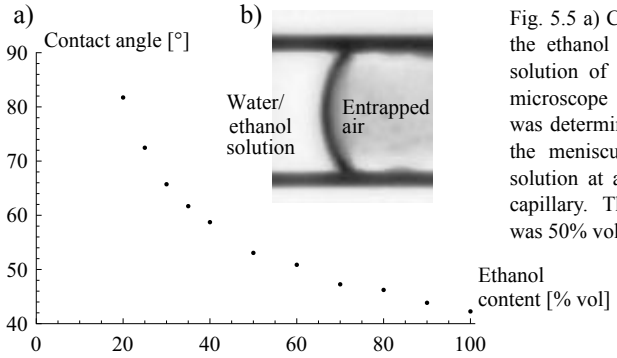

Fig. 5.5 a) Contact angle θ as a function of the ethanol volume content in the binary solution of water and ethanol. b) Optical microscope image of the contact angle θ was determined by measuring the radius of the meniscus between the water ethanol solution at an entrapped air bubble in the capillary. The employed ethanol content was 50% vol.

deduced from microscope images like the one shown in Fig. 5.5 b). It can be seen, that the higher the ethanol content, the lower the contact angle θ. At ethanol contents lower than 20% vol., the detection of the meniscus radius became more unreliable since the curvature became less distinctive. From this measurement, it was concluded that the capillary can be reliably filled with an ethanol content of 20% vol. and, hence, this concentration was used in the electroless Ag deposition.

5.2.2 Electroless Ag deposition

Composition of the startlayer

The need of a startlayer inside microfabricated SIP capillary with a cross section of 3 µm × 3 µm is motivated in Fig. 5.6. When starting directly with the proper electroless Ag deposition solution, the Ag layer deposited as a grainy reflective layer from the macroscopic inlet into the microscopic capillary. In most cases, the thickness of the Ag deposition gradually diminished to zero within 100 µm to 200 µm from the inlet into the capillary. The purity of the deposited Ag startlayer inside the SIP capillary was concluded by cutting it open with a focussed ion beam (FIB) and subsequently performing an energy dispersive X-ray (EDX) spectroscopy. The EDX spectroscopy result is shown in Fig. 5.7 a) and it clearly indicated a deposition of pure Ag on a SiO_2 substrate, where the traces of gallium (Ga) were remaining from the FIB cutting.

The usage of NaH_2PO_2 was limited to the startlayer deposition since the density of the deposited layer was less than the Ag layer deposited in the subsequent electroless depositions. The better demonstrate the influence of NaH_2PO_2 on the deposited Ag layer density an electroless Ag deposition was performed with 1 mol·l^{-1} NaH_2PO_2 as the only reducing agent

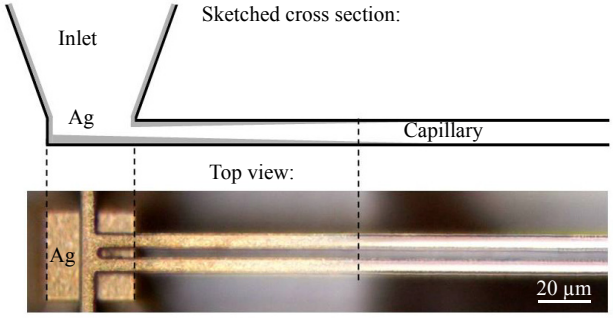

Fig. 5.6 Sketch and optical microscope image of an electroless Ag deposition without a startlayer. The Ag layer thickness diminished within 100 µm - 200 µm from the macroscopic inlet into the microscopic capillary (3 µm × 3 µm). This could be avoided by using a startlayer before the proper electroless Ag deposition.

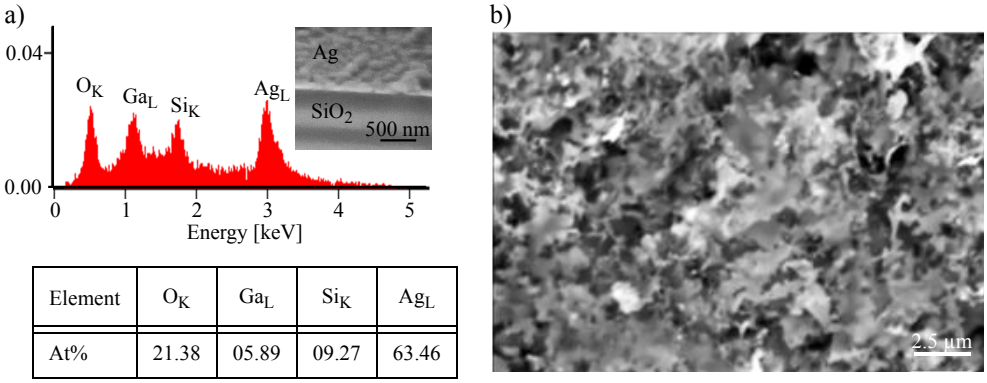

Element	O_K	Ga_L	Si_K	Ag_L
At%	21.38	05.89	09.27	63.46

Fig. 5.7 a) EDX spectrum of an Ag startlayer deposited into a SiO_2 capillary (3 µm × 3 µm). The spectroscopy result revealed a pure Ag layer on a SiO_2 substrate. The inset shows an SEM image where the EDX spectrum was performed. b) SEM image showing the influence of NaH_2PO_2 on the electroless deposited Ag layer. Using only NaH_2PO_2 as a reducing agent for the electroless deposition resulted in a sponge like porous layer.

and amplified by using a higher concentration of 0.05 mol·l^{-1} NaOH. The porosity of the sponge like Ag layer, can clearly be seen in the scanning electron microscope (SEM) image, shown in Fig. 5.7 b). This could be explained by the hydrogen evolution during the oxidation of $H_2PO_2^-$ [112].

Reaction kinetics

In order to verify the adjustment of the reaction speed by the concentration of trisodium citrate and NaOH the following experiments were conducted. Electroless Ag depositions with varying concentrations were performed for 20 min. at 65° C, in a MPS coated µ-capillary with a radius of 300 µm. Afterwards, the capillaries were rinsed and the ends were removed to a total length of 2 cm. Since the reaction was not finished at these large cross sections after 20 min., the reaction speed could be determined by the conductivity σ of the Ag layer. Fig. 5.8 a) shows the conductivity σ per cm at different time steps for a concentration of 0.2 g·l^{-1} trisodium citrate and 0.01 mol·l^{-1} NaOH. A saturation after 20 min. of reaction could not be detected, therefore, the reaction can be linearly fitted to 0.09 S·cm^{-1}·min.$^{-1}$. The conductivity σ of the deposited Ag layer as a function of the trisodium citrate concentration, at 0.01 mol·l^{-1} NaOH, is shown in Fig. 5.8 b). It can be clearly seen that the trisodium citrate had a strong influence on the reaction speed. At a concentration of more than 0.4 g·l^{-1} (equals a

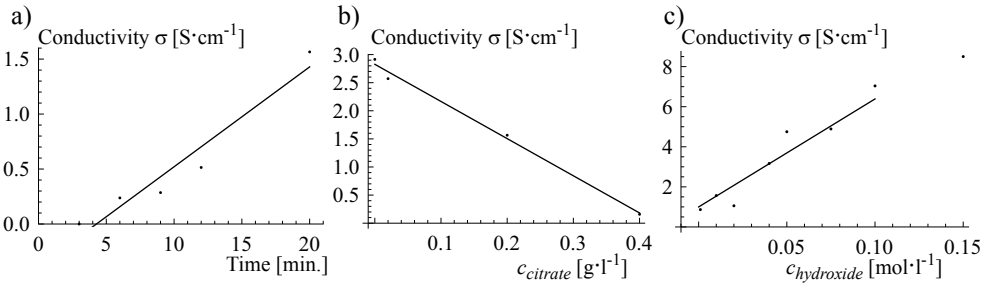

Fig. 5.8 Measurement of the conductivity σ of an Ag layer electrolessly deposited into a 300 µm µ-capillary. a) For the standard solution composition the reaction is not completed after 20 min. b) The reaction speed can be reduced by increasing the sodium citrate concentration. c) The reaction speed can be increased by increasing the NaOH concentration. The saturation at 0.15 mol·l^{-1} NaOH was the result of a nearly complete transfer of the Ag ions within the 20 min. time frame.

concentration of 1.5 mmol·l^{-1}), no conductive Ag layer was deposited after 20 min. The conductivity σ depended linearly on the trisodium citrate concentration $c_{citrate}$ as -6.6 S·l·cm^{-1}·g^{-1} $c_{citrate}$. The reaction deceleration could be explained by the observations of Pillai et al. [115], who used trisodium citrate as a complexing and stabilizing agent. The conductivity σ as a function of the NaOH concentration, at 0.2 g·l^{-1} trisodium citrate, is shown in Fig. 5.8 c). For NaOH concentrations up to 0.1 mol·l^{-1} the conductivity σ increased linearly. The conductivity σ could be linearly fitted on the NaOH concentration $c_{hydroxide}$ as 54 S·l·cm^{-1}·mol^{-1} $c_{hydroxide}$. For higher NaOH concentrations the conductivity σ slowly saturated. This could be explained by a complete reaction of the Ag out of the solution within 20 min. Furthermore, the reaction speed also saturated due to the Nernst equation, which predicts a logarithmic dependence of the reaction speed on the NaOH concentration. To summarize, an electroless Ag solution containing a concentration of 0.2 g·l^{-1} trisodium citrate and 0.01 mol·l^{-1} NaOH in a capillary provides enough time to properly fill a capillary with radius of 300 µm, and is fast enough for a reasonable deposition time.

Morphology, thickness and conductivity of multiple deposited Ag layers

In order to sufficiently increase the Ag layer thickness, multiple electroless depositions were conducted. The experiments presented in this section were performed on µ-capillaries with a radius of 520 µm. First, the µ-capillaries were MPS coated, then a startlayer and subsequent multiple layers of Ag were deposited. Finally, the µ-capillaries were cleaned with deionized water and the ends were removed to a total length of 2 cm in order to only investigate the deposition inside the µ-capillary. In Fig. 5.9, the morphology of the startlayer (a) and one subsequent Ag layer (b) was investigated with a scanning force microscope (SFM). The average surface roughness was determined to be 15 nm in both cases. The grain diameter increased from 96 nm ± 27 nm for the startlayer to 124 nm ± 28 nm for the subsequent Ag layer, which was expected since the deposition of the startlayer was performed with a stronger reducing agent. In addition, the grain diameter of the deposited subsequent Ag layer was in the same range, as reported by Saito et al. [87].

The thickness of the deposited Ag layer was measured by partially mechanically removing the Ag layer from the glass substrate, and taking a scanning force microscopy image across the step, as shown in Fig. 5.10 a). From the histogram of the scanning force microscopy image, see Fig. 5.10 b), the Ag layer thickness could be measured. The thickness was revealed by the height difference between the broad peak, indicating the rough Ag layer,

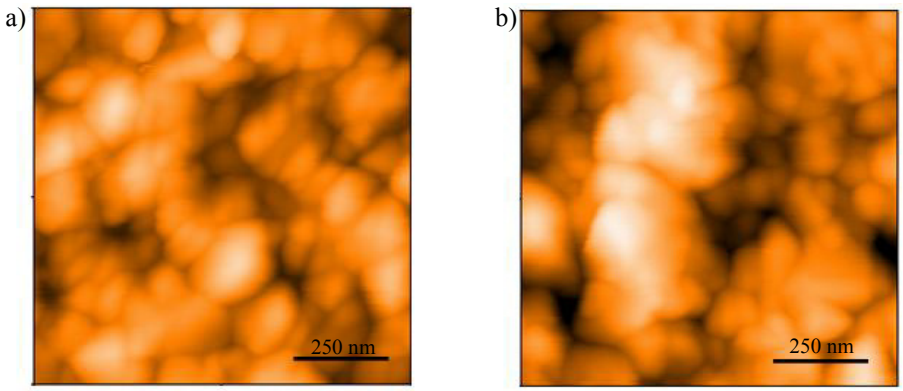

Fig. 5.9 Scanning force microscopy images (z-scale 105 nm) of: a) an electroless Ag deposited startlayer. The average grain size diameter is 96 nm ± 27 nm. b) An additional electroless Ag deposited layer on top of the start-layer. The average grain size diameter is 124 nm ± 28 nm.

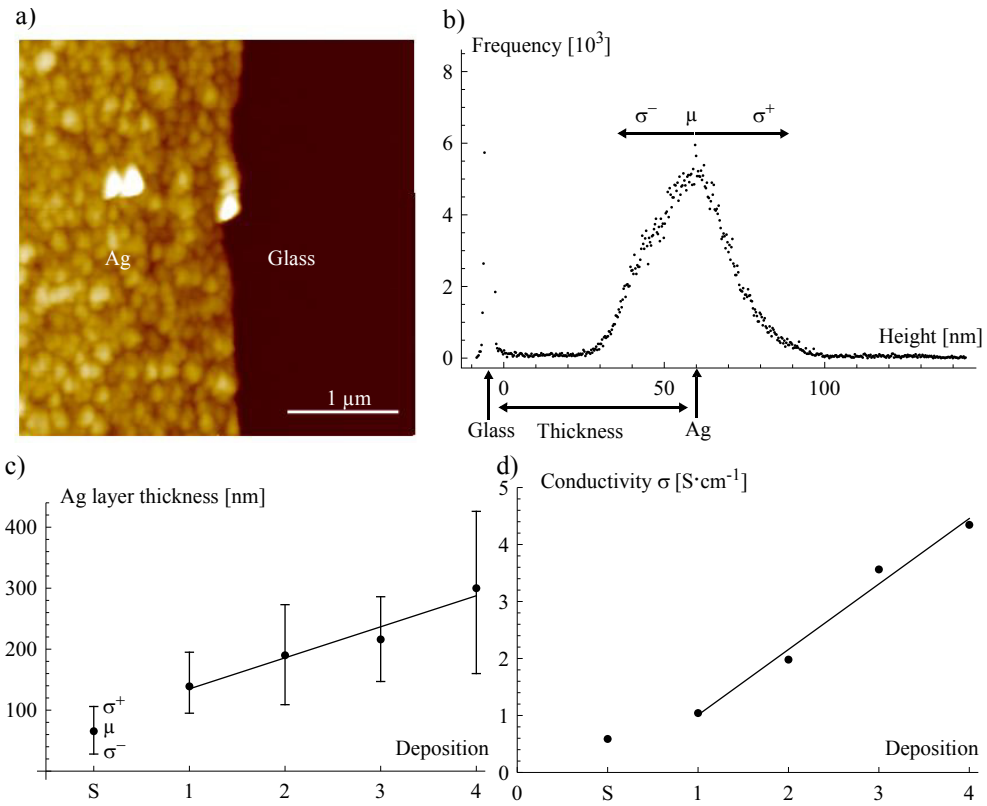

Fig. 5.10 a) The electrolessly deposited Ag startlayer was partially removed and a scanning force microscopy image was taken over the step (z-range 150 nm). b) Histogram of the scanning force microscopy image revealing the thickness of the startlayer as 65 nm. Thickness and conductivity σ of the startlayer (S) and multiple electroless Ag deposited layers (1 - 4). c) The Ag layer thickness linearly increased by 51 nm per deposition. d) The conductivity σ increased by 1.1 S·cm^{-1} per deposition.

and the sharp peak, indicating the smooth glass surface. The thickness of the startlayer was determined to 65 nm and each subsequent Ag layer increased the thickness linearly, by about 51 nm, as shown in Fig. 5.10 c). The conductivity of the startlayer was measured to 0.6 S·cm^{-1}, and it increased linearly for each subsequent Ag deposition to 1.1 S·cm^{-1}, as shown in Fig. 5.9 d). Combining the thickness with the conductivity yields the specific conductivity of the Ag layers as 3×10^7 S·m^{-1} for the startlayer and 6×10^7 S·m^{-1} for the subsequent Ag layers. Comparing these values with the one of the specific conductivity of bulk Ag (6.1×10^7 S·m^{-1} [123]) indicated that the Ag layer was very pure. In order to reach this high conductivity value, the layer must also be very dense. Moreover, the difference in specific conductivity between the startlayer and the subsequent Ag layers support the formation of a less dense startlayer induced by the NaH_2PO_2.

5.2.3 Microfluidic structuring of the Ag layer

The microfluidic stopvalve fabrication required to achieve the lowest corner rounding R_c, the highest opening angle κ and the smallest width w_0 of the microfluidic stopvalve. Especially, the lowest corner rounding was challenging. First, the lithography used to outline the microfluidic stopvalve, required a minimum sidewall width of 1 µm to avoid retraction of

the photoresist. The subsequent deep reactive ion etching (DRIE) rounded the corners with a radius of 450 nm, as shown in Fig. 5.11 a) upper image. Finally, the thermal oxidation further increased the corner rounding to about R_c = 1 µm, due to the growth of SiO_2 out of the Si. The fully fabricated microfluidic stopvalve is presented in Fig. 5.11 a) lower image. The stopvalve geometry was measured to an opening angle κ = 160°, with an initial width of the microfluidic stopvalve of w_0 = 1 µm. The height of the microfluidic stopvalve was not specifically measured, but was expected to be in the range of h = 3 µm.

The microfluidic properties of the stopvalve were tested. A successful stop of a 20% vol. ethanol solution is shown in Fig. 5.11 b). A stop of the solution is in good agreement with the previously developed model, taking the contact angle θ = 82° of a 20% vol. ethanol solution measured in Fig. 5.5. A void free filling of the microfluidic stopvalve is shown in Fig. 5.11 c). This was already achieved with a 40% vol. ethanol solution, corresponding to a contact angle of θ = 58°. According to the developed model, the transition to transmitting the solution should occur at a lower contact angle of θ = 45°. However, this model neglected the influence of corners between the top and the sidewall, as well as between the bottom and the sidewall, see also Fig. 2.6 b) of the capillary cross section. In these 90° corners, a sword-like meniscus is shaped [124, 125], which reduces the total Young-Laplace pressure p_t. This effect can be integrated into the model by a reduced effective height. In the presented case this results in a maximum effective height of 2.65 µm. Finally, the structuring of an Ag layer with two opposing microfluidic stopvalves is shown in Fig. 5.11 d). The Ag layer can be seen as the grainy reflective layer, up to the microfluidic stopvalves. The two electrodes are separated by a uncoated hollow capillary.

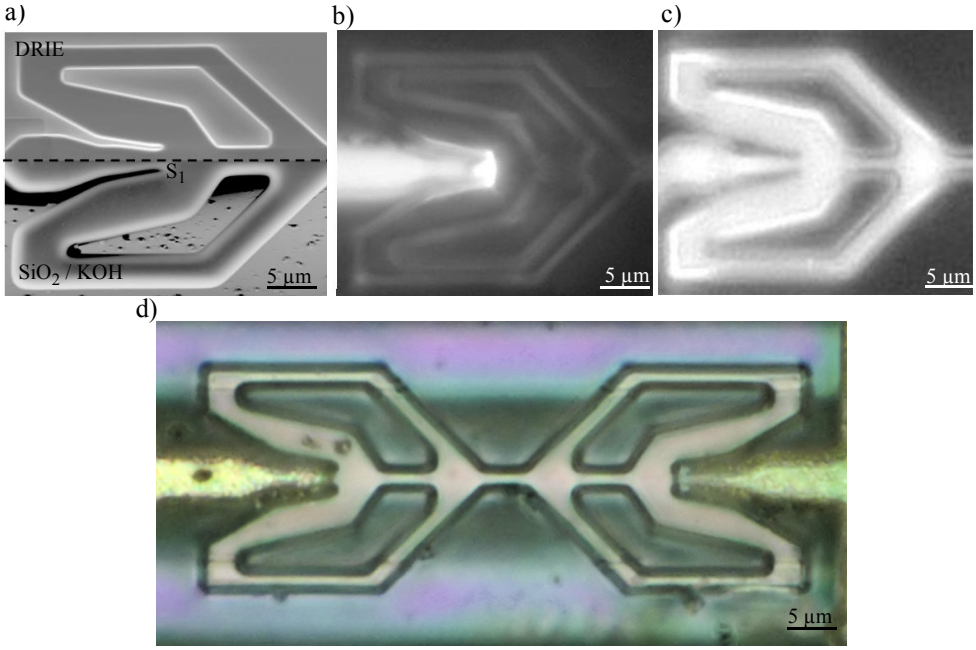

Fig. 5.11 a) The upper part shows a SEM image of the microfluidic stopvalve after DRIE. The lower image, after thermal oxidation and KOH release, the fully fabricated microfluidic stopvalve had in its stop S_1: a width of w_0 = 1 µm, an opening angle κ of 160° and a corner rounding with a radius of R_c = 1 µm. Fluorescence microscope image of a microfluidic stopvalve b) successfully stopping a 20% vol. ethanol solution and c) void free filling with a 40% vol. ethanol solution. d) Optical microscope image of an Ag layer electroless deposited and structured by two opposing microfluidic stopvalves. The Ag layer can be seen as the grainy reflective layer on the left and right, separated by a non coated hollow capillary.

5.3 Summary and conclusions

The strategy presented to deposit and structure Ag layers into closed capillaries with a cross section down to 3 µm × 3 µm was the following: For an improved adhesion on the SiO_2 surface an intermediate MPS layer was deposited. An Ag startlayer was deposited to homogeneously create reaction sites throughout the capillary. The thickness of the Ag startlayer was increased by multiple electroless depositions. The resulting Ag layer was very dense and highly conductive (specific conductivity $6 \times 10^7\ \Omega^{-1}\cdot m^{-1}$). Simultaneously to the Ag deposition, the layer was structured by controlling the filling of the capillaries with microfluidic stopvalves.

During the experiments, it turned out that the electroless Ag deposition is highly contamination sensitive. In the investigated cross sections of 3 µm × 3 µm already small surface contamination polluted the minute amount of liquid inside the capillary. For instance, a concentration of already 1.5 $mmol\cdot l^{-1}$ sodium citrate inhibited the reaction. This concentration amounts to a surface contamination of only 1 $\mu mol\cdot m^{-2}$. In order to successfully and reliably deposit Ag layers in large numbers of microfluidic devices or in even smaller capillary cross sections, a way to obtain ultra clean capillaries must be found.

Chapter 6

Electroosmotic pumping and electrochemical sensing with Ag/AgCl electrodes

Up to this point, liquid-gas separators for the ventilation of the emerging electrolyzed gases during electroosmotic (EO) pumping were required with platinum electrodes, as described in chapter 4. Electrodes like silver/silver chloride (Ag/AgCl) have the outstanding advantage that, during pumping the electrochemical reaction transforms Ag into AgCl and vice versa, rather than creating gasbubbles by electrolyzing the liquid. Taking the process of electroless Ag deposition, as described in the previous chapter, and further partially transforming the Ag layer into AgCl, allows the fabrication of Ag/AgCl electrodes. Ag/AgCl electrodes are the most common and well understood electrodes for biological and chemical measurements [126]. In order to improve electrochemical measurements in microfluidic systems, Suzuki et al. [127] already integrated Ag/AgCl electrodes by sputtering and subsequent electroless transformation. The integration of Ag/AgCl electrodes into the scanning ion pipette (SIP) would be an important step towards a scanning microfluidic electrochemical sensor. This chapter presents the design, fabrication and experimental analysis of Ag/AgCl electrodes for EO pumping and electrochemical sensing.

6.1 Design

The layout of this design was chosen to obtain a better understanding of the electroless Ag deposition and subsequent transformation process into AgCl as well as the performance of the Ag/AgCl electrodes for EO pumping. Hence, a relatively large, larger than the for the final SIP application, capillary cross section was chosen to increase the reproducibility of the electrode fabrication. By this, the risk of clogging was reduced and the accessibility to measure the conductance and the topography was facilitated. The capillaries hydraulic dimension of about 75 μm was chosen, according to an previously developed SU8 fabrication process [128]. A sketch of the fluidic system's layout is shown in Fig. 6.1 a) and of the EO pump in Fig. 6.1 b). Based on previous experience with the platinum electrodes for EO pumping, it was known that easily accessible fluidic and electric connections are important. Therefore, the size of the fluidic connections was increased to be 5 mm × 5 mm square. In order to define the geometry of the electrodes during EO flow fabrication, microfluidic stopvalves were employed. To facilitate the fluidic and electrical connections, Cord End terminals were glued to the fluidic connections of the NOA63 cast. Cord end terminals are usually employed to mechanically protect the ends of electrical cables. Here, the metallic hollow shaft, 1 mm in diameter and 5 mm in height, allowed a more convenient connection.

The layout with the EO pump, embedded into the fluidic system, was translated into an equivalent electrical circuit, in order to model and evaluate the resulting flows and pressures. This is shown in Fig. 6.1 c). The conversion of the capillaries and the EO pump into electrical

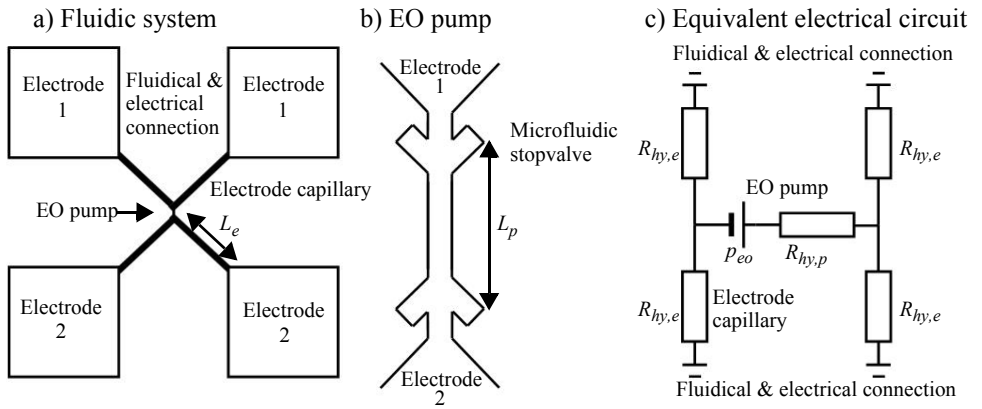

Fig. 6.1 a) Sketch of the fluidic system layout, including the fluidic and electrical connection. b) Sketch of the EO pump layout. The electrodes were structured by the microfluidic stopvalve. c) Equivalent electrical circuit of the fluidic system to determine the EO induced flow.

circuit elements was performed according to Morf et al. [129]. The hydraulic resistance $R_{hy,s}$ of the complete fluidic system can be calculated to be

$$R_{hy,s} = 2\frac{R_{hy,e}}{2} + R_{hy,p}, \tag{6.1}$$

where $R_{hy,e}$ and $R_{hy,p}$ denote the hydraulic resistance of the electrode and of the EO pump, respectively. Having a voltage U_{eo} over the EO pump leads to the characteristic flow Q_{eo}

$$Q_{eo} = U_{eo}\mu_{eo}\rho_{el}\frac{R_{hy,p}}{R_{hy,s}R_{el,p}}, \tag{6.2}$$

where μ_{eo}, ρ_{el}, $R_{el,p}$ denote the EO mobility, the specific electrical resistance of the solution and the electrical resistance of the pump, respectively. This defined the layout and a model of an EO pump embedded into a fluidic system.

6.2 Process flow

For the investigation presented here, a cheap, quick and easy processing was opted for. Within the framework of his master thesis, P.A. van der Ploeg intended to achieve this, by using a polymer based microfluidic chip fabrication. Polymer vacuum casting was used since it allowed to fabricate structures with high aspect ratio, satisfying resolution and repeatability [130-132]. Specifically, the fabrication of the fluidic system was based on the SU8-PDMS-NOA63 casting process, as suggested by Dupont et al. [133]. The idea was to take advantage of the high resist thickness and photolithographic structuring of SU8. To avoid bonding between SU8 and NOA63, an intermediate casting step in polydimethylsiloxane (PDMS) was necessary. The final cast was in NOA63, chosen due to its hydrophilic properties [134]. Despite the findings of Dupont et al. [133] that NOA63 exhibits high fluorescent auto-emission in the wavelength of fluorescein, the EO flow was determined with fluorescently labelled microspheres. To cope with this high fluorescent auto-emission, the NOA63 trenches were capped with microscope glass slides and the movement of the microspheres was observed through the glass. Due to this fabrication process, the micromachining of the microfluidic chip was reduced to only one lithography step, compared to the scanning ion pipette fabrication presented in chapter 2.

According to Polk et al. [137], one of the major drawbacks of integrating Ag/AgCl electrodes into microfluidic systems was the poor stability of the electrodes due to dissolution of the only a few nanometer thick AgCl layer. In addition, during the actuation the electrode is continuously transformed, hence, for a long actuation time a thick Ag/AgCl electrode is necessary. In order to fabricate the Ag/AgCl electrodes inside the NOA63/glass capillaries, an Ag deposition and a subsequent transformation into AgCl with an electroless solution was chosen. To sufficiently increase the electrode thickness, the electrodes were fabricated out of a flowing electroless solution [138, 139], instead of the previously used multiple depositions in Chapter 5. This had the additional advantage, that the concentration of the electroless solution could be kept constant throughout the capillary, as soon as the supply of reactants by a high flow rate exceeds the loss of reactants during the electroless reaction.

The fabrication process was divided into six steps, as shown in Fig. 6.2. **(a)** First, SU8 layer was spun on a dummy Si wafer and the positive master of the capillaries was outlined by photolithography. During photolithography, a UV-filter[1] was used, in order to reduce the commonly experienced t-topping of the SU8. **(b)** Secondly, The SU8 structure was casted into the negative PDMS master. **(c)** This PDMS master was casted into multiple NOA63 top-open trenches**. (d)** Then, the NOA63 trench was capped with standard microscope slide**. (e)** The Ag electrodes were deposited on the sidewalls of the capillary in an electroless flow deposition process and passively structured with microfluidic stopvalves. Further details are provided in the next paragraph. **(f)** Finally, the Ag electrodes were partially transformed into AgCl by pumping a 0.3 $mmol \cdot l^{-1}$ sodium hypochloride solution through the capillary for 15 s. The reaction was stopped by flushing for another 3 min. with deionized water. This transformation process was based on the oxidation of the Ag layer and an immediate precipitation of AgCl sticking to the electrode surface due to the presence of Cl^- ions.

The electroless Ag electrode deposition and structuring demands a more detailed explanation. For the Ag deposition, a Tollens solution was used, similar to the one in chapter 4. The solution consisted of 0.1 $mol \cdot l^{-1}$ silver nitrate, 1 $mol \cdot l^{-1}$ ammonium hydroxide, 0.1 $mol \cdot l^{-1}$ glucose and 0.55 $mol \cdot l^{-1}$ sodium hydroxide. In this case, no sodium citrate was used, since the reaction speed was decreased by setting the reaction temperature to 20° C. Furthermore, neither the NOA63 nor glass surface needed to be silanized. At these cross sections, the adhesion of Ag to the surface was sufficient to create a stable electrode.

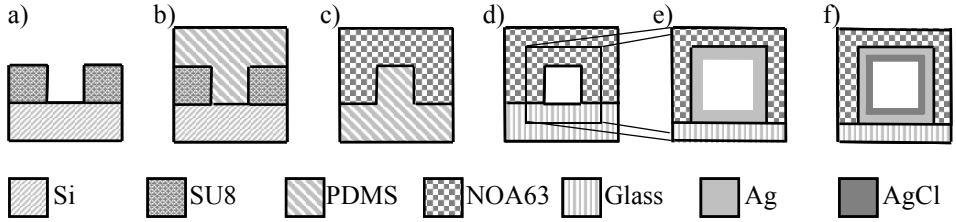

Fig. 6.2 The flow chart of the fabrication process. **a)** The SU8 layer was patterned by photolithography. In order to reduce t-topping of the SU8 a UV-filter was used. **b)** The SU8 structure was casted into the PDMS master. In order to increase the casting resolution, the cast with the liquid PDMS was placed in vacuum, 1 mbar, before curing. **c)** This PDMS master was then further vacuum casted into multiple NOA63 top-open trenches. **d)** The NOA63 trench was capped with standard microscope slide. **e)** The Ag electrodes were deposited on the sidewalls of the capillary in an electroless flow deposition process. The Ag electrodes were passively structured with microfluidic stopvalves. **f)** The Ag layer was further electrolessly chlorinated with flowing sodium hypochloride through the capillaries.

1. Omega, Pl-360-Pt

Therefore, it was not required to increase the solution's wetting properties with ethanol. For the flow deposition, the solution was freshly prepared before each deposition and stored in a reservoir at 3° C to suppress the reaction. From there, the solution was pumped with 200 $nl \cdot s^{-1}$ through silicone tubing (length 10 cm, interior diameter 0.5 mm and a sidewall thickness of 1 mm) to the chip. With this flow rate, the solution remained about 15 s inside the tubing, before it reached the chip. The temperature and, hence, the deposition rate was expected to be constant throughout the chip, since the solution was flushed through the chip within 1 s. The electroless Ag deposition was monitored by measuring the conductance of the electrode between the Cord End terminals, which were placed as fluidic and electric connections to the chip. The Ag deposition was stopped by flushing with deionized water for 3 min. once a conductance of 0.2 S was reached.

6.3 Fabrication results and discussion

The results presented here focus on the geometry of the fabricated capillaries, which is needed to verify the model for the EO flow section. During the flow fabrication, a detailed analysis was taken of the electroless Ag deposition and AgCl transformation rate. This was done by monitoring the conductance of the electrode between the two respective Cord End terminals.

6.3.1 Microfluidic NOA63/glass capillary

The PDMS master was obtained by gently pulling it off from the SU8 layer. The SU8 layer remained unharmed, since the mechanical bond-strength between PDMS and SU8 was relatively weak. The cross section of the PDMS negative of the EO pump is shown in Fig. 6.3 a). The dimensions of this negative stamp were measured to be 73 µm × 77 µm (height × width). The sidewall was slightly tapered from vertical by 1° reducing the width on the top, and a small spout of 4 µm was observed, where the PDMS crept in the gap between SU8 and the wafer.

The NOA63 cast was obtained by again gently pulling it of the PDMS master. In this case, the mechanical bond-strength between NOA63 and PDMS was weak as well. Fig. 6.3 b) shows the trench of the EO pump in the NOA63 cast. Its dimensions were reduced compared to the PDMS master and measured 55 µm × 67 µm (height × width). This shrinkage of UV curable polymers was known, for instance the UV curable SU8 has a volume shrinkage of about 7.5% [142]. The taper angle of the sidewall remained at about 1° and also a spout

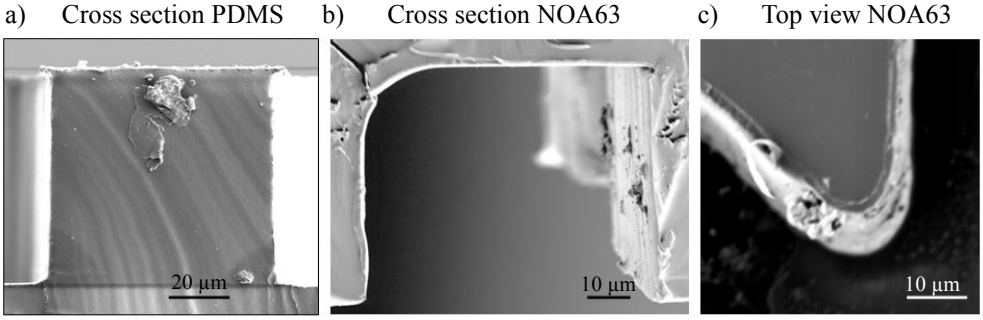

Fig. 6.3 Scanning electron microscope (SEM) images of the fabrication results. a) Cross section of the EO pump capillary, PDMS cast of SU8 structure. b) Cross section of the EO pump capillary, NOA63 cast of PDMS structure. c) Top view of a rounded corner of the microfluidic stopvalve in the NOA63 cast.

remained with a length of 2 µm. Fig. 6.3 c) shows the corner rounding of the NOA63 cast of the microfluidic stopvalve, which is important for the fluidic stopping and transmitting properties of the stopvalve. The dimensions of the electrode capillaries and the EO pump, as well as the microfluidic stopvalve in the NOA63 cast are summarized in Table 6.1.

Tabel 6.1: Dimensions fluidic system

Electrode capillary	Width, w_e	395 µm	Height, h_e	65 µm	Length, L_e	3.5 mm
EO pump	Width, w_p	65 µm	Height, h_p	55 µm	Length, L_p	600 µm
Microfluidic stopvalve	Width, w_s	65 µm	Height, h_s	55 µm	Corner radius, R_c	7 µm

6.3.2 Electroless Ag deposition

One of the major problem encountered during the fabrication was to homogeneously deposit a conductive Ag electrode. In order to generate a deeper understanding of the deposition process, the conductivity between the Cord End terminals was measured during the Ag deposition, as shown in Fig. 6.4. At the beginning of the deposition no connecting path between the Ag grains on the capillary sidewall was measured. After about 300 s the conductivity increased linearly. At a conductivity of 0.2 S, the electroless solution was replaced with deionized water and the conductivity slowly decayed until the complete electroless solution was flushed out of the capillary and the conductivity stabilized around 0.26 S.

From optical observation, it was concluded, that the Ag layer homogeneously deposited inside the capillary, except at the contact points to the Cord End terminals. There, the reaction was suppressed and the gap closed slowly during the deposition. This was explained by the high contamination sensitivity of the Ag deposition. As a consequence, the conductivity was reduced and dominated by the thin connection to the Cord End terminals, which made the estimation of the Ag layer thickness not very conclusive.

The structuring with the microfluidic stopvalve was investigated according to the model developed in chapter 5. The contact angle of NOA63, which was not treated by an oxygen plasma, was measured to be in the range of $\theta_1 = 75°$, determined on an entrapped air bubble inside the dead end capillary of the microfluidic stopvalve. This was in good agreement with Kim et al [134], who reported a contact angle of 70°. A successful stop of the capillary filling is shown in Fig. 6.5 a). The meniscus was stopped at an opening angle of about $\kappa = 45°$. In order to compare this value with the model, the Young-Laplace pressure with regard to the

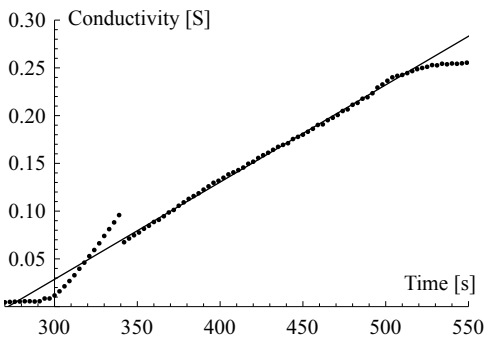

Fig. 6.4 Measured conductivity between two Cord End terminals of one electrode as a function of the deposition time. A formation of an interconnected Ag layer can be measured after 290 s. The conductivity increases linearly indicating constant deposition conditions. From optical observation, it was concluded, that the Ag layer homogeneously deposited inside the capillary, except at the contact points to the Cord End terminals. There, the reaction was suppressed and the gap closed slowly during the deposition. As a consequence, the conductivity was reduced, which made the estimation of the Ag layer thickness not very conclusive.

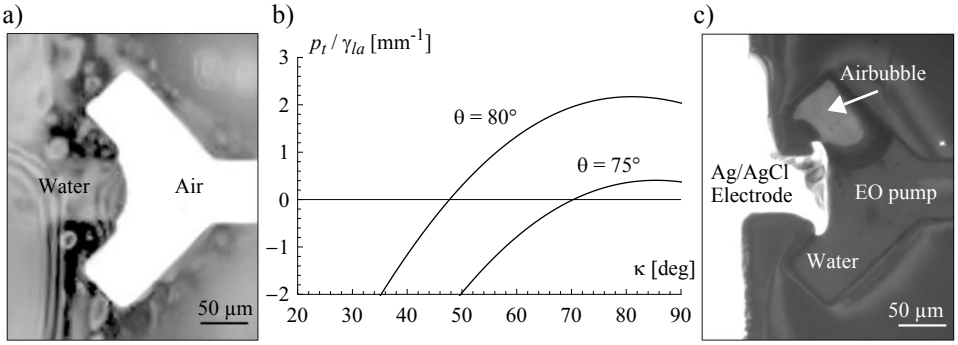

Fig. 6.5 a) Optical microscope image of a microfluidic stopvalve successfully stopping water. The opening angle was determined to be 45°. b) Total Young-Laplace pressure p_t of the microfluidic stopvalve as a function of the opening angle κ. At the transition from negative to positive total Young-Laplace pressure p_t, the meniscus was expected to stop, according to the theory developed in chapter 5. c) Structuring of the Ag/AgCl electrode with the microfluidic stopvalve. The stopvalve was overcome by external pressure and the EO pump was filled with water.

capillary height p_h (Eq. 5.2) needed to be modified to

$$p_h = \gamma_{la} \frac{\cos\theta_1 + \cos\theta_2}{h_s}, \tag{6.3}$$

in order to include two different contact angles θ_1 and θ_2 for the NOA63 and glass surface. The capillary height and the liquid-air surface tension are denoted by h_s and γ_{la}, respectively. With the measured contact angles for NOA63 and glass surfaces, a stop at an opening angle of about κ = 70° was expected, as shown in Fig. 6.5 b). This mismatch could be explained by only an approximative measurement of the opening angle and the contact angle of the NOA63 surface. A slight increase of the contact angle to $\theta_1 = 80°$ matches with the predicted opening angle κ = 45° from the model, as shown in the second graph in Fig. 6.5 b). Finally, a successful deposition and structuring of an electroless deposited Ag layer is shown in Fig. 6.5 c). The Ag layer can be seen as the highly reflective and bright surface on the left side of the optical microscope image. The stopvalve was overcome by applying an external pressure. A void free filling of the stopvalve was not achieved in this case, as it can be seen by the entrapped air bubble in the top. The design for void free filling, as suggested in chapter 5, could not be implemented here due to its comparatively large footprint.

6.3.3 Electroless Ag transformation into AgCl

The transformation of the Ag into the AgCl electrode pose a challenge since the electrode tended to delaminate or crack, as e.g. shown in Fig. 6.6. The growth of AgCl resulted in compressive stress in the electrode due to the lower molar density of AgCl (38 mmol·cm^{-3}) than Ag (97 mmol·cm^{-3}) (Molar mass: Ag(108 g·mol^{-1}) [135] and AgCl (143 g·mol^{-1}) [135]; Density: Ag (10.5 g·cm^{-3}) [135] and AgCl (5.6 g·cm^{-3}) [136]). It turned out that a mechanically stable Ag/AgCl electrode could be fabricated by limiting the transformation to 20% of the initial Ag layer thickness. The transformation process was investigated in details on larger glass µ-capillaries[1]. The Ag layer was deposited according to chapter 5 into a capillary with a radius of 500 µm, to avoid any influence of the ends they

1. Hirschmann, µ-capillary 25 µl

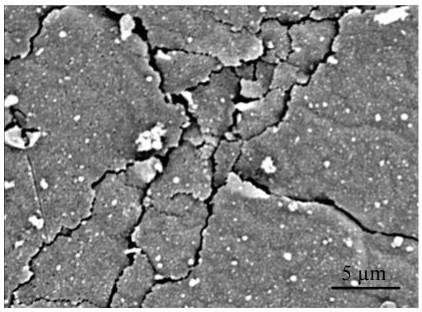

Fig. 6.6 SEM image of crack formation in the electrode during the transformation from Ag into AgCl. It was assumed that these cracks occur due to compressive stress attributed to the lower molar density of AgCl than Ag. It turned out that a mechanically stable Ag/AgCl electrode could be fabricated by limiting the transformation to 20% of the initial Ag layer thickness.

were removed after the deposition to a total capillary length of 2 cm. An Ag layer of 130 nm was deposited inside the capillary. In order to increase the measurement time, another and weaker oxidation agent, ferric(III) chloride, was employed, as used by Polk et al. [137]. The concentration was 0.01 $g \cdot l^{-1}$ and the flow rate 10 $ml \cdot s^{-1}$. The transformation process was again monitored by measuring the conductance. The conductance decreased nonlinear during the transformation process, as shown in Fig. 6.7 a), left ordinate. With the geometry and the specific conductivity, this was directly transformed into the remaining thickness of the Ag layer, since AgCl did not contribute to the conductance [140]. Hence, the diminishing Ag layer, as shown on the right ordinate in Fig. 6.7 a), was a measure for the increasing thickness d of AgCl layer.

The nonlinearity in the AgCl growth was at first surprising and, therefore, investigated in more details. A similar growth characteristic can be found for silicon dioxide (SiO_2). Deal and Grove [141] investigated and modelled the oxidation of silicon (Si). At thin SiO_2 layers, the oxidation is limited by the reaction rate. A linear SiO_2 growth can be assumed. At increasing SiO_2 thicknesses, the growth rate is limited by the diffusion of the oxidizing agent through an increasing SiO_2 layer. Transferring their model to the here presented case, predicts the increasing AgCl thickness d during the transformation time t

$$d^2 + Ad = Bt, \tag{6.4}$$

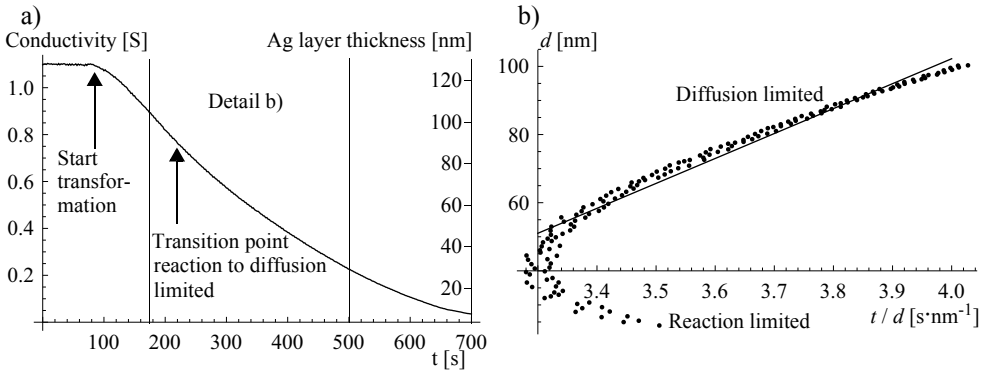

Fig. 6.7 a) Measured conductivity (left ordinate) and calculated Ag layer thickness (right ordinate) as a function of the transformation time. The transformation was started after 100 s. The conductivity decayed nonlinear. At about 210 s, the transition from reaction limited to diffusion limited transformation can be detected. After 500 s, parts of the electrode were completely transferred into AgCl. b) The AgCl layer growth was modelled in the diffusion limited part, according to the Deal-Grove model adapted to the present situation. The Deal-Grove parameters for the linear part of the shown graph were deduced to A = -0.3 µm and B = 0.6 $\mu m^2 \cdot h^{-1}$.

where A was a measure for the oxidation agent diffusion and the reaction rate, and B was a measure for the oxidation agent diffusion and the oxidation agent bulk concentration. The transition point from reaction limited to diffusion limited transformation process was reached after about 110 s after the transformation processes started. Fig. 6.7 b) shows the linearized plot for the Deal-Grove model adapted to the present situation. At the beginning of this graph the reaction limited transformation process can be seen by the data points at the higher abscise and lower ordinate values. The Deal-Grove parameters for the linear part of the shown graph were deduced to A = -0.3 µm and B = 0.6 $\mu m^2 \cdot h^{-1}$. For a conductance of less than 0.2 S (equivalent to an average of 30 nm Ag layer thickness) the Deal-Grove plot slowly saturated since parts of the Ag layer were completely transferred into AgCl.

6.4 Electroosmotic flow measurement

The EO flow was determined by measuring the speed of monodisperse carboxylated microspheres[1] with a radius of 0.7 µm. For this purpose, the chip with the EO pump was mounted with the glass slide towards an inverted fluorescent microscope[2]. The employed testsolution contained 10 $mmol \cdot l^{-1}$ potassium chloride (KCl) and 2 $mmol \cdot l^{-1}$ tris(hydroxymethyl)aminomethane, at a pH of 10 adjusted with NaOH. It was prepared freshly before each experiment and its specific conductivity was measured[3] to be $\sigma_s = 0.197\ S \cdot m^{-1}$.

The speed v_m of the carboxylated microspheres was the result of two electrohydrodynamic effects: The electrohydrodynamic voltage drop U_{eh} induced an EO flow of the testsolution in the capillary and an electrophoretic movement of the microspheres itself. The electrohydrodynamic voltage U_{eh} drop was determined by the electrical conductivity of the EO pump and the conductivity of the remaining electrical system. The electrical conductivity of the EO pump was determined by the product of the testsolution's specific conductivity and the EO pump geometry, and the conductivity of the remaining electrical system was mainly determined by the Ag/AgCl electrodes and the critical connection between the Ag/AgCl electrodes and the Cord End terminals. The electrical conductivity of the system was evaluated by applying different voltages U_0 ranging from -3 V up to 3 V at the Cord End terminals. The current depended linearly on the applied voltage U_0 and a complete electrical system conductivity of G_s = 0.5 µS was determined. From the solution's specific conductivity and the geometry, the conductivity over the EO pump was determined to be G_{eo} = 1.15 µS. Therefore, the electrohydrodynamic voltage drop over the EO pump was calculated to be $U_{eh} = U_0\ G_s / G_{eo}$.

The average speed v of the microspheres was measured as a function of the voltage drop over the EO pump U_{eh}. The average speed of six microspheres was taken, at different positions within the capillary cross section. The microsphere's speed v was split into two parts for better illustration, v_n and v_p for negative and positive applied voltage drops U_{eh} over the EO pump, respectively. In Fig. 6.8 the measured average speed v of the microspheres is shown as a function of the electric field E_h within the EO pump, where $E_h = U_{eh}/L_p$. The two linear fits of the microsphere speed revealed two important parameters: (i) The offset of the two linear fits at $E_h = 0\ V \cdot m^{-1}$ were v_{n0} = -12.8 $\mu m \cdot s^{-1}$ and v_{p0} = -5.4 $\mu m \cdot s^{-1}$. (ii) The gradient of the two linear fits represented the apparent mobility of the microspheres were

1. Polyscience, Flouresbrite YG Carboxylated Microspheres, diameter 1.5 µm
2. Zeiss, Axiovert S40 with a mounted camera AxioCam Mrm and a metal halide lamp HXP 120
3. Conductivity meter, Radiometer Copenhagen, CDM80

$\mu_n = -4.4 \times 10^{-8}$ m^2·V^{-1}·s^{-1}and $\mu_p = -4.6 \times 10^{-8}$ m^2·V^{-1}·s^{-1}. The difference in the offset of the velocities $v_{hy,p} = -7.4$ µm·s^{-1} at $E_h = 0$ V·m^{-1} was speculated to be a remaining hydrostatic pressure difference. The hydrostatic pressure induced flow was calculated to be $Q_{hy} = 26$ pl·s^{-1}, which equaled an average height difference of the two electrode reservoirs of 6.1 µm. Both apparent microsphere mobilities μ_n and μ_p were not significantly different, the average apparent mobility resulted in $\mu_m = -4.5 \times 10^{-8}$ m^2·V^{-1}·s^{-1}. This was a good indicator of a similar transformation into AgCl for both electrodes. Finally, plotting a line with the gradient of the average apparent microsphere mobility μ_m and the average offset of the microsphere speed at $E_h = 0$ V·m^{-1} crosses the x-axis at an electric field E_{h0} within the EO pump of $E_{h0} = 0.2$ V·mm^{-1}. This slight offset E_{h0} defined the minimum applied voltage which was necessary to initiate an electrokinetic movement of the microspheres, i.e. the minimum required applied voltage U_0 between the Cord End terminals was $U_0 = 0.27$ V to initiate EO pumping. This was speculated to be the result of the electrochemical reaction at the electrode.

6.4.1 Electroosmotic induced speed of the microspheres

In order to extract and model the EO flow contribution, the EO mobility μ_{eo} needed to be determined. With Eq. (1.14) from chapter 1, the EO mobility μ_{eo} can be linked to the zeta-potential ζ of the charged surface. In the presented case, the capillary consisted of a glass capped NOA63 trench. The zeta-potential ζ_{gl} of the glass slide was expected to be in the same range, as reported by Scales et al. [143] for a 10 mmol·l^{-1} KCl solution on a fused silica glass capillary, at pH 10, $\zeta_{gl} = -74$ mV. The usage of NOA63 for microfluidic devices was a recent development and not many experimental results on the EO mobility μ_{eo} were available in literature. From literature, it was known that NOA63 was based on polyurethane [134]. The derived zeta-potential ζ_{NOA63} for the NOA63 surface from a polyurethane surface represents only a rough estimate, since the NOA63 surface charge σ_{ch} might be strongly influenced by any eventual functional sidegroups as well as the degree of polymerization. Voigt et al. [144] investigated the zeta-potential ζ of a polyurethane surface[1] for pH values up to 9 at a NaCl concentration of 1 mmol·l^{-1}. In their experiments, it can be seen that the zeta-potential ζ remained relatively constant, around -50 mV from pH 6 to -55 mV at pH 9, hence, it was assumed that the zeta-potential ζ at pH 10 could be approximated by a value of -55 mV. For a low concentration c of counter ions, the zeta-potential ζ, depending on this concentration c, could be approximated by $\zeta \sim -\log c$ [145]. This resulted in an estimated zeta-potential of the NOA63 surface and the testsolution of $\zeta_{NOA63} = -36$ mV. A comparison of the contact angle

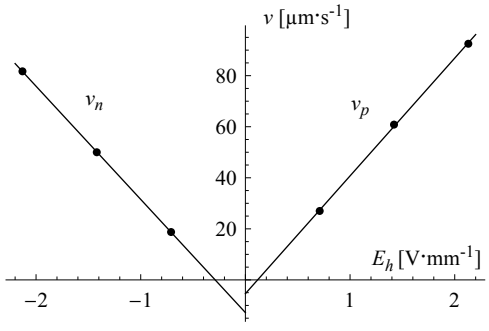

Fig. 6.8 Average speed of the microspheres as a function the electric field E_h within the EO pump. The average was taken for six measured microsphere speeds at different positions within the capillary cross section. The microsphere speed v was split into two parts for better illustration, v_n and v_p.

1. VEB, SYSpur

between the NOA63 surface and the polyurethane surface investigated by Voigt et al. [144] gives an additional idea on the validity of this estimated NOA63 zeta-potential ζ_{NOA63}. The theory of Owens and Wendt [147], especially suitable for a polymeric surface, determines the contact angle according to the disperse and the polar component of the free surface energy, γ_d and γ_p, respectively. With this theory, the contact angle of water ($\gamma_{dl} = 21.8$ mN·m^{-1} and $\gamma_{pl} = 21.8$ mN·m^{-1} [146]) on the polyurethane surface ($\gamma_{ds} = 32.2$ mN·m^{-1} and $\gamma_{ps} = 2.6$ mN·m^{-1}) investigated by Voigt et al. [144] was determined to be $\theta = 87°$. This contact angle was higher than the one measured on the NOA63 surface ($\theta = 75°$). Nevertheless, the contact angle of the NOA63 surface for the highly polar liquid, water, was still higher than the one measured on the glass surface, which was in the range of $\theta = 50°$. To conclude, a zeta-potential $\zeta_{NOA63} = -74$ mV for the NOA63 surface was chosen. This was slightly too low since its potential should be slightly higher than for the polyurethane surface (-74 mV) measured by Voigt et al. [144] and significantly lower than for the glass surface (-36 mV) measured by Scales et al. [143]. The average zeta-potential ζ_{cs} for the capillary surface was determined by the weighted fraction of the cross sectional perimeter to $\zeta_{cs} = [\zeta_{gl} w + \zeta_{Noa63}(2d + w)]/(2d + 2w) = -48$ mV, where w and h denote the width and the height of the EO pump, respectively. With Eq. (1.14) from chapter 1, the EO mobility μ_{eo} was determined to

$$\mu_{eo} = \frac{\varepsilon\varepsilon_0\zeta}{\eta} = -3.3 \times 10^{-8}\ \mathrm{m^2 \cdot V^{-1} \cdot s^{-1}}, \tag{6.5}$$

where ε ε_0 and η denote the dielectric constant of water ($\varepsilon = 78$) and the viscosity of water ($\eta = 1$ mPa·s), respectively. Since the EO pump was integrated into a fluidic system, the hydraulic resistances of the capillaries connecting the EO pump to the outside, the electrode capillaries, imposed a hydraulic load on the EO pump. This reduced the EO flow rate and it can be modelled by assuming a reduced EO mobility μ^*_{eo},

$$\mu^*_{eo} = \mu_{eo}\frac{R_{hy,p}}{R_{hy,s}} = \mu_{eo}\frac{R_{hy,p}}{R_{hy,e} + R_{hy,p}} = -2.3 \times 10^{-8}\ \mathrm{m^2 \cdot V^{-1} \cdot s^{-1}}, \tag{6.6}$$

according to Eq. (6.2). The capillary's hydraulic resistance were $R_{hy,e} = 6.97 \times 10^{11}$ Pa·s·m^{-3} and $R_{hy,p} = 1.64 \times 10^{12}$ Pa·s·m^{-3} after fabrication, according to Eq. (1.4) and Table 6.1.

6.4.2 Electrophoretic induced speed of the microspheres

The electrophoretic mobility μ_{ep} of carboxylated latex microspheres (Interfacial Dynamics Cooperation, radius = 155 nm) was measured to be

$$\mu_{ep} = -6.5 \times 10^{-8}\ \mathrm{m^2 \cdot V^{-1} \cdot s^{-1}}, \tag{6.7}$$

for a solution of 10 mmol·l KCl at pH 10 by Behrens et al. [148]. An electrophoretic experiment for a rough estimation, performed with the microspheres used in this research, indicated a similar electrophoretic mobility. Furthermore, for both radii, 155 nm and 0.7 µm, the Smoluchowski limit of $r / \lambda_D >> 1$ was reached, where λ_D represents the thickness of the Debye layer.

6.4.3 Combined velocity of the microspheres

The contribution of the EO effect and electrophoretic effect needed to be combined to obtain the estimated apparant mobility μ_{mm} of the microspheres. Both surfaces, the surface of

the chip and the surface of the microspheres, were negatively charged. This resulted in an opposing effect of electroosmosis and electrophoresis, hence the estimated apparent mobility μ_{mm} of the microspheres resulted in

$$\mu_{mm} = \mu_{ep} - \mu^*_{eo} = -4.2 \times 10^{-8}\ m^2 \cdot V^{-1} \cdot s^{-1}. \quad (6.8)$$

This estimated apparent mobility μ_{mm} of the microspheres was in good agreement with the measured average apparent mobility μ_m of the microspheres, $\mu_m = -4.5 \times 10^{-8}\ m^2 \cdot V^{-1} \cdot s^{-1}$. Finally, the EO pump rate Q_{eo} was calculated with Eq. (6.2) by inserting Eq. (6.8), the measured average apparent mobility μ_m of the microspheres and assuming that the electrophoretic mobility μ_{ep} of the microspheres was correct. This resulted in an EO pump rate Q_{eo} as a function of the voltage drop over the EO pump U_{eh} as $Q_{eo} = 0.12\ nl \cdot s^{-1} \cdot V^{-1}\ U_{eh}$.

6.5 Electrochemical measurement

First experiments were performed to use the Ag/AgCl electrode inside a µ-capillary as an electrochemical sensor. A simple experiment to verify the quality of the Ag/AgCl electrode was to replace the reference electrode of a pH-meter[1] with the microfabricated electrode and to perform a pH measurement. In this case, it was an indirect verification since the pH sensitivity was not caused by the Ag/AgCl electrode, but by the ion-sensitive glass membrane of the pH meter. For this purpose, the Ag/AgCl electrode inside a µ-capillary and the pH-meter electrode were placed into solutions with a constant KCl concentration of 3 $mol \cdot l^{-1}$ at a varying pH value. The electrical loop was, in this case: Ag/AgCl electrode inside a µ-capillary || solution || ion sensitive glass membrane || indicator Ag/AgCl electrode of the pH meter. The double bars represent transitions between the different medias. The measured pH response is shown in Fig. 6.9, for a temperature of 22.7° C. The pH response curve increased linear with the pH value. The sensitivity was determined to be 57.4 $mV \cdot pH^{-1}$, which was in good agreement with the expected Nernstian behavior of 58.6 $mV \cdot pH^{-1}$.

6.6 Conclusions and outlook

A quick, easy and cheap fabrication of an EO pump based on polymer casting, flow electroless Ag deposition and a transformation into AgCl electrodes was shown. The hydrophilic capillaries (hydraulic dimension in the range of 65 µm) of the EO pump were fabricated by NOA63 trenches capped with a microscope glass slide. The Ag electrodes were deposited out of a flow of electroless Ag deposition solution and structured with microfluidic stopvalves. The transformation process to obtain Ag/AgCl electrodes was investigated in detail. It was found that the transformation process was similar to the oxidation of Si and can

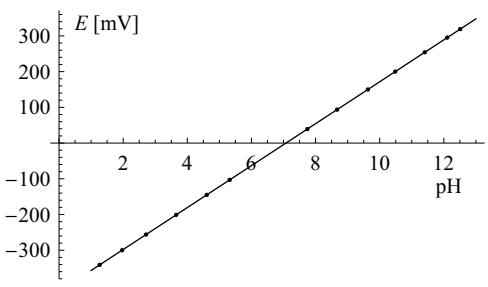

Fig. 6.9 The quality of the Ag/AgCl electrode inside a µ-capillary was verified by replacing the reference electrode of a pH-meter with the Ag/AgCl electrode inside a µ-capillary. The electrical loop was closed with the ion-sensitive indicator electrode of the pH-meter. The graph shows the measured potential *E*, measured as a function of the pH value. The slope of the measured pH response curve was determined to be 57.4 $mV \cdot pH^{-1}$ at 22.7 °C.

1. Mettler Toledo, SG 2

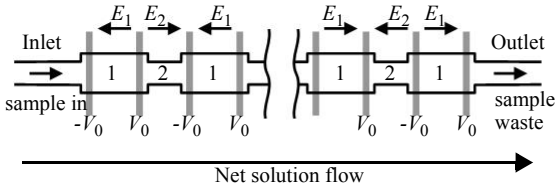

Fig. 6.10 Sketch of a low voltage capillary electrophoresis sensor. The setup takes advantage of the dependency of the electroosmosis on the capillary cross section, whereas electrophoresis is independent of the capillary cross section.

be described by the Deal-Grove model [141]. The final EO pump was modelled and characterized by measuring the velocity of fluorescent carboxylated microspheres inside the EO pump. From that, the EO flow rate was determined to be $Q_{eo} = 0.12\ \mathrm{nl \cdot s^{-1} \cdot V^{-1}}\ U_{eh}$ depending on the voltage drop U_{eh} over the EO pump. Finally, a first experiment of testing the Ag/AgCl electrodes as an electrochemical sensor were performed, where the Ag/AgCl electrode was placed as a reference electrode for a pH-meter. A pH sensitivity of 57.4 mV $\mathrm{pH^{-1}}$ at 22.7° C was determined, which was in good agreement with the expected Nernstian behavior. The combined electrohydrodynamic effects on the microspheres, electroosmosis and electrophoresis, might be used for a promising approach to reduce the applied voltage (in the range of kV) needed in conventional capillary electrophoresis and integrate it as an electrochemical sensor into the SIP. In capillary electrophoresis, high voltages are applied over the entire capillary and a separation of bio-molecular solutions is achieved due to different electrophoretic mobilities of various molecules. In order to sufficiently separate individual bio-molecules, a long capillary is required, hence, to maintain a high enough electric field, a high voltage needs to be applied. By the use of a manifold of electrodes initiating electroosmosis and electrophoresis on shorter capillary segments, this applied voltage V_0 can be reduced. A sketch of a possible electrochemical sensor for the integration into the SIP is shown in Fig. 6.10. The sample, containing the solution of bio-molecules aspired through the tip, is injected in the center of the modified capillary electrophoresis element. The electrophoretic separation capillary is divided into two sections 1 and 2 with two different capillary cross sections A_1 and A_2 since electroosmosis depends linearly on the capillary cross section and electrophoresis is independent of the capillary cross section. Since a low concentration of bio-molecules is expected the EO mobility is mainly determined by the used buffer solution, hence, it is bio-molecule concentration independent. By adjusting the capillary section lengths l_1 and l_2 according to the capillary cross section A_1 and A_2, the EO backpressure of two consecutive segments can be adjusted as such that the solution is propelled towards the outlet. The average EO velocity of the solution must be sufficiently high to transport bio-molecules with both charges towards the outlet and it must be low enough to achieve the highest separation. Nevertheless, the serial configuration causes a recirculation flow in the wider segment as a consequence of the EO flow at the capillary sidewall and a total hydrostatic pressure induce laminar back-flow in the center of the capillary. This results in a non constant solution velocity profile within the capillary cross section. Therefore, the influence of this recirculation flow on the electrophoretic velocity of the bio-molecules needs to be reduced, this can be done with a large number of segments in series. This also increases the total sensitivity since the bio-molecules remain longer in the capillary electrophoresis sensor.

Chapter 7

Imaging and dispensing with the scanning ion pipette

A successful experiment with dispensing and scanning force microscope (SFM) imaging at the same time was impressively demonstrated by the work of Meister et al. [149]. They showed the ability of the scanning ion pipette (SIP) to image living cells and selectively introduced a fluorescent dye into the cell. Especially, imaging of living cells requires the operation of the SFM in challenging conditions, in contact mode and in liquid, as well as on a very delicate sample. Furthermore, it requires a highly sensitive force-feedback in order to distinguish between imaging the cell and perforating the cell membrane to introduce the dye. The process to fabricate their SIPs was similar to the one described in chapter 2. Here, my own experience with the SIP for imaging and fluid dispensing is presented.

7.1 Scanning force microscopy imaging with the scanning ion pipette

The SFM properties of the SIP sensor chip were: A measured cantilever resonance frequency of 159 kHz and a quality factor of 186, as well as a calculated stiffness of 6.5 $N \cdot m^{-1}$. These cantilever properties allow scanning force microscopy imaging in contact, as well as tapping mode. The Si_3N_4 tip height was measured to 2.4 µm with a measured tip radius in the range of 40 nm. To increase the signal of the reflected laser beam, the cantilever was coated with a 10 nm Au layer from the backside. For a first experience with the SIP mounted on a SFM[1], a less delicate sample, in less challenging conditions, was chosen. The imaging capabilities were illustrated by measuring a fixed and dried Escherichia Coli bacteria in tapping mode, as shown in Fig. 7.1. The color z-scale for this image was 550 nm. The surface topology can be seen with a resolution down to the 10 nm range.

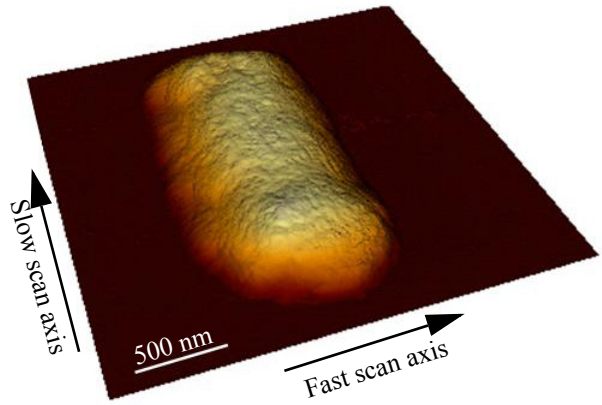

Fig. 7.1 Scanning force microscopy image of a fixed and dried Escherichia Coli bacteria obtained by the SIP. The z-data scale ranges up to 550 nm. The SFM characteristics of the SIP were: A measured cantilever resonance frequency of 159 kHz and a quality factor of 186, as well as a calculated stiffness of 6.5 $N \cdot m^{-1}$. The Si_3N_4 tip had a height of 2.4 µm with a tip radius in the range of 40 nm.

1. JPK Instruments, Nanowizard

7.2 Fluid dispensing with the scanning ion pipette

7.2.1 Interface: scanning ion pipette and scanning force microscope holder

The backside of the SIP, as shown in Fig. 7.2 a), was mounted to the SFM holder. The exterior dimensions on the backside surface were 1.5 mm × 3.5 mm with positively inclined sidewalls, 54.7°. The thickness of the SIP was about 390 µm. The fluidic connection from the SIP to the SFM holder was established by the potassium hydroxide (KOH) etched through wafer hole, serving as a connection to the fluidic system. It had the shape of an inverted truncated pyramid with a square shaped baseplate, having a width of 580 µm. The fluidic connection was separated from the outline of the SIP by a small rim of 30 µm to the front and a wider rim of 80 µm to the sides. On the sampleside, the fluidic through wafer connection led to the fluidic system. The fluidic system and the cantilever consisted of two parallel capillaries with a length of 500 µm and a cross section of 2 µm × 4 µm, which were connected to the sample by an outlet hole in the tip. In order to increase the dispensing flow rate in these first experiments, the diameter of the outlet hole was increased to 1 µm from the originally designed 100 nm. This decreased its hydraulic resistance and decreased the retaining capillary pressure at the exit of the outlet hole.

The alignment of the SIP to the SFM holder was defined by the laserspot from the SFM. It had to be placed on the backside of the SIP tip for an appropriate SFM operation. Fig. 7.2 b) shows a sketch of the SFM holder. The used SFM holder was a commercially available liquid cell[1] from a veeco SFM[2]. The SIP was placed on an about 1.5 mm wide recess, which was inclined by 20° from the horizontal sample plane. The SFM holder needed to be modified in order to establish the fluidic connection to the SIP. A hole with a diameter of 250 µm was drilled into the channel, already existing in the SFM holder and buried underneath the recess. To avoid leaking of that channel, the original outlet was sealed with a glass slide. The drawback of this solution, the drilled hole in the SFM holder had a distance of 1.5 mm to the laserspot, which does not match the dimensions of the SIP chip. The fluidic outlet of the SFM

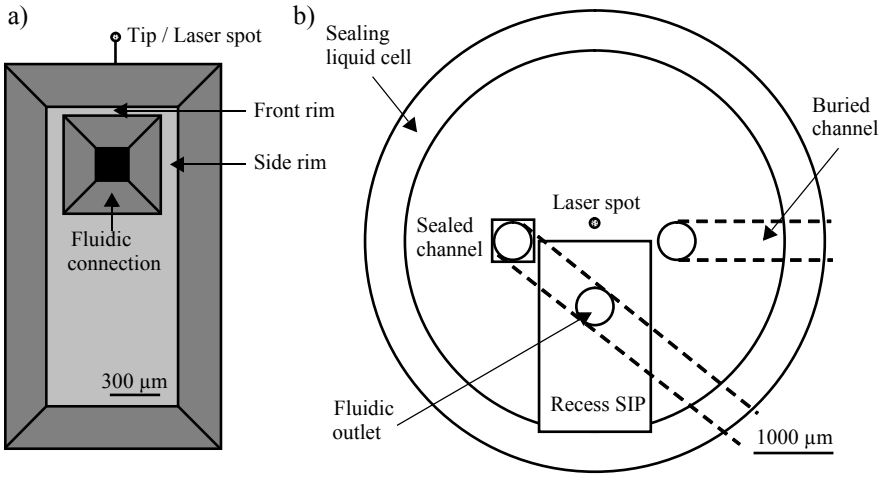

Fig. 7.2 a) Sketch of the SIP's backside showing the fluidic connection. The SIP needed to be aligned to the SFM holder such that the laser spot from the SFM was placed on the tip. b) Sketch of the modified SFM holder.

1. Veeco, NanoScope liquid cell
2. Veeco, NanoScope V

holder was misalignment by about 0.5 mm to 1 mm relative to the fluidic inlet of the SIP. This misalignment had to be compensated by an improvised interface.

7.2.2 Sealing agents and procedure

For the sealing between the SIP and the SFM holder, UV curable glues with a low viscosity[1] and a high viscosity[2], as well as polydimethylsiloxane[3] (PDMS) were used. The UV curable glue had the advantage of providing enough time for alignment underneath the stereo microscope before it hardened out. Especially, the low viscous glue had strong capillary forces between the silicon dioxide (SiO_2) surfaces of the SIP and the SFM holder which allowed reliably closing tiny gaps. The UV glue formed a strong bond between SiO_2 surfaces of the SIP and the SFM holder, but it did not bond to the second sealing agent PDMS. The downside of the UV glue was that it dissolved and swelled in water or ethanol based dispensing solutions. As a consequence, the solution and the capillaries were contaminated with patches of glue and the bond-strength of the gluing deteriorated during exposure to the dispensing solution. To circumvent this problem, PDMS was used to shield the UV glue from the dispensing solution. PDMS provided an elastic sealing material with good sealing properties to the SiO_2 surfaces which did not dissolve in the dispensing solution. It prevented capillary filling of the interface between PDMS and SiO_2 for distances larger than 50 µm. For shaping, it was easily cut by the tip of a syringe needle or casted as described in chapter 6. Nevertheless, it did not provide a sufficient mechanical bond, hence, a combination of UV glue and PDMS was necessary.

The mounting and sealing procedure of the SIP to the SFM holder is shown in Fig. 7.3**. a)** The SIP was placed in an oxygen plasma for 20 min., right before starting the sealing procedure, in order to clean it and activate the SiO_2 surface, as well as improve the capillary filling. **b)** To increase the width of the small rim at the front of the SIP's fluidic connection, small glass bars with a width of about 100 µm were placed on the SIP. These glass bars were glued to the SIP, by placing a minute droplet of low viscous UV curable glue on the outside of the glass bars, at the interface between glass and SIP. Capillary forces sucked the UV glue into the interface between SIP and glass and then the UV glue was cured. **c)** To form an elastic seal and to create the connection channel between the fluidic connection of the SIP and the hole in the SFM holder, narrower PDMS bars were placed on the glass bars. This reduced the contact area between the dissolvable UV glue and the dispensing solution. **d)** A thin layer of high viscous UV glue was dispensed on the glass bars outside the PDMS ring and not cured yet. It was important that the layer of UV glue was thinner than the PDMS ring, to not cover the PDMS bars in the subsequent step. **e)** The SIP was aligned on the SFM holder and the non cured UV glue formed a meniscus between the SiO_2 surface of the SIP to the SiO_2 surface of the SFM holder. After curing, this formed a reliably strong mechanical bond between the SIP and the SFM holder. **f)** Finally, the recess and the close surrounding of the SIP was filled with low viscous UV glue in order to seal any leakages. In case there was a thin layer of UV glue in between the SFM holder and the SIP tip, a sufficient feedback signal to the SFM was not achieved, due to the intensity loss of the laser beam in the glue layer. Hence, this glue layer needed to be removed mechanically.

1. Loctite, 3491 UV curable glue
2. Loctite, 4305 UV curable glue
3. Dow Corning, Sylgard 184

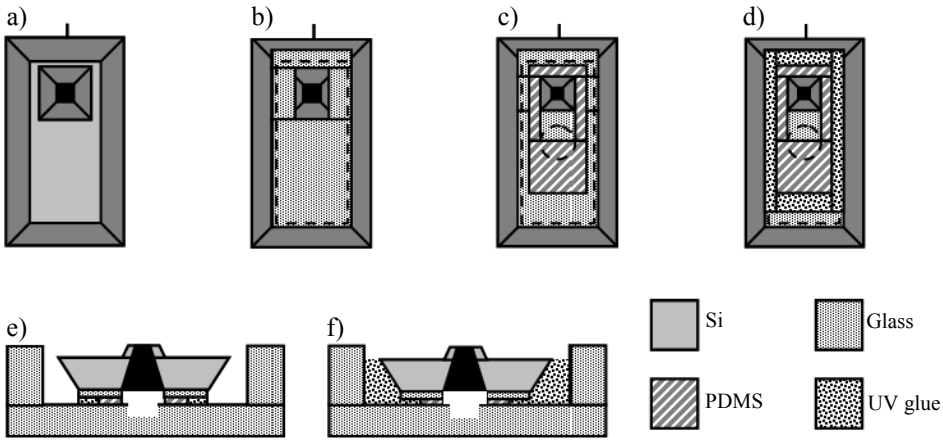

Fig. 7.3 Mounting and sealing procedure of the SIP on the SFM holder. **a)** The SIP is placed in the oxygen plasma to clean and activate the SiO_2 surface. **b)** To increase the width of the small rim at the front of the SIP's fluidic connection, small glass bars are placed on the SIP. These glass bars are glued to the SIP with low viscous UV curable glue from the outside of the glass bars. **c)** To form an elastic seal and to create the connection channel between the fluidic connection of the SIP and the fluidic connection of the SFM holder, narrower PDMS bars are placed on the glass bars. **d)** A thin layer of high viscous UV glue is dispensed on the glass bars outside the PDMS ring and not cured yet. **e)** The SIP is aligned on the SFM holder and the UV glue is cured. **f)** Finally, the recess and the close surrounding of the SIP is filled with low viscous UV glue in order to seal any leakages.

7.3 Dispensing results and discussion

In total, six SIPs were fluidically connected to the SFM holder and in only one case a flow out of the SIP tip could be detected. The main sources of failure were, either breaking of the SIP cantilever during the mounting procedure or a non filling of the capillary. Fig. 7.4 shows a typical fluorescent image of a filled fluidic through wafer connection and the non filling of the capillary. In most cases, traces of dissolved and subsequently dried glue residues were found in the capillary, which probably caused the non filling. A known approach to reduce the solubility of the UV glue in the dispensing solution was to bake it overnight at 80° C. Nevertheless, the capillaries were still not filled yet, probably due to the long time passed since the cleaning and activation of the capillary surface by the oxygen plasma. A satisfying and reliable solution was not found, other than reducing the contact area of UV glue by the PDMS spacers.

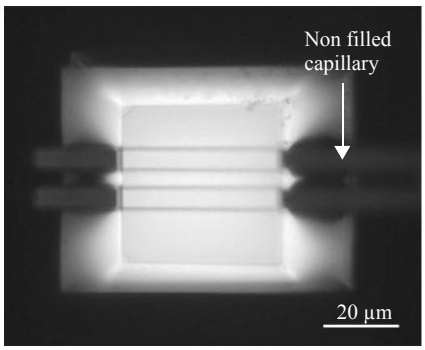

Fig. 7.4 Fluorescent microscope image of a non capillary filling of the SIP's fluidic system. The main causes for that were either patches of dissolved and re-dried glue residues inside the capillary or a reduced capillary wetting due to a long time gap from the oxygen plasma treatment.

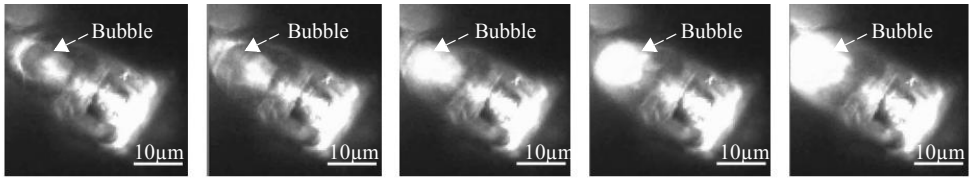

Fig. 7.5 Fluorescent microscope image of a dispensing experiment with the SIP. An external pressure of 100 Pa is applied to dispense fluorescein solution out of the tip. A slow generation of a bubble next to the tip hole can be seen. The time span between the images was 1s.

For the successful dispensing, the SIP was mounted into the SFM holder, following the previously described procedure. Instead of mounting the holder into the SFM, it was mounted on a fluorescent microscope, to observe the filling of the capillary and the flow out of the tip. The dispensing solution consisted of 10 $mmol \cdot l^{-1}$ fluorescein in water. A dispensing pressure was generated by attaching a flexible silicone tube to the SFM holder and filling the tube up to a level of about 10 cm higher than the SIP, which equals a hydrostatic pressure of 100 Pa. A flow of fluorescein solution out of the SIP tip was detected, as shown in Fig. 7.5. A slow generation of a fluorescein bubble at the outlet hole of the SIP tip is shown in a sequence of five consecutive images with a time span of 1 s. The image quality could not be improved since the images were taken at the resolution and magnification limit of the fluorescent microscope. A long working distance objective with a magnification of 50 times was used which provided just enough depth of focus to observe the complete SIP tip and bubble topography.

7.4 Summary and conclusions

A successful scanning force microscopy imaging of a fixed and dried Escherichia Coli bacteria with the SIP was shown. The obtained images had a horizontal resolution in the 10 nm range. Moreover, no special skills in handling the SFM were required, since it did not perform differently with a mounted SIP than with a mounted standard commercially available SFM chip. In order to scan more delicate biological samples, the stiffness of the cantilever should be reduced. This seems feasible by, first, using only one capillary as a cantilever instead of a doubled hairpin capillary, second, reducing the SiO_2 sidewall thickness of the capillary and finally, increasing the length of the cantilever.

The fluidic mounting of the SIP into the SFM holder needs to be improved. With the currently used method of gluing the SIP to the SFM holder, no satisfying and reliable mount was achieved. Furthermore, this mounting procedure required full concentration and working underneath a stereo microscope for at least two hours. An alternative mounting procedure is presented in the following section, which requires an additional deep reactive ion etching (DRIE) step.

7.5 Outlook: Alternative sealing approach

From the previous experiments it turned out, that the following problems needed to be solved:

1. The alignment mismatch between the fluidic connection of the SIP and the SFM holder needed to be reduced. The alignment mismatch can be overcome by placing the SIP's fluidic connection into the SIP's center. As a consequence, the hydraulic resistance is increased due to the longer fluidic system's capillaries. However, this increase is still negligible compared to the hydraulic resistance of the outlet hole in the tip.
2. The bond-strength between SIP and SFM holder needed to be improved. No glue should be in contact with the solution. To improve the mechanical bond-strength between SIP and SFM holder, the backside of the SIP should be prestructured with a sealing and clamping structure. This modified SIP backside can then be PDMS casted, as described in chapter 6. This PDMS cast provides an elastic and soft intermediate sealing layer in between the SIP and the SFM holder, which is mechanically strong enough to omit the UV glue.
3. The alignment of the SIP to the SFM holder should be facilitated, preferably by self-alignment.

This should result in an easier and faster mounting, in order to keep the enhanced wetting of the capillaries by the oxygen plasma.

The sealing structure enlarges the surface of the SIP and, hence, increases the interface area to the PDMS. The clamping structure provides a buried and recessed structure for a strong mechanical bond. Its fabrication is based on DRIE with subsequent KOH etching, similar to the process presented by de Boer et al. [150] for buried microchannels. For the sealing and clamping structure, the process flow of the SIP base-wafer as described in chapter 2 needs to be slightly extended, as shown in Fig. 7.6. The modification starts with outlining

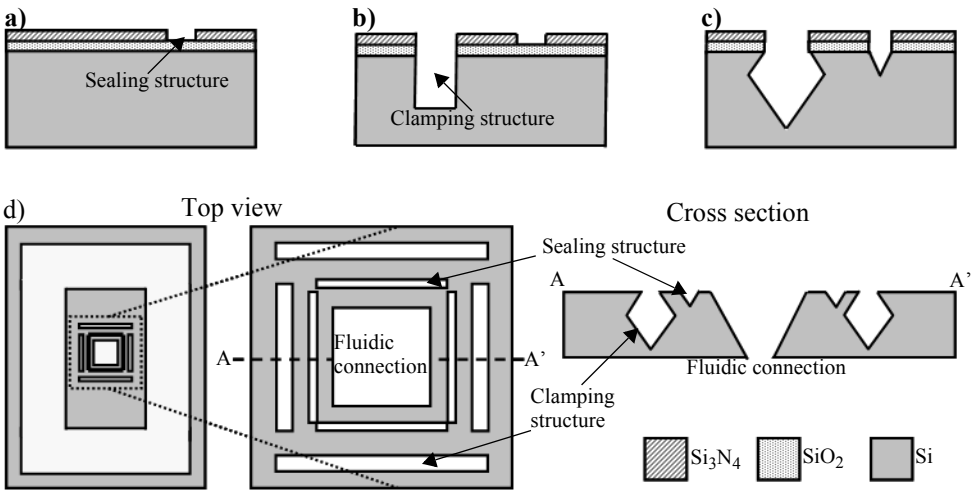

Fig. 7.6 Modification of the SIP process flow to integrate sealing and clamping structures in the SIP backside. **a)** In addition to the fluidic connection, the sealing structures are outlined with RIE into the KOH etch mask. Only the Si_3N_4 layer is removed. The remaining SiO_2 layer protects these openings from the DRIE etching and creates a shadow mask **b)** The clamping structure is outlined with DRIE etching. **c)** The SiO_2 of the shadow mask is opened with BHF. The process flow is continued with KOH etching and without any further modifications. d) Shows a sketch of the resulting sealing and clamping structures integrated into the SIP backside after the complete base-wafer fabrication.

the KOH mask for the fluidic connection by reactive ion etching (RIE) into the Si_3N_4 and SiO_2, step c) of the base-wafer fabrication. **a)** The rim surface around the fluidic connection can be enlarged with a sealing structure. Narrow rectangles should be placed around the fluidic connection. These rectangles are outlined in the same RIE step as the fluidic connection. The RIE etches only the Si_3N_4 layer and not as previously designed also the SiO_2 layer. Etching only the Si_3N_4 layer reduces the stepheight for the subsequent photolithography for deep DRIE structure. It also serves as a shadow mask, which can be opened without a photolithography step. **b)** The clamping structure is outlined with DRIE etching. **c)** The SiO_2 of the shadow mask is opened with buffered hydrofluoric acid (BHF) and the process flow is continued without any further modifications. After the KOH etching, the sealing structure results in long trenches with a triangular cross section and the clamping structure results in recessed diamond structures buried in the bulk Si backside of the SIP as shown in Fig. 7.6 d). The clamping structures facilitates the alignment and maybe even allows self alignment.

In order to adequately PDMS cast the recessed structure, freshly prepared PDMS should be used. The extraction of entrapped air in the buried recessed clamping structure can be supported by placing the cast into a vacuum chamber. This enables entrapped air bubbles to grow and to escape through the liquid PDMS. After the air bubbles escaped and the PDMS surface smoothened, the cast should be brought back to atmospheric pressure and cured at room temperature overnight. The mechanical bond-strength between PDMS and the SIP's SiO_2 surface can be increased by an oxygen plasma bond [151]. The SIP should be cleaned in the oxygen plasma for 20 min. Then, the fully cured PDMS cast should be exposed for short time to a low plasma power, in order to initiate the PDMS SiO_2 plasma bond. Instead of curing this bond for usually 16 h, the SIP should be used immediately to keep the capillaries wetting properties of the oxygen plasma. For the SFM holder only a few minor modifications are required. The roughly milled surface of the recess for the SIP should be polished in order to support the sealing of the intermediate PDMS layer. In order to provide sufficient clamping pressure, three pins instead of one should be used to press the SIP into the SFM holder.

Chapter 8

Conclusions and recommendations

8.1 Conclusions

The primary aim of this research was to built a tool to investigate at the nanometer scale surface changes induced by locally administering chemically or biologically active solutions, the so called scanning ion pipette (SIP). For this purpose, an already existing technology of a micropipette integrated into a scanning force microscope (SFM)-chip was enhanced by the use of electrodes for on-chip electrochemical sensing and electroosmotic (EO) pumping. The integration of an EO pump offered the possibility of storing, selecting and dispensing multiple different liquids with the SIP chip. For a high density and convenient electronic integration, an EO pump with a small footprint (less than 100 µm × 100 µm) and low actuation voltage (less than 10 V) had to be developed. During the time frame of this dissertation thesis, two important steps in the development of the SIP were achieved. First, the development and analysis of an EO pump within a fluidic system comparable to SIP capillary dimensions and second, the fabrication and the electrode integration into the SIP itself.

An EO pump with platinum (Pt) electrodes, based on a simplified fabrication process resulting in comparable SIP capillary dimensions, was experimentally analyzed and modelled. The EO pump achieved a flow rate of 50 $pl \cdot s^{-1}$ at a low actuation voltage of 5 V. The developed corresponding model of the flow within the fluidic system was in good agreement with the measured values. According to the model, an EO pump with a high backpressure (3.6 $kPa \cdot V^{-1}$), enabling a high dispensing flowrate of 1.5 $pl \cdot V^{-1} \cdot s^{-1}$ (SIP immersed in water, outlet hole radius of 100 nm) can be built. For the design of the EO pump, a SIP specific on-chip solution was required to remove the emerging electrolyzed gases from the Pt electrodes. This was achieved by integrating the electrodes into a liquid-gas (LG) separator. The novel concept of the LG-separator reliably separated the gas bubbles from the liquid and guided them away from the EO pump. The LG separation was solely based on the LG-separator's geometry of a tapered sidewall. This took advantage of the high capillary pressure occurring at the bubble's liquid gas interfaces in this small scale. For a deeper understanding, the development and the propagation of the bubble within the LG-separator was analytically described in three dimensions. The model and the derived design guidelines showed that Pt electrodes combined with the LG-separator open an interesting new field for complex high density electrohydrodynamic and electrochemical microfluidic applications. Among others, valves and displacement pumps with high actuation pressures, as well as, sensor structures for voltammetry can be designed.

The second approach aimed for a direct integration of silver/silver chloride (Ag/AgCl) electrodes into the SIP. At the beginning of this Ph.D. thesis, a process to fabricate the SIP capillaries was already developed by Hug et al. [152]. A further improvement achieved a process suitable for the design of a network of capillaries with a complex geometry for a multifunctional microfluidic system. The crucial point in this fabrication process was a high temperature step to form the silicon dioxide (SiO_2) capillary sidewalls which favoured an

implementation of the electrodes as a postprocess. The advantage of the Ag/AgCl was that during actuation no electrolyzed gases emerged compared to Pt electrodes. Hence, the footprint of the EO pump could be further reduced since no LG-separator is required. The processflow to integrate the electrodes as a post SIP capillary fabrication step was:

1. The adhesion of the Ag electrode to the capillary sidewall was improved by using an intermediate polymeric layer. This turned out to be essential for reliably stable Ag electrodes in a capillary dimension of less than 10 µm, since the strong capillary force tended to delaminate the electrode.
2. The electroless deposition process solved the challenges to deposit electrodes in closed capillaries. One of the main requirements for the development of the electroless deposition process was to deposit thick electrodes out of a minute available capillary volume. Thick electrodes were required for a continuous actuation of the Ag/AgCl electrode, since, depending on the electrode polarization, either Ag or AgCl was consumed. The best process control was achieved with an improved Tollens solution, additionally containing sodium citrate and sodium hydroxide to control the reaction speed. Two different methods of electroless deposition were employed: First, a dip process of multiple depositions which enabled a batch fabrication of the electrodes and second, a single electrode flow deposition providing continuously fresh electroless solution. Despite the individual electrode deposition, the flow deposition was favourable since the concentration could be kept constant throughout the capillary during the complete deposition time. This provided a better reaction control due to a lower concentration. It also reduced the effect of the minute available capillary volume and it compensated more effectively the high contamination sensitivity of the electroless deposition process.
3. The electrode structuring was performed by controlling the filling of the capillaries with electroless plating solution by means of microfluidic stopvalves. The requirement on the stopvalve had to be twofold, the solution was reliably stopped during the electroless deposition and afterwards the stopvalve had to be filled in a void free way to ensure correct fluidic actuation of the final device. Therefore, the stopvalve was designed such that a switching from stopping to transmitting the solution was induced by a change in the solution's surface tension and its corresponding change in the contact angle. This behavior was modelled by improving the previous two dimensional model [153] to a three dimensional one, additionally including also the fabrication specific corner rounding and low capillary cross section's aspect ratio.
4. After the electroless deposition and structuring, the Ag electrode was further transformed into an Ag/AgCl electrode. In a similar process as to the electroless Ag deposition, the electrode transformation was performed with a flow of either sodium hypochloride (0.3 $mmol \cdot l^{-1}$) or ferric(III) chloride (0.1 $g \cdot l^{-1}$). The electrochemical transformation was limited to 20% of the initial Ag layer thickness, due to stress-related electrode delamination or cracking, originating in the density difference of Ag and AgCl.

Electrodes were deposited into three different capillaries: a) into the SIP capillary itself (cross section 2.2 µm × 3.7 µm), b) for larger availability and easier accessibility, into commercially available round capillaries (radius up to 520 µm), and c) a polymeric microfluidic system with rectangular capillaries (cross section 55 µm × 65 µm). Inside the SIP, a successful electroless deposition in a dip like process and stopvalve structuring of Ag electrodes, as well as a subsequent void free filling of the stopvalve was shown. In the round capillary, multiple electroless dip-depositions revealed that each deposition increased the Ag layer thickness by 51 nm. The deposited Ag layer had a high specific conductivity of

6×10^7 S·m^{-1}, indicating a high purity and density. The further transformation into Ag/AgCl provided electrodes for electrochemically measuring different pH values. A linear pH sensitive of 57.4 mV·pH^{-1} at 22.7° C with a good agreement of Nernstian behavior was reached, indicating the usefulness of the electrode as an electrochemical sensor. Into the polymeric fluidic system, Ag/AgCl electrodes were electrolessly flow deposited, forming an EO pump. Its pump rate was experimentally determined to 0.12 nl·s^{-1}·V^{-1}. From the experience obtained during these experiments, three main conclusions can be drawn for the SIP: First, an Ag electrode deposition and structuring is possible, but second, especially at the small SIP cross section, the reliability of the electroless deposition process is highly sensitive to contaminations. Third, with further research, it seems feasible that Ag/AgCl electrodes can be further downscaled and used for EO pumping and electrochemical sensing inside the SIP's microfluidic systems.

Comparing both approaches, the integration of Pt electrodes and the post Ag/AgCl electrode deposition, showed that the focus of further research should be placed on the integration of the Pt electrode into the SIP. Despite the fact, that Ag/AgCl electrodes enable the fabrication of an EO pump with a smaller footprint and facilitate an improved electrochemical sensing, a reliable batch fabrication of Ag/AgCl electrodes requires a stronger investigative effort. Whereas, Pt electrodes can be deposited and structured with standard microfabrication techniques. Once the Pt electrodes are integrated and the design guidelines for an on-chip EO pump turn out to be valid, the problems during dispensing with the SIP, encountered in chapter 7, should be overcome. This should provide a unique and powerful SFM chip with an on-chip integrated active microfluidic and electrochemical system.

8.2 Recommendations

A first assessment of the upcoming challenges for the Pt electrode integration into the SIP revealed, that an investigation is needed for the choice of the appropriate intermediate adhesion and diffusion barrier layer, the surface self-diffusion of the Pt electrode and the influence of the Pt layer on the thermal fusion bonding. An adhesion and diffusion barrier layer between Pt and silicon (Si) is required, since Pt shows a high in-diffusion into Si [154, 155]. A formation of Pt silicides (Pt_2Si and PtSi) at the diffused Pt/Si interface further deteriorates the Pt layer [156]. Several adhesion and diffusion barrier layers have been investigated, among others titanium (Ti), tantalum (Ta) and zirconium (Zr) [157]. The most commonly used Ti should not be employed, since at elevated temperature (450° C), it strongly diffuses into the Pt and, hence, its purpose as an intermediate layer is lost. Furthermore, the resistivity of the Pt layer strongly increases due to electron scattering at the newly formed Pt/Ti interfaces [158]. An additional failure source is imposed by the oxygen (O_2) rich atmosphere during the thermal fusion bonding step. The O_2 itself diffuses through Pt [159] and reacts with the Ti to titanium oxide, causing the electrode to further deteriorate [160]. These problems can be overcome by using Ta instead. First, Ta does not form an eutecticum with Pt, for temperatures below 1635° C and remains as an intermediate layer. It forms during the exposure to O_2 a strong oxide layer underneath the Pt electrode. In addition, Ta also has a sufficiently higher melting temperature (3000° C) [161] than the thermal fusion temperature (1100° C).

Even though the melting temperature of Pt (1772° C) [161] is higher than the thermal fusion temperature, surface self-diffusion of Pt occurs, which deteriorates the electrode [162].

First experiments of a 100 nm thick Pt layer at 1100° C for a 1.5 µm thick SiO_2 layer (5.5 h) demonstrated this strong self-diffusion, resulting in a sponge like electrode, as shown in Fig. 8.1 a). Reducing the temperature to 900° C does not solve the problem, as shown in Fig. 8.1 b), where the resulting SiO_2 layer was reduced to 0.7 µm (7 h). It is assumed that capillary forces support the growth of a groove along the grain boundaries. This problem was addressed by the research of Firebaugh et al. [163], who suggested to use a thick Pt layer (about 1 µm). This should be sufficiently thicker than the equilibrium groove depth and, hence, results in a stable Pt electrode. In their report, a layer of 10 nm Ta and 400 nm Pt, had already an average lifetime of 2881 min at 900° C, where the average lifetime was determined by a 5% increase of electrical resistance. This average life time is more than sufficient to grow the required capillary sidewall of about 1.5 µm SiO_2 at 900° C.

Concerning the thermal fusion bonding quality, the experienced gas built up underneath the Pt electrodes and the resulting non bonded area is not expected, in contrast to what was observed for anodic bonding in chapter 4. The bonding mechanism requires oxygen to form the SiO_2 and, hence, it is in direct contact with the surrounding atmosphere. More critical is the steric hindrance of the thick Pt electrode. Therefore, it is favourable to bury the Pt electrode in a trench to regain a continuously flat bonding surface. So far, the Pt electrode degradation, due to a Pt/SiO_2 interface, is considered the most critical. This interface occurs at the Pt electrode sides and top, since it is required to hydraulically seal the electrode. At this interface, the electrode might degrade, for instance, as competing reaction between the SiO_2 formation and the aforementioned formation of platinum silicide [164].

Herewith, I would like to finish my dissertation thesis and I thank the interested reader for his patience.

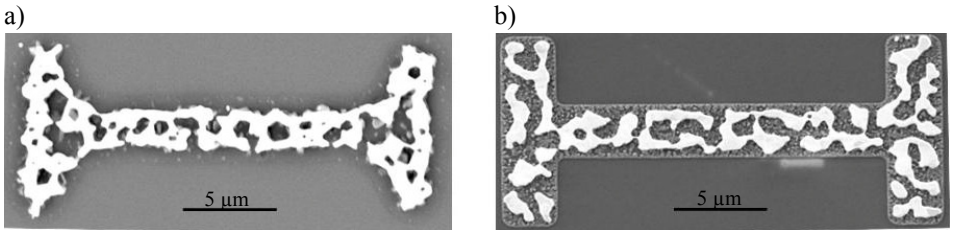

Fig. 8.1 Scanning electron images of a 100 nm thick Pt layer after: a) 5.5 h at 1100° C and b) 7 h at 900° C. Surface self diffusion of Pt deteriorates the electrode, forming a sponge like layer.

References

9.1 Introduction

[1] Barber MA, 1911, A technique for the inoculation of bacteria and other substances into living cells, *The Journal of Infectious Diseases*, **8**, 348-360.

[2] Wingren C and Borrebaeck CAK, 2007, Progress in miniaturization of protein arrays-- a step closer to high- density nanoarrays, *Drug Discovery Today*, **12**, 813-819.

[3] Quate CF, Binning G and Gerber C, 1986, Atomic Force Microscope, *Physics Review Letter*, **56**, 930-933.

[4] Espinosa HD, Moldovan N and Kim KH, 2006, Novel AFM Nanoprobes, Applied scanning probe methods VII, *Springer Berlin Heidelberg*, 77-134.

[5] Piner RD, Zhu J, Xu F, Hong S and Mirkin CA, 1999, Dip-Pen Nanolithography, *Sience*, **283**, 661-663.

[6] Hong S and Mirkin CA, 2000, A Nanoplotter with Both Parallel and Serial Writing Capabilities, *Science*, **288**, 1808-1811.

[7] Jang J, Hong S, Schatz GC and Ratner MA, 2001, Self-assembly of ink molecules in dip-pen nanolithography: A diffusion model, *Journal of Chemical Physics*, **115**, 2721-2729.

[8] Demers LM, Ginger DS, Park SJ, Li Z, Chung SW and Mirkin CA, 2002, Direct Patterning of Modified Oligonucleotides on Metals and Insulators by Dip-Pen Nanolithography, *Science*, **296**, 1836-1838.

[9] Lim JH, Ginger DS, Lee KB, Heo J, Nam JM and Mirkin CA, 2003, Direct-Write Dip-Pen Nanolithography of Proteins on Modified Silicon Oxide Surfaces, *Angewandte Chemie*, **42**, 2309-2312.

[10] Lee KB, Lim JH and Mirkin CA, 2003, Protein Nanostructures formed via Direct-Write Dip-pen Nanolithography, *Journal of the American Chemical Society*, **125**, 5588-5589.

[11] Salaita K, Wang Y and Mirkin CA, 2007, Applications of dip-pen nanolithograpy, Nature nanotechnology, **2**, 145-155.

[12] Huo F, Zheng Z, Zheng G, Giam LR, Zhang H and Mirkin CA, 2008, Polymer Pen Lithography, *Science*, **321**, 1658-1660.

[13] Moldovan N, Kim KH and Espinosa HD, 2006, Design and Fabrication of a Novel Microfluidic Nanoprobe, *Journal of Microelectromechanical Systems*, **15**, 204-212.

[14] Moldovan N, Kim KH and Espinosa HD, 2006, A multi-ink linear array of nanofountain probes, *Journal of Microelectromechanical Systems,* **16**, 1935-1942.

[15] Kim KH, Sanedrin RG, Ho AM, Lee SW, Moldovan N, Mirkin CA and Espinosa HD, 2008, Direct Delivery and Submicrometer Patterning of DNA by a Nanofountain Probe, *Advanced Materials*, **20**, 330-334.

[16] Meister A, Jeney S, Liley M, Akiyama T, Staufer U, de Rooij NF and Heinzelmann H, 2003, Nanoscale dispensing of liquids through cantilevered probes, *Microelectronic Engineering*, **67**, 644-650.

[17] Meister A, Liley M, Brugger J, Pugin R and Heinzelmann H, 2004, Nanodispenser for attoliter volume deposition using atomic force microscopy probes modified by focused-ion-beam milling, *Applied Physics Letters*, **85**, 6260-6262.

[18] Fang A, Dujarin E and Ondharcuhu T, 2006, Control of Droplets Size in Liquid Nanodispensing, *Nanoletters*, **6**, 2368-2374.

[19] Meister A, Krishnamoorthy S, Hinderling C, Pugin R and Heinzelmann H, 2006, Local modification of micellar layers using nanoscale dispensing, *Microelectronic Engineering*, **83**, 1509-1512.

[20] Hug TS, Biss T, de Rooij N and Staufer U, 2005, Generic Fabrication Technology For transparent and suspended microfluidic and nanofluidic channels, *Proceedings 13th Transducers Conference*, 1191-1194.

[21] Deladi S, Berenschot JW, de Boer MJ, Krijnen GJM and Elwenspoek MC, 2004, An AFM-based device for in-situ characterization of nano-wear, *Proceedings 17th MEMS Conferenc*e, 181-184.

[22] Deladi S, Berenschot JW, Tas NR, Krijnen GJM, de Boer JH, de Boer MJ and Elwenspoek MC, 2005, *Journal of Microelectromechanical Systems*, **15**, 528-534.

[23] Meister A, Polesel-Maris J, Niedermann P, Przybylska J, Studer P, Gabi M, Behr P, Zambelli T, Liley M, Voeroes J and Heinzelmann H, 2009, Nanoscale dispensing in liquid environment of streptavidin on a biotin-functionalized surface using hollow atomic force microscope probes, *Microelectronic Engineering*, **86**, 1481-1484.

[24] Meister A, Gabi M, Behr P, Studer P, Voeroes J, Niedermann P, Bitterli J, Polesel-Maris J, Liley M, Heinzelmann H and Zambelli T, 2009, FluidFM: Combining Atomic Force Microscopy and Nanofluidics in a Universal Liquid Delivery System for Single Cell Applications and Beyond, *Nano Letters*, **9**, 2501-2507.

[25] Lewis A, Kheifetz Y, Shambrodt E, Radko A and Khatchatryan E, 1999, Fountain Pen Nanochemistry: Atomic force control of chrome etching, *Applied Physics Letters*, **75**, 2689-2691.

[26] Staemmler L, Suter T and Boehni H, 2002, Glass Capillaries as a Tool in Nanoelectrochemical Deposition, *Electrochemical and Solid-State Letters*, **5**, 61-63.

[27] Akamine S and Quate CF, 1992, Low temperature thermal oxidation sharpening of microcast tips, *Journal of Vacuum Science Technology B*, **10**, 2307-2310.

[28] Korchev YE, Negulyaev YA, Edwards CRW, Vodyanoy I and Lab MJ, 2000, Functional localization of single active ion channels on the surface of a living cell, *Nature cell biology*, **2**, 616-619.

[29] Hamill OP, Marty A, Neher E, Sakmann B and Sigworth FJ, 1981, Improved Patch-Clamp Techniques for High-Resolution Current Recording from Cells and Cell-Free Membrane Patches, *Pfluegers Archive*, **391**, 85-100.

[30] Hansma PK, Drake B, Marti O, Gould SAC and Prater CB, 1989, The scanning Ion-Conductance Microscope, *Science*, **243**, 641-643.

[31] Cong P, Doolen RD, Fan Q, Giaquinta DM, Guan S, McFarland EW, Poorjav DM, Self K, Turner HW and Weinberg WH, 1999, High-Throughput Synthesis and Screening of Combinatorial Heterogeneous Catalyst Libraries, *Angewandte Chemie Internationale Edition*, **38**, 483-488.

[32] Jambunathan K and Hillier AC, 2003, Measuring Electrocatalytic Activity on a Local Scale with Scanning Differential Electrochemical Mass Spectrometry, *Journal of the Electrochemical Society*, **150**, 312-320.

[33] Braun T, Barwich V, Ghatkesar MK, Bredekamp AH, Gerber C, Hegner M and Lang HP, 2005, Micromechanical mass sensors for biomolecular detection in a physiological environment, *Physical Review E*, **72**, 031907.

[34] Burg TP and Manalis SR, 2003, Suspended microchannel resonators for biomolecular detection, *Applied Physics Letters*, **83**, 2698-2700.

[35] Burg TP, Godin M, Knudsen SM, Shen W, Carlson G, Foster JS, Babcock K and Manalis SR, 2007, Weighing of biomolecules, single cells and single nanoparticles in fluid, *Nature*, **446**, 1066-1069.

[36] Woolley AT, Lao K, Glazer AN and Mathies RA, 1998, Capillary Electrophoresis Chips with Integrated Electrochemical Detection, *Analytical Chemistry*, **70**, 684-688.

[37] Pai RS, Walsh KM, Crain MM, Roussel TJ, Jackson DJ, Baldwin RP, Keynton RS and Naber JF, 2009, Fully Integrated Three-Dimensional Electrodes for Eletrochemical Detection in Microchips: Fabrication, Characterization, and Application, *Analytical Chemistry*, **81**, 4762-4769.

[38] Bratten CDT, Cobbold PH and Cooper JM, 1997, Micromachining Sensors for Electrochemical Measurements in Subnanoliter Volumes, *Analytical Chemistry*, **69**, 253-258.

[39] Firebaugh SL, Jensen KV and Schmidt MA, 1998, Investigation of High-Temperature Degradation of Platinum Thin Films with an In Situ Resistance Measurement Apparatus, *Journal of Micromechanical Systems*, **7**, 128-135.

[40] Janz GJ and Ives DJG, 1968, Silver Silver Chloride Electrodes, *Annals of the New York Academy of Science*, **148**, 210-221.

[41] Bruus H, 2008, Theoretical Microfluidics, *Oxford University Press*.

[42] Zhou MX and Foley JP, 2006, Quantitative Theory of Electroosmotic Flow in Fused-Silica Capillaries Using an Extended Site-Dissociation-Site-Binding Model, *Analytical Chemistry*, **78**, 1849-1858.

[43] Morf WE, Guenat OT and de Rooij NF, 2001, Partial electroosmotic pumping in complex capillary systems Part 1: Principles and general theoretical approach, *Sensors and Actuators B*, **72**, 266-272.

[44] Stern OZ, 1924, The theory of the electrolytic double layer, *Zeitschrift fuer Elektrochemie und Angewandte Physikalische Chemie*, **30**, 508-516.

[45] Meyer E, 1992, Atomic Force microscopy, Progress in Surface Science, **41**, 3-49.

[46] Giessibl FJ, 2003, Advances in atomic force microscopy, *Reviews of modern physics*, **75**, 949-978.

[47] Frederix PLTM, Akiyama T, Staufer U, Gerber Ch, Fotiadis D, Mueller DJ and Engel A, 2003, Atomic force bio-analytics, *Current Opinion in Chemical Biology*, **5**, 641-647.

[48] Quate CF, 1994, The AFM as a tool for surface imaging, *Surface Science*, **299**, 980-995.

[49] Madou MJ, 2002, Fundamentals of Microfabrication, 2nd edition, *CRC Press*.

[50] Franssila S, 2004, Introduction into Microfabrication, *Wiley*.

[51] May GS and Sze SM, 2004, Fundamentals of Semiconductor Processing, *Wiley*.

9.2 Fabrication of the scanning ion pipette

[52] Hug TS, Biss T, deRooij NF and Staufer U, 2005, Generic fabrication technology for transparent and suspended microfluidic and nanofluidic channels, *In Digest of Technical Papers, Transducers'05*, **2**, 1191-1194.

[53] Hug TS, deRooij NF, and Staufer U, 2006, Fabrication and electroosmotic flow measurements in micro- and nanofluidic channels, *Microfluid Nanofluid*, **2**, 117-124.
[54] Frederix PLTM, Akiyama T, Staufer U, Gerber Ch, Fotiadis D, Mueller DJ and Engel A, 2003, Atomic force bio-analytics, *Current Opinion in Chemical Biology*, **5**, 641-647.
[55] Franssila S, 2004, Introduction into Microfabrication, *Wiley*.
[56] Meyer E, 1992, Atomic Force microscopy, Progress in Surface Science, **41**, 3-49.
[57] Deal BE and Grove AS, 1965, General Relationship for the Thermal Oxidation of Silicon, *Journal of Applied Physics*, **36**, 3770-3778.
[58] Madou MJ, 2002, Fundamentals of Microfabrication, 2nd edition, *CRC Press*.
[59] Seidel H, Csepregi L, Heuberger A and Baumgaertel H, 1990, Anisotropic Etching of Crystalline Silicon in Alkaline Solutions, Part 1, *Journal of Electrochemical Society*, **137**, 3612-3626.

9.3 Evaporation induced pumping within the scanning ion pipette

[60] Namasivayam V, Larson RG, Burke DT and Burns MA, Transpiration-based micropump for delivering continuous ultra-low flow rates. *J. Micromechanics and Microengineering,* 2003, **13,** 261-271.
[61] Lynn NS and Dandy DS, Passive microfluidic pumping using coupled capillary/ evaporation effects. *Lab on Chip*, 2009, **9**, 3422-3429.
[62] Zimmermann M, Bentley S, Schmid H, Hunziker P and Delamarche E, Continuous flow in open microfluidics using controlled evaporation. *Lab on a Chip*, 2005, **5**, 1355-1359.
[63] Walker GM and Beebe DJ, An evaporation-based microfluidic sample concentration method. *Lab on a Chip*, 2002, **2**, 57-61.
[64] Goedecke N, Eijkel J and Manz A, Evaporation driven pumping for chromatographic application. *Lab on a Chip*, 2002, **2**, 219-223.
[65] Bird R, Steward W and Lightfoot E, Transport Phenomena, *Wiley*, 1960.
[66] Weast RC, Astle MJ and Beyer WH, 1988, CRC Handbook of Chemistry, 68th edition, *CRC Press*.
[67] Gates DM, Biophysical Ecology, *Springer*, 1980.

9.4 Electroosmotic pumping with Pt electrodes

[68] Brask A, Kutter JP and Bruus H, 2005, Long-term stable electroosmotic pump with ion exchange membranes, *Lab on Chip*, **5**, 730-738.
[69] Hug TS, de Rooij NF and Staufer U, 2005, Fabrication and electroosmotic flow measurements in micro- and nanofluidic channels, *Microfluid Nanofluid*, **2**, 117-124.
[70] Takamura Y, Onoda H, Inokuchi H, Adachi S, Oki A and Horiike Y, 2003, Low-voltage electroosmosis pump for stand-alone microfluidics devices, *Electrophoresis*, **24**, 185-192.
[71] Guenther A, Jhunjhunwala M, Thalmann M, Schmidt MA and Jensen KF, 2005, Micromixing of Miscible Liquids in Segmented Gas-Liquid Flow, *Langmuir*, **21**, 1547-1555.
[72] Jensen MJ, Goranovic G and Bruus H, 2004, The clogging pressure of bubbles in hydrophilic microchannel contractions, *Journal of Micromechanics and Microengineering*, **14**, 876-883.
[73] Paust N, Litterst C, Metz T, Eck M, Ziegler C, Zengerle R and Koltay P, 2009, Capillary-driven pumping for passive degassing and fuel supply in direct methanol fuel cells, *Microfluid Nanofluid*, **7**, 531-543.

[74] Han A, Mondin G, Hegelbach NG, de Rooij, NF and Staufer U, 2006, Filling kinetics of liquids in nanochannels as narrow as 27 nm by capillary force, *Journal of Colloid and Interface Science*, **293**, 151-157.

[75] Madou MJ, 2002, Fundamentals of Microfabrication, 2nd edition, *CRC Press*.

[76] Lee TMH, Lee DHY, Liaw CYN, Lao AIK, Hsing IM, 2000, Detailed characterization of anodic bonding process between glass and thin-film coated silicon substrates, *Sensors and Actuators A*, **86**, 103-107.

[77] Plaza JA, Esteve J and Lora-Tamayo E, 1998, Effect of silicon oxide, silicon nitride and polysilicon layers on the electrostatic pressure during anodic bonding, *Sensors and Actuators A*, **67**, 181-184.

[78] White FM, 1999, Fluid Mechanics, 4th edition, *McGraw-Hill*.

[79] Coury L, 1999, Conductance Measurements Part 1: Theory, *Current Separations*, **18,** 91-96.

[80] Zhou MX and Foley JP, 2006, Quantitative Theory of Electroosmotic Flow in Fused-Silica Capillaries Using an Extended Site-Dissociation-Site-Binding Model, *Analytical Chemistry*, **78**, 1849-1858.

[81] Wang P, Chen Z and Chang HC, 2006, A new electro-osmotic pump based on silicamonoliths, *Sensors and Actuators B*, **113**, 500-509.

[82] Hubin A and Vereecken J, 1994, Electrochemical reduction of silver thiosulfate complexes Part I: Thermodynamic aspects of solution composition, *Journal of Applied Electrochemistry*, **24**, 239-244.

[83] Hubin A and Vereecken J, 1994, Electrochemical reduction of silver thiosulfate complexes Part II: Mechanism and Kinetics, *Journal of Applied Electrochemistry*, **24**, 396-403.

[84] Vandeputte S, Verboom E, Hubin A and Vereecken J, 1995, Silver reduction in a thiosulfate + nitrate solution: study of a CE reaction scheme by means of polarization curves and ac impedance, *Journal of Electroanalytical Chemistry*, **397**, 249-260.

9.5 Integration of Ag electrodes into the scanning ion pipette

[85] Xia Y, Venkateswaran N, Qin D, Tin J and Whitesides GM, 1998, Use of Electroless Silver as the Substrate in Microcontact Printing and its Application in Microfabrication, *Langmuir*, **14**, 363-371.

[86] Yin Y, Li Z, Zhong Z, Gates B, Xia Y and Venkateswaran S, 2002, Synthesis and characterization of stable aqueous dispersions of silver nanoparticles through the Tollens process, *Journal of Materials Chemistry*, **12**, 522-527.

[87] Saito Y, Wang JJ, Batchelder DN and Smith DA, 2003, Simple Chemical Method for Forming Silver Surfaces with Controlled Grain Sizes for Surface Plasmon Experiments, *Langmuir*, **19**, 6857-6861.

[88] Kvitek L, Prucek R, Panacek A, Novotny R, Hrbac J and Zboril R, 2005, The influence of complexing agent concentrations on particle size in the process of SERS active silver colloid synthesis, *Journal of Materials Chemistry*, **15**, 1099-1105.

[89] Formanek F, Takeyasu N and Tanaka T, 2006, Selective electroless plating to fabricate complex three-dimensional metallic micro/nanostructures, *Applied Physics Letters*, **88**, 205-209.

[90] Kenis PJA, Ismagilov RF, Takayama S and Whiteside GM, 1999, Microfabrication Inside Capillaries Using Multiphase Laminar Flow Patterning, *Science*, **285**, 83-85.

[91] Allen PB, Rodriquez I, Kuyper CL, Lorenz RM, Spicar-Mihalic P, Kuo JS and Chiu DT, 2003, Selective Electroless and Electrolytic Deposition of Metal for Applications in Microfluidics: Fabrication of a Microthermocouple, *Analytical Chemistry*, **75**, 1578-1583.

[92] Goluch ED, Shaikh KA, Ryu K, Chen J, Engel J and Liu C, 2004, Microfluidic method for in-situ deposition and precision patterning of thin-film metals on curved surfaces, *Applied Physics Letters*, **85**, 3629-3631.

[93] Bogush V, Inberg A, Croitoru N, Dubin V and Shacham-Diamand Y, 2003, Electroless deposition of novel Ag-W thin films, *Microelectronic Engineering*, **70**, 489-494.

[94] Shacham-Diamand Y, Inberg A, Sverdlov Y, Bogus V, Croitoru N, Moscovich H and Freeman A, 2003, Electroless processes for micro- and nanoelectronics, *Electrochimica Acta*, **48**, 2987-2996.

[95] Liu Z, He Q, Xiao P, Liang BO, Tan J, He N and Lu Z, 2003, Self-assembly monolayer of mercaptopopyltrimethoxysilane for electroless deposition of Ag, *Materials Chemistry and Physics*, **82**, 301-305.

[96] Cho JH, Lim JA and Han JT, 2005, Control of the electrical and adhesion properties of metal/organic interfaces with self-assembled monolayers, *Applied Physics Letters*, **86**, 171906.

[97] Freeman RG, Grabar KC, Allison KJ, Bright RM, Davis JA, Guthrie AP, Hommer MB, Jackson MA, Smith PC, Walter DG and Nathan MJ, 1995, Self-Assembled Metal Colloid Monolayers: An Approach to SERS Substrates, *Langmuir*, **267**, 1629-1631.

[98] Hajdukova N, Prochazka M, Stepanek J and Spirkova MA, 2007, Chemically reduced and laser-ablated gold nanoparticles immobilized to silanized glass plates: Preparation, characterization and SERS spectral testing, *Colloids and Surfaces A: Physiochemical Engineering Aspects*, **301**, 264-270.

[99] Menzel H, Mowery MD, Cai M and Evans CE, 1999, Surface-Confined Nanoparticles as Substrates for Photopolymerizable Self-Assembled Monolayers, *Advanced Materials*, **11**, 131-134.

[100] Cheng W, Dong S and Wang E, 2002, Gold Nanoparticles as Fine Tuners of Electrochemical Properties of the Electrode/Solution Interface, *Langmuir*, **18**, 9947-9952.

[101] Hooper AE, Werho D, Hopson T and Palmer O, 2001, Evaluation of amine- and amide-terminated self-assembled monolayers as Molecular glues for Au and SiO_2 substrates, *Surface and Interface Analysis*, 809-814.

[102] Goss CA, Charych DH and Majda M, 1991, Application of (3-Mercaptopropyl)trimethoxysilane as a Molecular Adhesive in the Fabrication of Vapor-Deposited Gold Electrodes on Glass Substrates, *Analytical Chemistry*, **63**, 85-88.

[103] Doron A, Katz E and Willner I, 1995, Organization of Au Colloids as Monolayer Films onto ITO Glass Surfaces: Application of the Metal Colloid Films as Base Interfaces To Construct Redox-Active Monolayers, *Langmuir*, **11**, 1313-1317.

[104] Rye RR, Nelson GC and Dugger MT, 1997, Mechanistic Aspects of Alkylchlorosilane Coupling Reactions, *Langmuir*, **13**, 2965-2972.

[105] Ledung G, Bergkvist M, Quist AP, Gelius U, Carlsson J and Oscarsson S, 2001, A Novel Method for Preparation of Disulfides on Silicon, *Langmuir*, **17**, 6056-6058.

[106] Hong H, Jiang M, Sligar SG and Bohn PW, 1994, Cysteine -Specific Surface Tethering of Genetically Engineered Cytochromes for Fabrication of Metalloprotein Nanostructures, *Langmuir*, **10**, 153-158.

[107] Haller I, 1978, Covalently Attached Organic Monolayers on Semiconductor Surfaces, *Journal of the American Chemical Society*, 8050-8055.

[108] Schneider S, Halbig P, Grau H and Nickel U, 1994, Reproducible preparation of silver sols with uniform particle size for applications in surface-enhanced Raman spectroscopy, *Photochemistry and Photobiology*, **60**, 605-610.

[109] Shirtcliffe N, Nickel U and Schneider S, 1999, Reproducible Preparation of Silver Sols with Small Particle Size Using Borohydride Reduction: For Use as Nuclei for Preparation of Larger Particles, *Journal of Colloid and Interface Science*, **211**, 122-129.

[110] Tong H, Zhu L, Li M and Wang C, 2003, Electroless silver deposition on Si(100) substrate based on the seed layer of silver itself, *Electrochimica Acta*, **48**, 2473-2477.

[111] Zhang Q, Wu M and Zhao W, 2005, Electroless nickel plating on hollow glass microspheres, *Surface & Coatings Technology*, **192**, 213-219.

[112] Li J, Tian Y, Huang Z and Zhang X, 2006, Studies of the porosity in electroless nickel deposits on magnesium alloy, *Applied Surface Science*, **252**, 2839-2846.

[113] Barger MS and White WB, 1991, The Daguerreotype, *Simthsonian Institution Press*.

[114] Hilmi A and Luong JHT, 2000, Electrochemical Detectors Prepared by Electroless Deposition for Microfabricated Electrophoresis Chips, *Analytical Chemistry*, **72**, 4677-4682.

[115] Pillai ZS and Kamat PV, 2004, What Factors Control the Size and Shape of Silver Nanoparticles in the Citrate Ion Reduction Method?, *Journal of Physical Chemistry B*, **108**, 945-951.

[116] Atkins PW and Beran JA, 1992, General Chemistry, *Freeman and Company press*, 2nd edition.

[117] Man PF, Mastrangelo CH, Burns MA and Burke DT, 1998, Microfabricated capillarity-driven stop valve and sample injector, *MEMS'98*, 45-50.

[118] Egidi G, Herrera F, Moreno-Bondim MC, Kempe M, van Rhijn JA, Fiaccabrino GC and de Rooij NF, 2003, Fabrication and characterization of stop flow valves for fluid handling, *Transducers'03*, 147-150.

[119] Leu T and Chang P, 2004, Pressure barrier of capillary stop valves in micro sample separators, *Sensor and Actuators A*, **115**, 508-515.

[120] Melin J, Roxhed N, Gimenez G, Griss P, van der Wijngaart W and Stemme G, 2004, A liquid-triggered liquid microvalve for on-chip flow control, *Sensors and Actuators B*, **100**, 463-468.

[121] Gliere A and Delattre C, 2006, Modelling and fabrication of capillary stop valves for planar microfluidic systems, *Sensor and Actuators A*, **130-131**, 601-608.

[122] Zimmermann M, Hunziker P and Delamarche E, 2008, Valves for autonomous capillary systems, *Microfluid Nanofluid*, **5**, 395-402.

[123] Matula RA, 1979, Electrical-resistivity of Copper, Gold, Palladium and Silver, *Journal of Physical and Chemical Reference Data*, **8**, 1147-1298.

[124] Weislogel MM and Lichter S, 1998, Capillary flow in an interior corner, *Journal of Fluid Mechanics*, **373**, 349-378.

[125] Goldschmidtboeing F, Rabold M and Woias P, 2006, Strategies for void-free liquid filling of micro cavities, *Journal of Micromechanics and Microengineering*, **16**, 1321-1330.

9.6 Electroosmotic pumping and electrochemical sensing with Ag/AgCl electrodes

[126] Janz GJ and Ives DJG, 1968, Silver Silver Chloride Electrodes, *Annals of the New York Academy of Science*, **148**, 210-221.

[127] Suzuki H, Hirakawa T, Sasaki S and Karube I, 1999, An integrated three-electrode system with a micromachined liquid-junction Ag/AgCl reference electrode, *Analytica Chimica Acta*, **387**, 103-112.

[128] Miessner U, Lindken R and Westerweel J, 2008, 3D - Velocity measurements in microscopic two-phase flows by means of micro PIV, *14th Symposium of Laser Techniques to Fluid Mechanics.*

[129] Morf WE, Guenat OT and de Rooij NF, 2001, Partial electroosmotic pumping in complex capillary systems Part 1: Principles and general theoretical approach, *Sensors and Actuators B*, **72**, 266-272.

[130] Huo F, Zheng Z, Zheng G, Giam LR, Zhang H and Mirkin CA, 2008, Polymer Pen Lithography, *Science*, **321**, 1658-1660.

[131] Trautmann A, Heuck F, Mueller C, Ruther P and Paul O, 2005, Replication of microneedle arrays using vacuum casting and hot embossing, *Proceedings Tranducers conference*, 1420-1423.

[132] Zhao XM, Xia Y and Whiteside GM, 1997, Softlithography methods for nano-fabrication, *Journal of Material Chemistry*, **7**, 1069-1074.

[133] Dupont EP, Luisier R and Gijs MAM, 2010, NOA 63 as a UV-curable material for fabrication of microfluidic channels with native hydrophilicity, *Microelectronic Engineering,* **87**, 1253-1255.

[134] Kim SH, Yang Y, Kim M, Nam SW, Lee KM, Leen NY, Kim YS and Park S, 2007, Simple Route to Hydrophilic Microfluidic Chip Fabrication Using and Ultraviolet (UV)-Cured Polymer, *Advanced Functional Materials*, **17**, 3493-3498.

[135] Atkins PW and Beran JA, 1992, General Chemistry, *Freeman and Company press*, 2nd edition.

[136] Cain LS and Slifkin LM, 1980, Ionic Conductivity of mixed silver halide crystals, *Journal of Physics and Chemistry of Solids,* **2**, 173-178.

[137] Polk BJ, Stelzenmueller A, Mijares G, MacCrehan W and Gaitan M, 2006, Ag/AgCl microelectrodes with improved stability for microfluidics, *Sensors and Actuators B*, **114**, 239-247.

[138] Kenis PJA, Ismagilov RF, Takayama S and Whiteside GM, 2000, Fabrication inside Microchannels Using Fluid Flow, *Accounts of Chemical Research*, **33**, 841-847.

[139] Goluch ED, Shaikh KA, Ryu K, Chen J, Engel J and Chang L, 2004, Microfluidic method for in-situ deposition and precision pattering of thin-film metals on curved surfaces, *Applied Physics Letters*, **85**, 3629-3631.

[140] Corish J and Jacobs PWM, 1975, An Analysis of models for the Ionic Conductivity of Silver Chloride, *Physica Status Solidi*, **67**, 263-272.

[141] Deal BE and Grove AS, 1965, General Relationship for the Thermal Oxidation of Silicon, *Journal of Applied Physics*, **36**, 3770-3778.

[142] Bohl B, Steger R, Zengerle R and Koltay P, 2005, Multi-layer Su-8 lift-off technology for microfluidic devices, *Journal of Micromechanics and Microengineering*, **15**, 1125-1130.

[143] Scales PJ, Grieser F and Healy TW, 1992, Electrokinetics of the Silica-Solution Interface: A Flat Plate Streaming Potential Study, *Langmuir*, **8**, 965-974.

[144] Voigt A, Wolf H, Lauckner S, Neumann G, Becker R and Richter L, 1983, Electrokinetic properties of polymer and glass surfaces in aqueous solutions: Experimental evidence for swollen surface layers, *Biomaterials*, **4**, 299-304.

[145] Kirby BJ and Hasselbrink EF, 2004, Zeta potential of microfluidic substrates: 2. Data for polymers, *Electrophoresis*, **25**, 203-213.

[146] Kaelble DH, 1970, Dispersion-Polar surface tension properties of organic solids, *The Journal of Adhesion*, **2**, 66-81.

[147] Owens DK and Wendt RC, 1969, Estimation of the surface free energy of polymers, *Journal of Applied Polymer Science*, **13**, 1741-1747.

[148] Behrens SH, Christl DI, Emmerzael R, Schurtenberger P and Borkovec M, 2000, Charging and Aggregation Properties of Carboxyl Latex Particles: Experiments versus DLVO Theory, *Langmuir*, **16**, 2566-2575.

9.7 Imaging and dispensing with the scanning ion pipette

[149] Meister A, Gabi M, Behr P, Studer P, Voeroes J, Niedermann P, Bitterli J, Polesel-Maris J, Liley M, Heinzelmann H and Zambelli T, 2009, FluidFM: Combining Atomic Force Microscopy and Nanofluidics in a Universal Liquid Delivery System for Single Cell Applications and Beyond, *Nano Letters*, **9**, 2501-2507.

[150] de Boer MJ, Tjerkstra RW, Berenschot JWE, Jansen HV, Burger GJ, Gardeniers JGE, Elwenspoek M and van den Berg, 2000, Micromachining of Buried Micro Channels in Silicon, *Journal of Microelectromechanical Systems*, **9,** 94-104.

[151] Bhattacharya S, Datta A, Berg JM and Gangopadhyay S, 2005, Studies on Surface Wettability of Poly(Dimethyl)Siloxane (PDMS) and Glass Under Oxygen-Plasma Treatment and Correlation With Bond Strength, *Journal of Microelectromechanical Systems*, **14,** 590-597.

9.8 Conclusions and recommendations

[152] Hug TS, Biss T, deRooij NF and Staufer U, 2005, Generic fabrication technology for transparent and suspended microfluidic and nanofluidic channels, *In Digest of Technical Papers, Transducers'05*, **2**, 1191-1194.

[153] Man PF, Mastrangelo CH, Burns MA and Burke DT, 1998, Microfabricated capillarity-driven stop valve and sample injector, *MEMS'98*, 45-50.

[154] Prabhakar A, McGill TC and Nicolet MA, 1983, Platinum diffusion into silicon from PtSi, *Applied Physics Letters*, **43**, 1118-1120.

[155] Mantovani S, Nava F, Nobili C and Ottaviani G, 1986, In-diffusion of Pt in Si from the Pt/Si/Si interface, *Physical Review B*, **33**, 5536-5544.

[156] Larrieu G, Dubois E, Wallart X, Baie X and Katcki J, 2003, Formation of platinum-based silicide contacts: Kinetics, stoichiometry, and current drive capabilities, *Journal of Applied Physics*, **94**, 7801-7810.

[157] Maeder T, Sagalowicz and Muralt P, 1998, Stabilized Platimum Electrodes for Ferroelectric Film Deposition using Ti, Ta and Zr Adhesion Layers, *Japanese Journal of Applied Physics*, **37**, 2007-2012.

[158] Schmid U and Seidel H, 2008, Effect of high temperature annealing on the electrical performance of titanium/platinum thin films, *Thin Solid Films*, **516**, 898-906.

[159] Schmiedl R, Demuth V, Lahnor P, Godehardt H, Bodschwinna Y, Harder C, Hammer L, Strunk HP, Schulz M and Heinz K, 1996, Oxygen diffusion through thin Pt films on Si(100), *Applied Physics A*, **62**, 223-230.

[160] Sreenivas K, Reaney I, Maeder T and Setter N, 1994, Investigation of Pt/Ti bilayer metallization on silicon for ferroelectric thin film investigation, *Journal of Applied Physics*, **75**, 232-239.

[161] Atkins PW and Beran JA, 1992, General Chemistry, *Freeman and Company press*, 2nd edition.

[162] Kellogg GL, 1991, Temperature dependence of surface self-diffusion on Pt(001), *Surface Science*, **246**, 31-36.

[163] Firebaugh SL, Jensen KV and Schmidt MA, 1998, Investigation of High-Temperature Degradation of Platinum Thin Films with an In Situ Resistance Measurement Apparatus, *Journal of Micromechanical Systems*, **7**, 128-135.

[164] Wang D, Penner S, Su DS, Rupprechter G, Hayek K and Schloegl R, 2003, Silicide formation on a Pt/SiO_2 model catalyst studied by TEM, EELS and EDXS, *Journal of Catalysis*, **219**, 434-441.

Summary

In this thesis, sub-10 µm fluidic systems with integrated electrodes for pumping and sensing in nanotechnology applications were developed and analyzed. This work contributes to the development of the scanning ion pipette (SIP), a tool to investigate surface changes on the nanometer scale induced by locally administering chemically or bio-active solutions. For this purpose, the already existing technology of a micropipette integrated into a scanning force microscope (SFM)-chip was enhanced by the use of electrodes for on-chip electrochemical sensing and electroosmotic (EO) pumping. The integration of an EO pump offered the possibility of storing, selecting and dispensing multiple different liquids with the SIP chip. For a high density and convenient electronic integration, an EO pump with a small footprint (less than 100 µm × 100 µm) and low actuation voltage (less than 10 V) had to be developed.

The thesis starts with a detailed analysis of the microfabrication process to build the SIP's network of capillaries, the freestanding cantilever and the tip. The fabrication was based on standard micromachining, from well established MEMS processes. The main innovation, previously developed by Hug et al., was to outline the capillaries of the fluidic system, the cantilever and the tip in one wafer, and fabricating the fluidic through wafer connections and the SIP chip outline in another wafer. By bonding the two wafers together, the former trenches were capped and by a subsequent high temperature oxidation, the hydrophilic silicon dioxide (SiO_2) capillaries were formed. Afterwards, the buried fluidic system and the cantilever were released, providing optical access to the capillaries. Finally, the outlet hole was drilled next to the tip apex with a focussed ion beam. This SIP fabrication process was highly versatile with regards to the capillary geometry, allowing the design of a complex capillary geometry for a multifunctional microfluidic system.

To obtain a first experience with these small capillary dimensions, the integration of an evaporation based micropump into the SIP was investigated. Its actuation did not require any electrodes and hence, it could be directly implemented into the SIP fabrication process, without any additional fabrications steps. The working principle of an evaporation based micropump is as follows: The hydrophilic capillaries of the SIP were spontaneously filled with a water based solution. Once the fluid reached the capillary outlet inside, it started evaporating. The capillary pressure kept the outlet of the capillaries wetted, and thereby, automatically replaced the evaporation loss by drawing additional water through the capillaries. This resulted in a unidirectional pump, which could be controlled by the temperature at the evaporation area. The evaporation induced flowrate was experimentally determined to range from 7 $pl \cdot s^{-1}$ at 23° C up to 53 $pl \cdot s^{-1}$ at 65° C depending exponentially on the temperature.

A more advanced bidirectional EO pump with platinum (Pt) electrodes, based on a simplified fabrication process, resulting in comparable SIP capillary dimensions, was experimentally analyzed and modelled. The current-coupling between the Pt electrodes and the solution required a SIP specific on-chip design to ventilate the emerging electrolyzed

gases. This was achieved by integrating the electrodes into a novel liquid-gas (LG) separator. The LG-separator separated the gas bubbles from the liquid and guided them away from the EO pump. Its operation principle is solely based on the LG-separator's geometry of tapered sidewalls, taking advantage of the high capillary pressure occurring at the bubble's liquid gas interfaces at this small scale. The LG-separator was experimentally analyzed and modelled. In the experimental analysis, the maximum backpressure of the LG-separator was determined to be 0.6 kPa. It was able to reliably separate and ventilate an emerging gas flow of 2 $pl \cdot s^{-1}$. For a deeper understanding, the development and the propagation of the bubble within the LG-separator was analytically described in three dimensions. The model and the derived design guidelines show that Pt electrodes, combined with the LG-separator, open an interesting new field for complex high density electrohydrodynamic and electrochemical microfluidic applications. A microfluidic system, containing two LG-separators sandwiching an EO pump, was also analyzed and modelled. The EO pump achieved a flow rate of 50 $pl \cdot s^{-1}$ at a low actuation voltage of 5 V. The developed corresponding model of the flows within the fluidic system was in good agreement with the measured values. According to the model, an EO pump with a high backpressure (3.6 $kPa \cdot V^{-1}$) enabling a high dispensing flowrate of 1.5 $pl \cdot V^{-1} \cdot s^{-1}$ (corresponding to a SIP immersed in water, outlet hole radius of 100 nm) can be built.

The performance and integration of a second type of electrodes, based on silver/silver chloride (Ag/AgCl), into the SIP was investigated. These electrodes had the outstanding advantage that during electrode actuation the electrochemical reaction continued to transform Ag into AgCl and vice versa, rather than electrolyzing the liquid. Moreover, these electrodes could be integrated in a post SIP capillary fabrication step, circumventing electrode instability caused by the high temperature oxidation step to form the SiO_2 of the capillary sidewalls. The general processflow to integrate the Ag/AgCl electrodes into the fabricated SIP capillary fabrication step was:

1. The adhesion of the Ag electrode to the SiO_2 capillary sidewall was improved by using an intermediate polymeric layer consisting of 3-mercaptopropylmethyldimethoxy silane (MPS). This silanization step turned out to be essential for reliably stable Ag electrodes in a capillary dimension of less than 10 µm, since the strong capillary force tended to delaminate the electrode. Crucial for a successful silanization was the use of a gas phase deposition on a dehydrated surface, to avoid the formation of polymeric MPS globuly.
2. Electroless deposition provided a highly flexible and unique tool to deposit the electrodes in the closed SIP capillaries. The general idea was to fill a solution of Ag ions, as well as a reducing agent into the capillary. During the electrochemical reaction, the Ag electrodes started to grow on the capillary sidewall. The deposition of thick electrodes was required since during the electrode actuation, either Ag or AgCl was continuously consumed. This deposition of thick electrodes was especially challenging due to a minute available capillary volume, hence high concentrations within the electroless solution were used. The best electroless deposition process control was achieved with an improved Tollens solution and the reaction speed was controlled with the sodium citrate concentration (decrease) and the sodium hydroxide concentration (increase). Two different methods of electroless deposition were employed: First, a batch-like dip process of multiple electroless depositions, and second, a single electrode flow deposition process providing continuously fresh electroless solution.
3. The electrode structuring was performed by controlling the capillary filling of the electroless solution within the fluidic system by microfluidic stopvalves. The stopvalve

functionality was twofold, the solution was reliably stopped during the electroless deposition and afterwards the stopvalve was void free filled to ensure correct fluidic actuation of the final device. This should be done preferably without applying any external pressure. The switching from stopping to transmitting the solution was induced by a change in the solution's surface tension. The stopvalve performance was modelled by improving the previously two dimensional model to three dimensions including, additionally, the design fabrication specific corner rounding and low capillary cross section's aspect ratio.

4. After the electroless deposition and structuring, the Ag electrode was further transformed into an Ag/AgCl electrode. Similarly to the electroless Ag deposition, the electrode transformation was performed with a flow of either sodium hypochloride or ferric(III) chloride. The transformation should be limited to 20% of the initial Ag layer thickness, due to stress related electrode delamination or cracking, originating in the density difference of Ag and AgCl. Interestingly, the electrochemical transformation process from Ag into AgCl could be described by the Deal-Grove model for the oxidation of silicon. The growth of AgCl depended nonlinearly on electrochemical reaction time. After an AgCl thickness of about 40 nm, the electrochemical reaction was dominated by the diffusion of the oxidizing species through an increasing layer of AgCl.

Electrodes were deposited into three different capillaries: a) into the SIP capillary itself (cross section 2.2 µm × 3.7 µm), b) for larger availability and easier accessibility, into commercially available round capillaries (radius up to 520 µm), and c) a polymeric microfluidic system with rectangular capillaries (cross section 55 µm × 65 µm). Inside the SIP, the functionality of the microfluidic stopvalve was experimentally verified, a binary solution of 20% ethanol in water (contact angle 82°) was stopped and a binary solution of 40% ethanol in water (contact angle 58°) filled the stopvalve void free. In addition, a successful dip electroless deposition and stopvalve structuring of Ag electrodes was shown. Inside round capillaries, multiple electroless depositions revealed that each deposition increased the Ag layer thickness of 51 nm. The deposited Ag layer had a high specific conductivity of 6×10^7 S·m^{-1}, indicating a high purity and density. The further transformation into Ag/AgCl provided electrodes to electrochemically measure different pH values. A linear pH sensitivity of 57.4 mV·pH^{-1} at 22.7° C with a good agreement of Nernstian behavior was reached. During these experiments, it turned out that the electroless Ag deposition was highly contamination sensitive which was strongly enhanced by the small capillary cross section. Therefore, the deposition into the polymeric fluidic system was performed with a flow of electroless solution instead of previously used multiple depositions. Despite the individual electrode deposition, the flow deposition had the advantage that the concentration could be kept constant throughout the capillary during the complete deposition time. This provided a better reaction control due to a lower concentration and in addition, it reduced the effect of the minute available capillary volume. The EO pump inside the polymeric fluidic system had an experimentally determined pump rate of 0.12 nl·s^{-1}·V^{-1}.

First, experiments with the SIP for imaging and dispensing were performed. In order to get a first hand-on experience, a less delicate sample, in less challenging conditions, was chosen, then anticipated for the expected SIP imaging of a living cell. The imaging capabilities were illustrated by imaging in tapping mode a fixed and dried Escherichia Coli bacteria. The obtained images had a reasonable image quality and resolution. Moreover, no special skills in handling the SFM were required, since it did not perform differently with a mounted SIP than with a mounted standard commercially available SFM. In case of

dispensing, with an externally applied pressure, the development of a bubble at the outlet hole of the tip was observed. With the currently used method of gluing the SIP to the SFM holder, no satisfying and reliable mounting was achieved. The main reasons of failure were leakage afflicted sealing between the SIP and the SFM holder, contamination of the SIP capillaries and finally breaking of the SIP cantilever during the complex and lengthy mounting procedure. This, again, shows the necessity of improving SIP techniques towards autonomous on-chip fluid handling.

Samenvatting

In dit proefschrift zijn micro-fluïdische systemen in het bereik onder 10 µm ontwikkeld en geanalyseerd met geïntegreerde elektroden voor het pompen en aftasten in nanotechnologische toepassingen. Dit werk levert een bijdrage aan de ontwikkeling van de scanning ion pipette (SIP), een apparaat voor het onderzoeken van oppervlakteveranderingen op nanometerschaal veroorzaakt door lokaal aangebrachte chemische of bioactieve oplossingen. Voor dit doel is de bestaande technologie van een in een scanning force microscope (SFM)-chip geïntegreerde micropipet verder ontwikkeld door toepassing van elektroden voor on-chip elektrochemisch aftasten en elektro-osmotisch (EO) pompen. Het integreren van een EO-pomp maakte het opslaan, selecteren en doseren van een aantal verschillende vloeistoffen met de SIP-chip mogelijk. Om een hoge dichtheid en een doelmatige elektronische integratie te bewerkstelligen, moest een EO-pomp worden ontwikkeld met een kleine basisoppervlakte (minder dan 100 µm × 100 µm) en een lage aandrijfspanning (minder dan 10 V).

Het proefschrift begint met een gedetailleerde analyse van het microfabricageproces voor het bouwen van het SIP-netwerk van capillairen, de vrijstaande bladveer en de tip. Voor de fabricage is uitgegaan van gewone microbewerkingen met behulp van beproefde MEMS-processen. De belangrijkste innovatie, eerder ontwikkeld door Hug et al., was het aftekenen van de capillairen van het fluïdisch systeem, de bladveer en de tip in één waver, en het fabriceren van de fluïdische verbindingen door de waver en het aftekenen van de SIP-tip in een andere waver. Door de twee waver op elkaar te bevestigen werden de sleuven afgedekt en door daaropvolgende oxidatie bij hoge temperatuur werden de capillairen gevormd uit hydrofiele siliciumdioxide (SiO_2). Vervolgens werden het ingekapselde fluïdisch systeem en de bladveer vrijgemaakt zodat optisch toegang werd verkregen tot de capillairen. Tenslotte werd vlakbij de bovenkant van de tip het uitlaatgat geboord met behulp van een geconcentreerde ionenbundel. Dit SIP-fabricageproces bood veel mogelijkheden met betrekking tot capillaire geometrie en maakte een complexe capillaire geometrie voor een multifunctioneel microfluïdisch systeem mogelijk. Om eerste ervaringen op te doen met deze kleine capillaire afmetingen, is de integratie onderzocht van een verdampings-micropomp op de SIP. De aandrijving ervan vereiste geen elektroden zodat hij rechtstreeks en zonder enige aanvullende fabricagestappen kon worden geïmplementeerd in het SIP-fabricageproces. Het werkingsprincipe van deze verdampings-micropomp is als volgt: De hydrofiele capillairen van de SIP vulden zich vanzelf met een waterige oplossing. Bij de uitlaat van de capillairen aangekomen, begon de vloeistof te verdampen. Door de capillaire druk bleef de uitlaat van de capillairen vochtig en werd de verdampte vloeistof automatisch aangevuld doordat de capillairen extra vloeistof opzogen. Zo is een éénrichtingspomp gerealiseerd die kon worden geregeld door middel van de temperatuur in het verdampingsgebied. Experimenteel is vastgesteld dat het door verdamping opgewekte debiet varieerde van 7 $pl \cdot s^{-1}$ bij 23° C tot 53 $pl \cdot s^{-1}$ bij 65° C, exponentieel evenredig met de temperatuur.

Een meer geavanceerde bidirectionele EO-pomp met platina (Pt) elektroden

vervaardigd in een vereenvoudigd fabricageproces waarbij SIP-capillairen met vergelijkbare afmetingen ontstonden, is experimenteel geanalyseerd en gemodelleerd. Aangezien er stroom loopt door de Pt-elektroden en de oplossing, was een SIP-specifieke voorziening op de chip nodig om de door elektrolyse gevormde gassen af te voeren. Dit werd gerealiseerd door de elektroden op te nemen in een geavanceerde vloeistof-gasscheider (lg-scheider). De lg-scheider verwijderde de gasbellen uit de vloeistof en voerde ze weg van de EO-pomp. Het werkingsprincipe van de lg-scheider is uitsluitend gebaseerd op diens geometrie met taps toelopende zijwanden en gebruikmaking van de hoge capillaire druk die bij deze kleine afmetingen optreedt op het scheidingsvlak tussen vloeistof en gas van de bellen. De lg-scheider is experimenteel geanalyseerd en gemodelleerd. Bij de experimentele analyse is de maximale tegendruk van de lg-scheider vastgesteld op 0.6 kPa. Hij kon betrouwbaar een vrijkomend gasdebiet van 2 $pl \cdot s^{-1}$ scheiden en afvoeren. Voor een beter begrip is de ontwikkeling en voortplanting van de bel binnen de lg-scheider analytisch beschreven in drie dimensies. Het model en de afgeleide ontwerprichtlijnen laten zien dat Pt-elektroden in combinatie met de lg-scheider een interessant nieuw gebied openen voor complexe hogedichtheid-elektrohydrodynamische en elektrochemisch microfluïdische toepassingen. Ook is er een microfluïdisch systeem geanalyseerd en gemodelleerd dat bestond uit twee lg-scheiders aan weerszijden van een EO-pomp. De EO-pomp bereikte een debiet van 50 pl s^{-1} bij een lage aandrijfspanning van 5 V. Het ontwikkelde corresponderende model van de stromingen binnen het fluïdisch systeem kwam goed overeen met de gemeten waarden. Volgens het model kan een EO-pomp worden gebouwd met een hoge tegendruk (3.6 $kPa \cdot V^{-1}$) waardoor een hoog doseerdebiet van 1.5 $pl \cdot V^{-1} \cdot s^{-1}$ mogelijk is (overeenkomend met een SIP ondergedompeld in water, uitlaatgatstraal van 100 nm). Ook is onderzoek gedaan naar de werking en integratie van een tweede type elektroden op basis van zilver/zilverchloride (Ag/AgCl) in de SIP. Deze elektroden hadden het belangrijke voordeel dat, als de elektrode actief was, de elektrochemische reactie bleef voortduren waarbij Ag werd omgezet in AgCl en omgekeerd in plaats van de vloeistof te elektrolyseren. Bovendien konden deze elektroden worden geïntegreerd in een fabricagestap na productie van de SIP-capillairen waardoor de instabiliteit van de elektrode werd vermeden die wordt veroorzaakt door de oxidatie bij hoge temperatuur voor de vorming van het SiO_2 van de zijwanden van de capillairen. Het algemene productieproces voor het integreren van de Ag/AgCl- elektroden in de geproduceerde SIP-capillairen was:

1. De adhesie van de Ag-elektrode aan het SiO_2 van de capillairwand is verbeterd door toepassing van een polymeer tussenlaag bestaande uit 3-mercaptopropylmethyldimethoxy-silaan (MPS). Het bleek dat deze silaniseringsstap van vitaal belang was voor betrouwbaar stabiele Ag-elektroden bij capillaire afmetingen van minder dan 10 µm, aangezien de elektrode de neiging had te delamineren door de sterke capillaire kracht. Essentieel voor succesvolle silanisering was toepassing van gasfasedepositie op een gedehydrateerd oppervlak om vorming van bolletjes MPS-polymeer te voorkomen.

2. Chemische depositie bleek een zeer flexibel en uniek hulpmiddel te zijn voor depositie van de elektroden in de gesloten SIP-capillairen. Het algemene idee was om de capillairen te vullen met een oplossing van Ag-ionen met een reductiemiddel. Tijdens de elektrochemische reactie begonnen de Ag-elektronen te groeien op de capillairwand. Het was nodig dikke elektroden te vormen aangezien voortdurend ofwel Ag of AgCl werd verbruikt als de elektroden actief waren. Deze depositie van dikke elektroden was in het bijzonder een uitdaging doordat er slechts een zeer beperkt capillair volume beschikbaar was zodat hoge concentraties chemische oplossing werden gebruikt. De beste procesbeheersing van de

chemische depositie werd bereikt met een verbeterde Tollens-oplossing en de reactiesnelheid werd geregeld met geconcentreerd natriumcitraat (vertragen) en geconcentreerd natriumhydroxide (versnellen). Er werden twee verschillende methoden voor chemische depositie gebruikt: Allereerst een discontinu dompelproces met meervoudige chemische deposities en in de tweede plaats een enkelvoudig continu depositieproces waarbij voortdurend verse chemische oplossing werd toegevoerd.

3. Structurering van de elektroden werd gerealiseerd door het regelen van de vulling van de capillairen met de chemische oplossing binnen het fluïdisch systeem met microfluïdische afsluitkleppen. De afsluitkleppen hadden een tweevoudige functie, de oplossing werd betrouwbaar afgesloten tijdens de chemische depositie en naderhand was de afsluitklep gevuld zonder holtes voor een goede fluïdische aansturing van het uiteindelijke apparaat. Dit moet bij voorkeur worden gedaan zonder uitwendige druk toe te passen. Het schakelen tussen stoppen en doorlaten van de oplossing werd geactiveerd door een verandering in de oppervlaktespanning van de oplossing. De werking van de afsluitkleppen werd gemodelleerd door verbetering van het oorspronkelijk tweedimensionale model tot drie dimensies en daarbij rekening te houden met de door het ontwerp bepaalde hoekronding en de kleine capillaire doorsnede.

4. Na chemische depositie en structurering werd de Ag-elektrode vervolgens omgezet in een Ag/AgCl-elektrode. Net als bij de chemische Ag-depositie, werd de elektrodetransformatie uitgevoerd met een stroom van ofwel natriumhypochloride or ferric (III) chloride. De transformatie dient beperkt te blijven tot 20% van de oorspronkelijke Ag-laagdikte vanwege door spanningen veroorzaakte deliminatie of barsten van de elektrode als gevolg van het verschil in dichtheid tussen Ag en AgCl. Interessant genoeg kan het elektrochemische transformatieproces van Ag in AgCl worden beschreven met het Deal-Grove-model voor de oxidatie van silicium. De aangroei van het AgCl was niet-lineair afhankelijk van de elektrochemische reactietijd. Vanaf een AgCl-dikte van ongeveer 40 nm, werd de elektrochemische reactie overheerst door de diffusie van het oxiderende materiaal door een toenemende laag AgCl.

Elektroden werden afgezet in drie verschillende capillairen: a) in het SIP-capillair zelf (doorsnede 2.2 µm × 3.7 µm), b) voor grotere beschikbaarheid en eenvoudiger bereikbaarheid, in commercieel leverbare ronde capillairen (straal tot 520 µm), en c) een polymeer-microfluïdische systeem met rechthoekige capillairen (doorsnede 55 µm × 65 µm). Binnen de SIP is de functionaliteit van de microfluïdische afsluitklep experimenteel geverifieerd, een binaire oplossing van 20% ethanol in water (contacthoek 82°) is afgesloten en een binaire oplossing van 40% ethanol in water (contacthoek 58°) heeft de afsluitklep gevuld zonder holtes. Bovendien is de succesvolle chemische dompeldepositie en structurering van de afsluitklep van Ag-elektroden aangetoond. In ronde capillairen liet meervoudige chemische depositie zien dat bij elke depositie de laagdikte van het Ag met 51 nm toenam. De afgezette Ag-laag had een hoge specifieke geleidbaarheid van 6×10^7 S·m^{-1}, wat wijst op een hoge zuiverheid en dichtheid. De verdere transformatie in Ag/AgCl resulteerde in elektroden voor elektrochemische meting van verschillende pH-waarden. Er werd een lineaire pH-gevoeligheid bereikt van 57.4 mV·pH^{-1} bij 22.7° C met een goede overeenkomst met Nernst-gedrag. Tijdens deze experimenten bleek dat de chemische Ag-depositie zeer gevoelig was voor vervuiling, wat aanzienlijk werd versterkt door de kleine capillaire doorsnede. Daarom werd de depositie in het polymeer-fluïdische systeem uitgevoerd met een continue stroom chemische oplossing in plaats van de eerder gebruikte meervoudige deposities. Vergeleken met de individuele elektrodedepositie, had de continue

depositie het voordeel dat de concentratie in het capillair gedurende de gehele depositietijd constant gehouden kon worden. Hierdoor kon de reactie beter worden gestuurd dankzij een lagere concentratie en daarnaast verminderde dit het effect van het minuscule beschikbare capillaire volume. De EO-pomp binnen het fluïdisch polymeersysteem had een experimenteel bepaald pompdebiet van 0.12 $nl \cdot s^{-1} \cdot V^{-1}$.

Eerst zijn experimenten uitgevoerd met de SIP voor beeldvorming en doseren. Om een eerste praktijkervaring op te doen is een minder gevoelig monster onder minder moeilijke omstandigheden gekozen, en vervolgens is vooruitgelopen op de verwachte SIP-beeldvorming van een levende cel. De mogelijkheden voor beeldvorming zijn geïllustreerd door het maken van beelden onder amplitudemodulatie van een gefixeerde en gedroogde Escherichia Colibacterie. De verkregen beelden hadden een redelijke beeldkwaliteit en resolutie. Bovendien waren er geen speciale vaardigheden vereist voor het bedienen van de SFM aangezien die zich niet anders gedroeg met de geplaatste SIP dan met een geplaatste standaard leverbare SFM. Bij het doseren onder externe druk werd de ontwikkeling van een luchtbel bij het uitlaatgat van de tip waargenomen. Met de momenteel toegepaste methode waarbij de SIP wordt vastgelijmd aan de SFM-houder, werd geen afdoende en betrouwbare bevestiging bereikt. De belangrijkste storingen waren lekkage van de afdichting tussen de SIP en de SFM-houder, vervuiling van de SIP-capillairen, en tenslotte het bezwijken van de SIP-bladveer tijdens de complexe en langdurige plaatsingsprocedure. Dit toont nogmaals de noodzaak aan van het verbeteren van SIP-technieken om te komen tot de autonome on-chip vloeistofbehandeling.

Nomenclature

Symbols

A	Cross sectional area	[m^2]	p_c	Young-Laplace pressure or capillary pressure	[Pa]
Bo	Bond number	[ ]	p_{hy}	Hydraulic pressure	[Pa]
b_p	Bubble parameter	[ ]	p_{int}	Internal pressure	[Pa]
c	Concentration	[$mol \cdot l^{-1}$]	p_V	Partial vapor pressure	[Pa]
D	Diffusion constant	[$m^2 \cdot s^{-1}$]	pH	Negative logarithm of the hydronium concentration	[ ]
d	Depth	[m]	Q	Flowrate	[$m^3 \cdot s^{-1}$]
E	Electric field	[$V \cdot m^{-1}$]	R	Radius	[m]
G	Gibbs free energy	[J]	R_c	Corner radius	[m]
g	Gravity	[$m \cdot s^{-2}$]	Re	Reynolds number	[ ]
H_{vap}	Evaporation enthalphy	[$N \cdot m \cdot mol^{-1}$]	R_{el}	Electrical resistance	[Ω]
h	Height	[m]	R_{hy}	Hydraulic resistance	[$Pa \cdot s \cdot m^{-3}$]
I_{el}	Electrical current	[A]	T	Temperature	[K] [°C]
I_z	Second moment of inertia	[m^4]	t	Time	[s]
k	Stiffness	[$N \cdot m^{-1}$]	U	Voltage drop	[V]
l	Length	[m]	U	Internal energy	[J]
l_c	Characteristic cross sectional length	[m]	V	Volume	[m^3]
M	Molarity	[$kg \cdot mol^{-1}$]	v	Velocity	[$m \cdot s^{-1}$]
N_E	Evaporation rate	[$mol \cdot m^{-2} \cdot s^{-1}$]	w	Width	[m]
p	Pressure	[Pa]	Y	Young's stiffness modulus	[Pa]
p_b	Backpressure LG-separator	[Pa]	Z	Valence of charged ion	[ ]

Constants

e	Elementary charge	1.6×10^{-19} C	k_B	Boltzmann constant	1.38×10^{-23} $J \cdot K^{-1}$
ε_0	Electrical permittivity in vacuum	8.85×10^{-12} $A \cdot s \cdot V^{-1} \cdot m^{-1}$	R	Avogadro constant	6.02×10^{23} mol^{-1}

Greek Symbols

β	Taper angle	[deg]	μ_{eo}	Electroosmotic mobility	$[m^2 \cdot V^{-1} \cdot s^{-1}]$
γ	Surface tension	$[N \cdot m^{-1}]$	μ_{ep}	Electrophoretic mobility	$[m^2 \cdot V^{-1} \cdot s^{-1}]$
ε	Hydraulic resistance depending on electrode misalignment within the LG-separator	$[Pa \cdot s \cdot m^{-3}]$	υ	Evaporation induced flow	$[m^3 \cdot s^{-1}]$
ζ	Zeta potential	[V]	ρ_{el}	Specific electrical resistance	$[\Omega \cdot m]$
η	Dynamic viscosity	[Pa·s]	ρ_l	Liquid density	$[kg \cdot m^{-3}]$
θ	Contact angle	[deg]	σ_{ch}	Surface charge	$[C \cdot m^{-2}]$
κ	Opening angle at a rounded corner	[deg]	σ_s	Specific conductivity	[S·m]
λ_D	Debye layer thickness	[m]			

Abbreviations and Acronyms

CCD	Charged Coupled Device	NADIS	Nanoscale Dispensing
CMOS	Complementary Metal Oxide Semiconductor	NFP	Nano Fountain Probe
DPN	Dip Pen Nanolithography	NOA63	UV Curable Polymer
DRIE	Deep Reactive Ion Etching	PECVD	Plasma Enhanced Chemical Vapor Deposition
EDX	Energy Dispersive X-ray Spectroscopy	RIE	Reactive Ion Etching
EO	Electroosmotic	SEM	Scanning Electron Microscope
FIB	Focussed Ion Beam	SFM	Scanning Force Microscope
FPN	Fountain Pen Nanochemistry	SIP	Scanning Ion Pipette
LG	Liquid-gas	SU8	Negative Photoresist
LPCVD	Low Pressure Chemical Vapor Deposition	la	liquid-air
MEMS	Micro Electro Mechanical System	sa	solid-air
MPS	Polymeric-mercapto-silane	sl	solid-liquid

Chemicals and chemical compounds

Ag	Silver	NaH_2PO_2	Sodium hypophosphite
AgCl	Silver chloride	NaOH	Sodium hydroxide
$AgNO_3$	Silver nitrate	NH_4OH	Ammonium hydroxide
AgO_2	Silver oxide	PDMS	Polydimethylsiloxane
Au	Gold	Pt	Platinum
BHF	Buffered hydrofluoric acid	PtSi, Pt_2Si	Platinum silicide
DNA	Deoxyribonucleic acid	Si	Silicon
Ga	Gallium	Si_3N_4	Silicon nitride
H_2O	Water	SiO_2	Silicon dioxide
OH^-	Hydroxide ion	SiO^-	Silanoate
H_3O^+	Hydronium ion	SiOH	Silanol group
H_2O_2	Hydrogen peroxide	Ta	Tantalum
H_3PO_4	Phosporic acid	Ti	Titanium
HEPES	4(2-hydroxylethyl)-1-piperazine-ethansulfonic acid	TMAH	Tetramethylammonium hydroxide
KCl	Potassium chloride	O_2	Oxygen
KOH	Potassium hydroxide	Zr	Zirconium
MPS	3-mercaptopropyldimethoxy-methyl silane		

Curriculum Vitae

Friedjof Heuck was born 30.11.1980 in Seeheim-Jugenheim, DE

Education

Ph.D.	**Microsystems Engineering combined with Microfluidics**
10/2010	Developing and Analyzing sub-10 µm Fluidic Systems with Integrated Electrodes for Pumping and Sensing in Nanotechnology Applications, Thesis supervised by Prof. Dr. U. Staufer
01/2008-10/2010	Micro and Nano Engineering Laboratory, Delft University of Technology, Delft, NL, headed by Prof. Dr. U. Staufer
09/2006-02/2007	The Sensors, Actuators and Microsystems Laboratory, Université de Neuchâtel, Neuchâtel, CH, headed by Prof. Dr. N.F. de Rooij
Diplom equiv. Master	**Microsystems Engineering**
04/2006	Nonlinear Effects in Integrated Hall Plates, Thesis supervised by Prof. Dr. O. Paul
10/2001-04/2006	Study of Microsystems Engineering with emphasis Processes and Materials, IMTEK, Albert-Ludwigs-University, Freiburg, DE
Highschool	
09/1990-06/2000	Christoph-Probst Gymnasium, specialization in science, Gilching, DE
Employments	**Scientific staff member at different chairs**
01/2008-10/2010	Micro and Nano Engineering Laboratory, PME, Delft University of Technology, Delft, NL, headed by Prof. Dr. Staufer
09/2006-12/2007	The Sensors, Actuators and Microsystems Laboratory, IMT, Université de Neuchâtel, Neuchâtel, CH, headed by Prof. Dr. de Rooij
05/2004-04/2006	Microsystem Materials, IMTEK, University of Freiburg, headed by Prof. Dr. Paul
01/2003-03/2004	Chemistry and Physics of Interfaces, IMTEK, University of Freiburg, headed by Prof. Dr. Rühe

Publications

Peer Review	**Journal Articles**
09/2010	F. Heuck and U. Staufer, Electroless Deposition and Structuring of Silver Electrodes in Closed Microfluidic Capillaries, submitted to *Journal of Microelectromechanical Systems*
09/2010	F. Heuck, P. van der Ploeg and U. Staufer, Deposition and Structuring of Ag/AgCl Electrodes Inside a Closed Polymeric Microfluidic System for Electroosmotic Pumping, submitted to *Microelectronic Engineering*
08/2010	F. Heuck and U. Staufer, Low Voltage Electroosmotic Pump for High Density Integration into Microfabricated Fluidic Systems, submitted to *Microfluidics and Nanofluidics*
12/2009	F. Heuck and U. Staufer, Silver/Silver-chloride electrode fabrication in closed micro-fluidic capillaries, *Microelectronic Engineering,* 1383-1385
01/2008	F. Heuck, T. Hug. T. Akiyama, P. L. T. M. Frederix, A. Engel, A. Meister, H. Heinzelmann, N. F. de Rooij and U. Staufer, Evaporation based micropump integrated into a scanning force microscope probe, *Microelectronic Engineering*, 1302-1305
Conferences	**National and international conferences**
09/2010	P. van der Ploeg, F. Heuck and U. Staufer, MNE Conference, Genoa (IT)
09/2010	F. Heuck and U. Staufer, Het Instrument, Amsterdam (NL)
09/2009	F. Heuck and U. Staufer, MNE Conference, Gent (BE)
06/2009	F. Heuck P. M. Sarro, J. Slabbekoorn, T. Akiyama, N. F. de Rooij and U. Staufer, Proceedings of the EUSPEN conference, 158-161, San Sebastian (ES)
12/2008	F. Heuck and U. Staufer, Dutch Scanning Probe Symposium, Utrecht (NL)
03/2008	F. Heuck, T. Hug. T. Akiyama, P. L. T. M. Frederix, A. Engel, A. Meister, H. Heinzelmann, N. F. de Rooij and U. Staufer, SPS annual meeting, Geneva (CH)
09/2007	F. Heuck, T. Hug. T. Akiyama, P. L. T. M. Frederix, A. Engel, A. Meister, H. Heinzelmann, N. F. de Rooij and U. Staufer, MNE Conference, Copenhagen (DK)

05/2007	F. Heuck, T. Akiyama, N.F. de Rooij and U. Staufer, MicroNano-Fabrication Annual Review Meeting, Lausanne (CH)
01/2006	A. Trautmann, R. Denfeld, F. Heuck, P. Ruther and O. Paul, Proceedings MEMS'06, 434-437, Istanbul (TR)
10/2005	A. Trautmann, F. Heuck, C. Mueller, P. Ruther and O. Paul, Mikrosystemtechnik Kongress, Freiburg (DE)
06/2005	A. Trautmann, F. Heuck, C. Mueller, P. Ruther and O. Paul, Proceedings Transducers'05, 1420-1423, Seoul (KR)

Scientific Grant

07/2010	U. Staufer, F. Heuck and M.H.J van Acht, Micro Dispensing a Raft of Oligonucleotides, Proteins or other Liquid Extracts to Targeted Sites, FES Proposal HTS&M financed by the Dutch government

Achievements	**Related to this thesis**
09/2010	Best Poster Award, MNE Conference, Genoa, IT
09/2010	*Market meets Science* Award, 2nd place, Het Instrument, Amsterdam, NL
09/2007	Best Nano Image Award, NCCR Nano, Basel, CH

Teaching	**Developing and updating studentcourses**
01-12/2009	*Physics for mechanical engineers*, Master, exercise, English
02/2009	*Electron beam lithography*, Master, lecture, English
11-12/2008 & 11-12/2009	*Surface roughness measurement*, Master, laboratory, English
03 & 07/2007	*Microfabrication of a scanning force microscope chip*, Bachelor, Cleanroom, German/English
09/2007	*Semiconductor devices*, Master, exercise, French

Acknowledgments

What is better than finishing the thesis, even though I guess that this is the first page you read, with saying thank you to all the people who contributed to this work. First, I would like to express my deepest appreciation for the guidance, supervision and education I received from my supervisor: Thank you Urs! The freedom and the discussion at the right time allowed me to further develop, broaden and sharpen my own approach to solve scientific challenges. During those four years you successfully helped me going through all the different phases of solving scientific problems, i.e. naive & curious tackling, desperately biting & massaging, then the satisfaction of finding a partial solution, the secure feeling of trusting this solution and finally finding & exploring new applications based on this solution. This makes, for me, the distinct difference between a Ph.D. thesis and an engineering work in the industry. In addition, I highly appreciated the opportunity to experience and to take part in establishing your new section, here in Delft.

Nevertheless, Neuchatel was a perfect start for my PhD and there, I especially have to thank Nico for establishing this excellent research environment. Teru for the showing me insides of a successful, patient and highly professional microfabrication. Je souhaiterais également remercier Edith, la fée bienfaitrice de la salle blanche dans une foret de difficultés. Thank you for the time in Neuchatel: Peter, Sebastian, Dara, Roland, Michi, Patrick, Yannik, Severin, Laure, Don, Daniel, Kaspar, Silvia, Laurent, Christian and all the others not mentioned here. Still in Switzerland, but this time in Basel, I would like to thank Patrick for introducing me into scanning force microscopy.

Coming now here to my time in Delft, I would like to thank my dear colleagues for their support, input, discussion and useful time to parchate, especially to Pablo, Sander (former CSO), Marcello, Eric, Jon, Sophie, Iwan, Ali, Marli, the coffee table with Rudolf (CSO), Jasper, Jeroen, Guido, Maarten and all the other colleagues from MNE, MSD and PME. Also to the support of my master students, Erik, Paul and Kees. To the strong men from the PME support staff, Rob, Harry, Patrick and Jos. Special thanks go to Dimes: Lina, John, Charles, Luigi, Jan Cornelis and Gregory. It was not always easy but at the end we fabricated nice working devices, thank you! Thank you also to Hozanna and Paul for the focussed ion beam cuts. Last but not least, thank you to Uli and Ralph for sponsoring the spin coater and the hotplate and Phi for commenting and correcting my thesis and any other paper I had to write. Furthermore, I would like to thank the members of my examination committee for investing their time and energy to read and comment my thesis.

Finally, I would like to thank my parents for their support and encouragement to achieve this ultimate step, concluding a 23- years of school & university education. It is a highly reassuring feeling to have this strong family network behind me. Also, I am impressed with how much persistence and understanding you proof read my thesis, even though the content was far beyond your field of expertise. The same accounts for my love, Aurelie, who especially brought me back to what can be considered a normal life in the final phase of my thesis.

One of the most important contributors of ideas and support, as well as, creators of a very stimulating atmosphere at home, the best flatemates, thank you Ivan and Pablo.

Last but not least, thank you to the network of friends who contributed to this work by making this time a highly various mixture of international flavors, among others, Andres, Andreia, Bea, Carla, David, Donata, Ilhan, Julie, Kate, Layla, Marcos, Maria, Martha, Nazli, Patrice, Sinar, Steffi,....

Yours,

Friedi Delft 01.09.2010

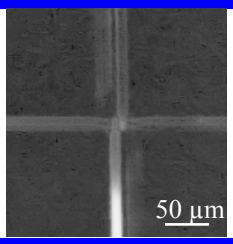

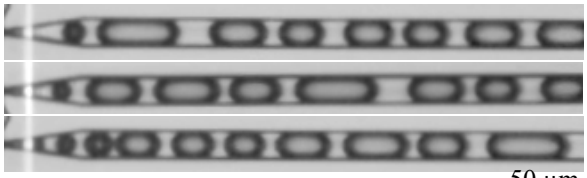

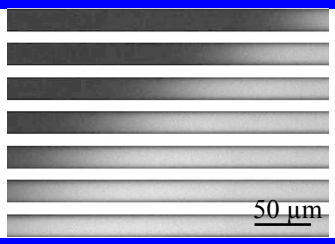
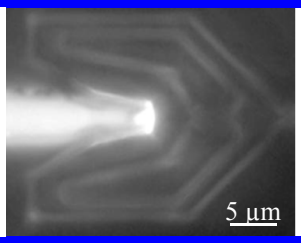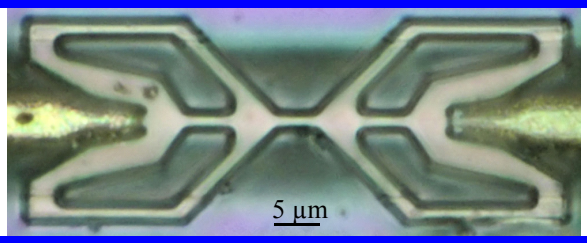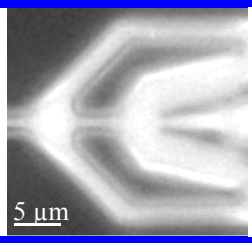
In this thesis, sub-10 µm fluidic systems, with integrated electrodes for pumping and sensing, in nanotechnology applications were developed and analysed. This work contributes to the development of the scanning ion pipette (SIP), a tool to investigate on the nanometer scale surface changes induced by locally administering chemically or bioactive solutions. For this purpose, the already existing technology of a micropipette integrated into a scanning force microscope chip was enhanced by the use of electrodes for on-chip electrochemical sensing and electroosmotic pumping. The integration of an eo pump offered the possibility of storing, selecting and dispensing multiple different liquids within the SIP chip. For a high density and convenient electronic integration, an eo pump with a small footprint (less than 100 µm × 100 µm) and low actuation voltage (less than 10 V) had to be developed.